Veronika Obersteiner, BSc

Impact of collective effects on charge transport through molecular monolayers

Master Thesis

For obtaining the academic degree

Diplom-Ingenieur

Master Programme of Technical Physics

Graz University of Technology

Supervisor:

Ao.Univ.-Prof. Dipl.-Ing. Dr.techn. Egbert Zojer

Institute of Solid State Physics

Graz, March 2014

Acknowledgements

Zu allererst möchte ich mich herzlichst bei meinem Betreuer, Prof. Egbert Zojer, bedanken, der mich im letzten Jahr mit großem Engagement unterstützt und begleitet hat. Eingebettet in ein unvergleichliches Arbeitsumfeld konnte ich nicht nur außerordentliche wissenschaftliche Erfahrungen sammeln, sondern auch ganz besondere Menschen kennenlernen, welche mich in dieser Zeit auf unterschiedlichste Art unterstützt und motiviert haben.

Ich möchte mich herzlichst bei der gesamten Arbeitsgruppe bestehend aus Iris Hehn, Gernot Kraberger, Bernhardt Kretz, Elisabeth Verwüster und Elisabeth Wruß für die Unterstützung und die gemeinsame Zeit innerhalb und außerhalb der Universität bedanken. Ein spezielles Dankeschön möchte ich an David Egger richten, der mich sowohl hinsichtlich der Einarbeitung als auch beim Voranschreiten meiner Arbeit mit seinen wertvollen Erfahrungswerten unterstützt hat. Zudem danke ich Georg Heimel von der Humboldt Universität zu Berlin für die gute Zusammenarbeit.

An dieser Stelle möchte ich mich auch noch bei der Abteilung für Scientific Computing des Zentralen Informatikdiensts (ZID) der TU Graz für die zur Verfügung gestellten Ressourcen und beim Österreichischen Wissenschaftsfonds (FWF): I937-N19 für die Förderung meiner wissenschaftlichen Arbeit bedanken.

Innerhalb des Studiums gab es unzählige Menschen, die meine Zeit an der Universität unvergesslich machten. Ich möchte mich speziell bei meinem Kollegen Werner Dobrautz bedanken, der mich nicht nur in Zeiten unseres gemeinsamen Prüfungsmarathons begleitet hat, sondern mir auch während der Diplomarbeit verständnisvoll zur Seite stand.

Meinem Physikprofessor Kurt Pirscher möchte ich dafür danken, dass es ihm auf seine kreative Art und Weise gelang, in mir schon als Schülerin die Begeisterung und Leidenschaft für die Physik zu wecken.

Ein ganz besonderes Dankeschön möchte ich meiner Familie widmen, die mich stets darin bestärkt hat Herausforderungen entschlossen anzunehmen. Meinen Eltern, Uta und Hans danke ich für den stabilen Rückhalt und die große Unterstützung, die Sie mir besonders in der Zeit des Studiums entgegengebracht haben. Zudem möcht ich meiner Oma danken, die mir immer wieder die Möglichkeit bietet, meinem Gedankenreich zu entfliehen und meine freien Stunden in der Natur zu genießen.

Nicht zuletzt möchte ich mich bei Daniel für die liebevolle Unterstützung, den Rückhalt und den Zuspruch in den letzten sieben Jahren bedanken. Für unzählige schöne Momente, für seine unvergleichlich lustige und liebevolle Art und große Rücksichtnahme in herausfordernden Zeiten meines Physikstudiums.

Abstract

Impact of collective effects on charge transport through molecular monolayers

Veronika Obersteiner
Institute of Solid State Physics, Graz University of Technology, 8010 Graz, Austria

In the area of molecular electronics, it has been increasingly acknowledged over the past years that there are fundamental differences between charge transport through individual molecules and through continuous, extended, two-dimensional monolayers.

In the present work these differences are related to effects that originate from the collective electrostatic interactions between molecules in an extended system. This is theoretically demonstrated by varying the coverage in self-assembled monolayers (SAMs) consisting of organic molecules with dipoles distributed along their backbones. Starting with SAMs at full coverage the molecular density is continuously reduced until arriving at the single-molecule level.

The coverage dependent calculations are performed using density functional theory (DFT). To determine the transport properties, the transmission coefficients are calculated applying a Green's function approach.

Besides varying the coverage, collective effects are additionally studied for molecular clusters of varying size. When measuring transport through molecular junctions, it is often the case, that one deals with a bunch of molecules, rather than having only one single molecule comprised between the leads. Therefore, especially for experiments, it is important to know at which number of molecules such collective electrostatic effects start to appear.

To study the impact of the docking chemistry (that is known to also strongly affect electrical transport), collective effects are investigated for different anchoring groups forming the contact between the SAMs and the gold electrodes.

Kurzfassung

Einfluss von kollektiven Effekten auf den Ladungstransport in molekularen Monolagen

Veronika Obersteiner
Institut für Festkörperphysik, Technische Universität Graz,
8010 Graz, Austria

Im Bereich der molekularen Elektronik stellte es in den letzten Jahren zunehmend heraus, dass es fundamentale Unterschiede im Ladungstransport durch einzelne Moleküle und durch kontinuierliche, ausgedehnte, zweidimensionale Monolagen gibt.

In der vorliegenden Arbeit werden diese Unterschiede auf Effekte zurückgeführt, die eine Folge von kollektiven, elekrostatischen Wechselwirkungen zwischen den Molekülen sind. Dies wird theoretisch durch Variation der Bedeckung in selbstassemblierten Monolagen (SAMs), welche aus Molekülen mit eingbauten Dipolen bestehen, beschrieben. Ausgehend von voller Bedeckung, wird die Dichte der Moleküle nach und nach verringert bis man die Situation des Einzelmoleküls erreicht.

Die bedeckungsabhängigen Berechnungen werden mit Hilfe der Dichtefunktionaltheorie (DFT) durchgeführt. Um die Transporteigenschaften zu bestimmen, werden die Transmissionskoeffizienten unter Anwendungen der Green's Funktionen berechnet.

Neben der Veränderung der Bedeckung, werden kollektive Effekte zusätzlich für molekulare Cluster verschiedener Größen untersucht. Experimentell hat man es häufiger mit einer Ansammlung von Molekülen zu tun als mit einem einzelnen Molekül. Deshalb ist es speziell für Experimente interessant, ab welcher Anzahl von Molekülen kollektive elektrostatische Effekte auftreten.

Um den Einfluss von Ankergruppen zu untersuchen, die sich bekanntlich sehr stark auf das Transportverhalten auswirken, wurden kollektive Effekte zusätzlich für verschiedene funktionelle Gruppen untersucht, die den Kontakt zwischen des SAMs und den Goldelektroden bilden.

Contents

1 Introduction and Motivation

In this chapter an introduction into the field of molecular electronics, as well as the main motivation for this thesis shall be presented. It will start with the basic ideas of molecular electronics combined with the most important facts related to its history. A detailed dicussion of recent results concerning the difference between single-molecule and full monolayer junctions follows, leading to the basic ideas that motivated this work. Finally, the importance of docking groups in molecular junctions will be discussed with a subsequent short summary of the most important experimental techniques within molecular electronics.

1.1 Molecular Electronics

Molecular electronics is an interdisciplinary field of science, involving the combined knowledge from traditional disciplines like physics, chemistry, biology and engineering to investigate electrical and thermal properties in nanoscale devices, in which individual molecules or an assembly of them act as basic building blocks. Since some of the feature dimensions of such molecular circuits are of the order of nanometres, molecular electronics can also be seen as a subfield of nanoscience.

Many review articles were published on this topic in the last years. These include [1], [2] and more recently [3] and [4]. Additionally, there is a very recommendable book called *Molecular Electronics - An Introduction to Theory and Experiment* by Cuevas and Scheer [5], where amongst others, detailed information about the history of molecular electronics and its experimental techniques can be found. This chapter builds on [2] and [5].

Molecular electronics is based on the **bottom-up approach**, where elementary pieces, like atoms are assembled to build more complex structures, as opposed to the top-down approach, where macroscopic systems are shrinked by cutting, etching and lithography process, but soon arrive at its intrinsic limits. Since single molecules are the basic electronic components in these devices, a unique ingredient of variability and structural control can be added, that cannot be achieved by conventional solid state physics. Choosing different compositions and geometries of the molecules offers the ability to extensively vary transport, optical or structural properties. With device densities orders of magnitudes higher than todays state of the art, molecular electronics could have the potential means of extending Moore's Law to dimensions of a single molecule.

With benefits in size, speed and functionality, the vision of molecular electronics was once to replace the silicon-based technology. Up to now this seems to be relative unlikely, but nevertheless molecular electronics has become a huge and important playground in fundamental science, having more the character of supporting todays technology rather than replacing it.

One of the most important works concerning the **history of molecular electronics** was done in 1974, when Arieh Aviram and Mark Ratner suggested to use a single molecule as a molecular rectifier [6]. This was a theoretical work describing how a modified charge-

transfer salt could operate as a traditional diode in an electrical circuit. At this time this idea was more a theoretical curiosity and could not be tested experimentally, mainly, because of the disability of attaching the electrodes to the molecule.

As for many fields in nanoscience, the invention of the Scanning Tunneling Microscope (STM) by Gerd Binnig and Heinrich Rohrer in 1981 [7], changed the view for this field. For the first time it was possible to really manipulate matter on the atomic scale [8]. Besides, at the end of the 1980's the mechanically controllable break junction (MCBJ), introduced by Moreland et al. [9] and Muller et al. [10], was used to fabricate metallic wires of atomic dimensions.

This was a great improvement for molecular electronics and in 1997 the collaboration of James Tour and Mark Reed led to a publication [11], that is known to be the first transport experiment in single-molecule junctions and is considered the real birth of molecular electronics. They used the MCBJ technique to contact benzenedithiol with gold electrodes. From that time on, many new experimental techniques (see section 1.4) were invented and also on the theoretical side there was much progress.

The central question in molecular electronics is to understand how electrons move through a single molecule. The attempt to characterize charge transport through single molecules or an assembly of them bridging external contacts experimentally as well as theoretically, led to the discovery of many characteristic functions, such as diodes [12], switches [13], transistors [14] and memories [15].

1.2 Single Molecule vs. Monolayer

Typical investigated systems in molecular electronics are so called molecular junctions, as shown in Fig. 1. They consist of a left and a right electrode and in between the organic part composed of a molecular backbone and the docking group. The latter is the group of atoms that attach the molecule to the electrode. To obtain the transport characteristics, a voltage is applied and the current is measured.

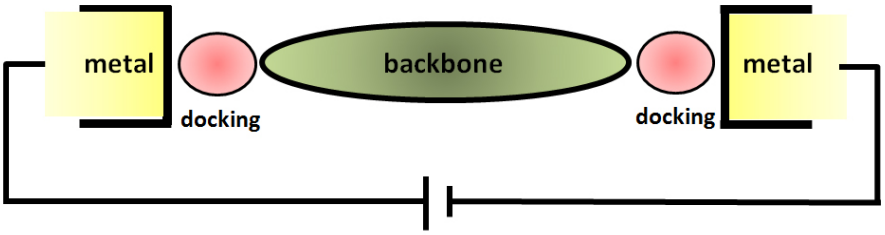

Figure 1: Molecular junction consisting of a left and a right electrode and the organic part in between

Electronic transport properties in these metal-molecule-metal systems generally depend on the electronic properties of the metal electrodes and the molecular constituent, on the bonding between them (mainly the docking group [16]), on the junction geometry and

conformation [17], [18] and on environmental parameters such as temperature [19].

Additionally, it has been shown that putting a single molecule into the junction results in hugely different properties compared to putting an assembly of molecules, also called a self assembled monolayer (SAM) (see Fig. 2). Therefore, the dependence on the number of molecules in the conduction process is also an important issue that has been addressed in several experimental [20], [21], and theoretical works [22], [23], [24]. Latest results concerning this issue will be discussed in the following.

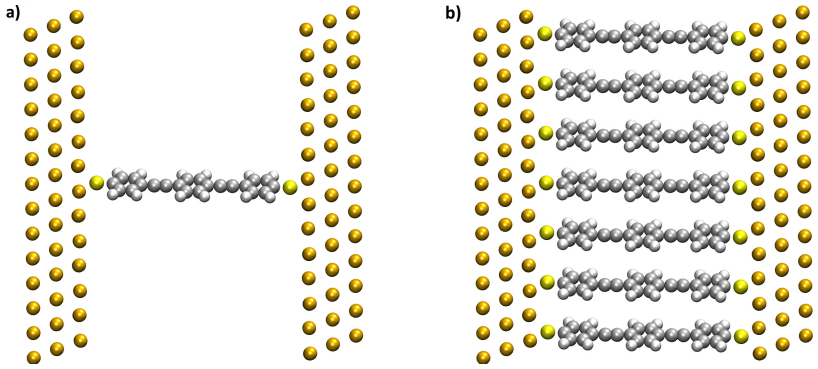

Figure 2: (a) Single molecule junction and (b) molecular junction comprising the corresponding SAM

When dealing with ensemble characteristics of molecules that form SAMs of different densities, the responsible effects are termed as **cooperative** or **collective effects** [22], [25], [26], [23], [20]. While electron transport through single molecules is reasonable well understood [27], the scaling with molecular coverage is still a disputed topic, yielding oppositional predictions when going from single to multiple molecules in parallel. On the one hand, a common practice is to associate the conduction-per molecule measured from monolayer junctions with that of the single molecule junction. This linear scaling was indicated by Cui et al. [28] and Xu and Tao [29], but also by Kushmerick et al [30]. On the other hand, conduction of single molecule junctions was found to be orders of magnitudes larger than the corresponding monolayer conduction-per-molecule [31].

Also, theoretical studies led to contradicting results. N Molecular wires were found to obey a kind of pseudo Ohm's law [32]

$$G_N = NG_1^{eff}, \tag{1.1}$$

where G_1^{eff} is an effective single wire conductance, differing from the corresponding single molecule property because of intermolecular interactions. In many cases cooperative effects cause $G_1^{eff} > G_1$ [23], [33], but there are also reports about $G_1^{eff} < G_1$ [23], [33].

While direct intermolecular coupling and substrate-mediated coupling were found to explain cooperative phenomena [20], **collective electrostatic effects** are particularly important for adsorbed polar monolayers, as emphasized in [34], [35], [36]. In their experimental work [21] Selzer et al. investigated molecular junctions consisting of isolated

individual monolayers on the one hand and self assembled monolayers on the other. They found that the conduction per molecule assembled in the SAM is similar to that of the corresponding individual molecule, but the differential conductance of the individual molecule increases more rapidly with bias and can become a thousand time larger than that of the SAM. They related these differences to electrostatic effects depending crucially on the local molecular environment, i.e. on the existence of neighbouring molecules.

In general, a polar monolayer introduces an electrical dipole perpendicular to the surface/interface, resulting in a shift in the electrostatic potential energy. The magnitude of the potential-energy step ΔE due to the induced dipole layer with the dipole moment μ per surface area A can be described by the Helmholtz equation,

$$\Delta E = \frac{\mu}{\epsilon_0 A} = \frac{qd}{\epsilon_0 A} \tag{1.2}$$

where ϵ_0 denotes the vacuum permettivity and μ can be expressed by the charge q times the seperation distance d. This simple picture effectively treats the monolayer as a dielectric parallel plate capacitor [37], but since a layer of molecules is a quantum mechanical object with rapid variations in charge density along lateral and vertical directions, this picture has to be adapted. Natan et al. [34], therefore, emphasized the fundamental electrostatic difference between one dipole and an array of dipoles and found that the characteristic decay-length of the electric field for a two-dimensional array of dipoles is $d/(2\pi)$, with d being the lateral distance of the dipoles. Therefore the induced electric field decays much faster for an array of dipoles than for a single dipole.

A very important theoretical work concerning the difference between single molecules and monolayers in molecular junctions and at the same time the main motivation for this thesis was presented by David A. Egger et al. in 'Polarity Switching of Charge Transport and Thermoelectricity in Self-Assembled Monolayer Devices' [38].

In their work they investigated the charge-transport characteristics of two isomeric molecules, shown in Fig. 3a. Based on the 'Tour-wire' molecule [39], a very famous model system in molecular electronic named after James Tour, chemical modifications were built into the molecular backbone by symmetrically replacing the two outermost phenyl rings with pyrimidine rings. Referring to the position of the nitrogen atoms on the inner and outer part of the rings, they are called N_{in} and N_{out} molecule, respectively. Since these two isomeric molecules are fully symmetric, they have no net dipole moment, but by introducing the pyrimidine units, their polar bonds and those on the thiol docking groups add up to a local dipole moment on the peripheries of the N_{in} molecule, while they essentially cancel for the N_{out} molecule.

As isolated single molecules N_{in} and N_{out} were shown to have very similar HOMO (highest occupied molecular orbital) and LUMO (lowest unoccupied molecular orbital) energies, leading to nearly the same molecular IP (ionization potential). The molecular IP can to first order be approximated by the energy difference between the HOMO and the vacuum energy E_{vac}, as can be seen in Fig. 4, showing the energetic situation for the non-

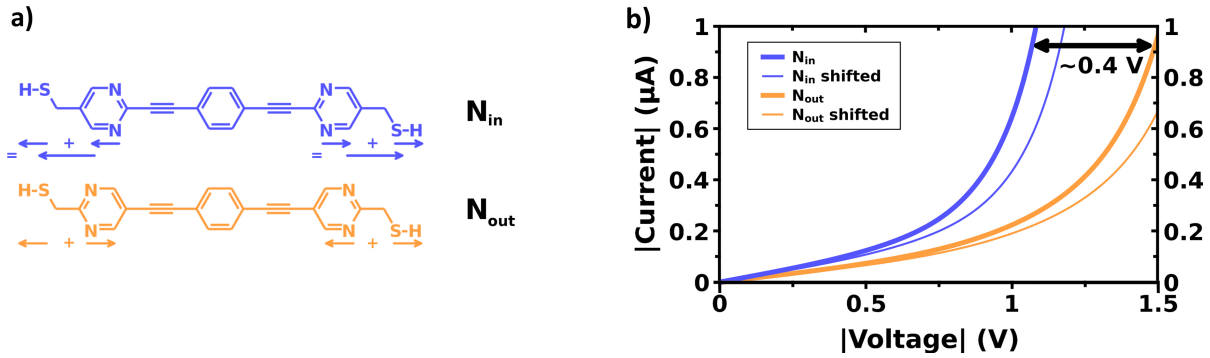

Figure 3: (a) Chemical structures of N_{in} and N_{out} molecules with arrows indicating the local dipoles. (b) Calculated current-voltage characteristics of the SAM devices. Reproduced with permission from ref. [38], ©2012 WILEY-VCH Verlag GmbH&Co.KGaA, Weinheim

interacting metal-molecule system. The alignment of the molecular orbitals, in this case the HOMO with the Fermi energy E_F, determines the so called charge injection barrier ΔE_{HOMO}, which charge carriers have to overcome to enable current flow. Therefore, the alignment of the molecular orbitals with the Fermi level of the external electrodes is a dominant parameter controlling transport through molecular junctions [40]. Since N_{in} and N_{out} have a very similar molecular IP, one might expect similar transport characteristics for the respective devices.

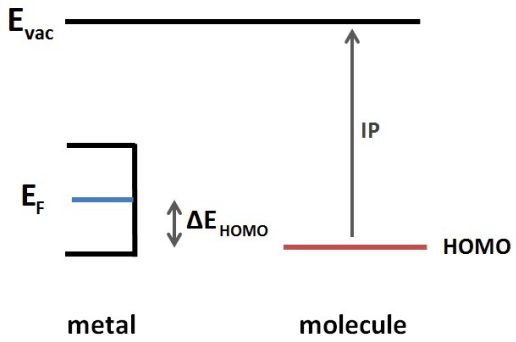

Figure 4: Energetic situation for the non-interacting metal-molecule system emphasizing the impact of the molecular IP on the charge injection barrier ΔE_{HOMO}

But, arranging these molecules into self assembled monolayers (SAMs) and calculating charge-transport characteristics of the associated molecular devices on the basis of DFT and Green's function techniques resulted in entirely different current-voltage curves for N_{in} and N_{out}, as can be seen in Fig. 3b.

Although N_{in} and N_{out} are very similar as isolated species, for the N_{in} SAM a current up to a factor of 9 higher than for the N_{out} SAM was obtained in the low-bias regime. Additionally a fundamentally different nature of charge transport through the SAMs was found. The nature of charge transport through molecular junctions is characterized by

their dominant transport orbitals and, therefore, dependent on the position of the Fermi energy of the metallic contacts with respect to the HOMO and LUMO levels of the organic part. While molecules with E_F lying closer to the HOMO level exhibit p-type current with holes being the dominant charge transport carriers, molecules that are predicted to conduct through the LUMO exhibit n-type current, mainly carried by electrons. The polarity switch from primarily p-type conduction for the N_{in} device to n-type conduction for N_{out} can be seen in Fig. 5a. It implies a change in the thermoelectric properties, namely a change in sign of the appropriate Seebeck coefficient associated with the junction. Details on thermoelectric properties, charge transport polarity and Seebeck coefficients will be given in section 4.2.

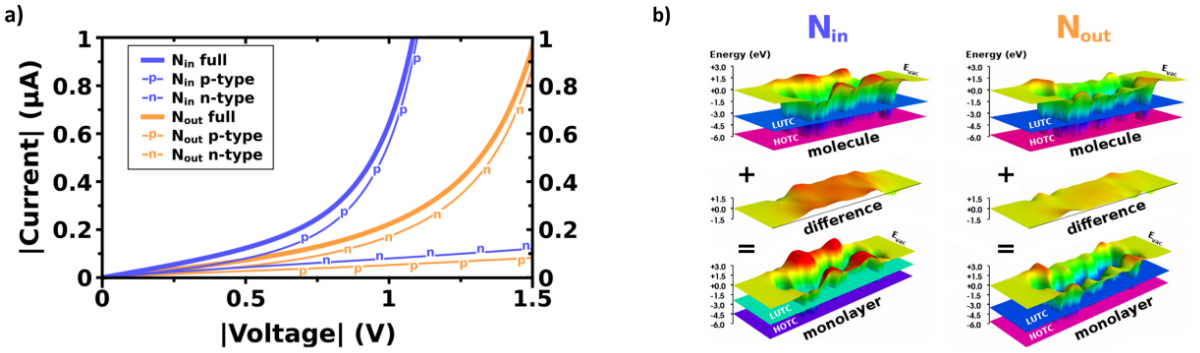

Figure 5: (a)Calculated charge-transport characteristics of N_{in} and N_{out} SAM-devices. (b) DFT calculated potential wells of N_{in} and N_{out} isolated molecules (top) and free standing monolayers (bottom), and the respective potential energy difference, emerged from collective electrostatic effects (middle). Reproduced with permission from ref. [38], ©2012 WILEY-VCH Verlag GmbH&Co.KGaA, Weinheim

The explanation for this observation are purely electrostatic effects connected to the superposition of fields generated by the polar bonds present in N_{in} and N_{out} molecules. When assembling these two isomeric molecules in respective monolayers, the fields from local dipoles on the peripheries of the N_{in} molecule add up, while there are no local dipoles for the N_{out} molecule. The impact of this collective effect on the potential energy landscape is illustrated in Fig. 5b and is very different for N_{in} and N_{out} molecules arranged in SAMs. When arranging the local dipoles of the N_{in} molecule, the potential energy in the region of the backbone is shifted by about 1 eV towards the vacuum level. Since the differences between isolated molecule and monolayer only arise from the ensemble of molecules that form the SAMs, the responsible effect was termed to be a **collective electrostatic effect**. This collective effect together with the interface dipole were found to be responsible for the entirely different transport characteristics for N_{in} and N_{out} SAMs.

The main goal of this thesis is to demonstrate these typically thereby underestimated implication of collective electrostatic effects, by studying their coverage dependence and their implications on charge-transport properties on the basis of DFT calculations combined with Green's function techniques. By varying the coverage in molecular junctions comprising these molecules with dipoles distributed along their backbones, different pack-

ing densities of the respective SAMs can be achieved, leading to intermediate situations between single molecule and SAM, with not as densely packed molecular arrangements as was assumed in [38]. It will be shown that a simple extrapolation of the single-molecule picture to the respective SAM is insufficient to describe electrical properties in the associated monolayer device. In addition to N_{in} and N_{out}, molecules with different docking groups will be investigated.

1.3 Docking Groups

The behaviour of charge transport through molecular junctions consisting of a single molecule or an assembly of them coupled to metal electrodes is very sensitive to the detailed atomic structure of the contact region between the metal and the molecule. The strength of the metal-molecule coupling can be tuned chemically by using appropriate docking groups. Therefore, the influence of the docking chemistry is of great interest in molecular electronics and was widely investigated experimentally [41], [42], [43], [44], [45] as well as theoretically [46], [47], [48], [49].

Depending on the electrode material, proper anchoring groups need to be found, that provide both stability and high contact transparency to electrons. To date, the combination of thiol (SH) moieties and gold electrodes is by far the most studied metal-molecule system, primarily due to the favourable bonding properties. At the same time, thiol-gold bonds exhibit large variations and fluctuations that are reflected in unreliable transport measurements [27]. As will be explained in the next section, single molecule measurements are based on a statistical analysis of large numbers of equivalent molecular junctions. It has been shown that the resulting conductance distribution spreads over one order of magnitude, when using thiols as docking groups. One of the origins of that are differences in the binding geometry at the contact, which are less pronounced when using, for instance, amines (NH_2) [27], [45]. Therefore, the chemical group used as anchor can be crucial in obtaining reproducible molecular junctions.

A combined experimental and theoretical study of anchoring groups in electrical conduction through single-molecule junctions was done by Zotti et al. [16]. They investigated tolane molecules attached to gold via thiol, nitro and cyano docking groups, showing that anchor groups influence not only the strength of the metal-molecule coupling, but also the position of the molecular energy levels. Another experimental and theoretical work by Hong et al. [50] compared the effect of thiol, pyridyl, amine and nitril anchoring groups revealing a hierarchy considering junction formation probability and stability: $PY > SH > NH_2 > CN$.

Lörtscher et al. [44] experimentally investigated the influence of metal-molecule coupling on transport through single-molecule junctions using thiol and isocyano linkers connecting benzene molecules to gold, applying the MCBJ technique. They found isocayno groups to be the better docking group, resulting in fewer instabilities in the current-voltage curves and higher surface mobility of the molecules arranging on the gold electrodes. They reached similar currents in the order of $25 - 40$ nA at 1.2 V for the thiol docking group

and $20 - 30$ nA at 1.2 V for isocyanide. Koga et al. theoretically investigated electron transport properties through single benzene molecules with cyanide (-CN) and isocyanide (-NC) anchor groups at their para and meta positions [49]. They found larger broadened, transmissive LUMO peaks for isocyanide, resulting from a stronger coupling to the gold electrodes and leading to a higher current of about 6 μA at 1 V, than for the cyanide docking group.

The influence of docking groups was also intensively investigated on the basis of metal-SAM systems for pyridine anchors by Ma et al. [51] or by Heimel et al. [35] comparing -SH, -NC and pyridine.

Not only the type of anchoring group, but also its exact position matters in case of transport calculations, as was shown by Mayor et al. [52] by investigating thiol groups placed in the para or meta position of the last phenyl ring. The latter resulted in a crucially reduced current, due to an interruption of conjugation.

1.4 Experimental Techniques

The final goal of experiments in molecular electronics is to make robust, reproducible and consistent electronic devices, that can be easily manufactured and integrated. A detailed description of experimental techniques can be found in several reccomendable reviews about molecular electronic junctions like [1] and [2]. Here, only an overview about the most common techniques will be given, mainly based on [2] and [5].

Since molecular junctions can be divided into two types, namely single molecule and ensemble, the underlying experimental fabrication techniques can accordingly be subdivided, as shown in Fig. 6. In the red area two examples for single molecule device fabrication can be found and the green area shows common examples for ensemble junctions.

Break junction techniques can be divided into two categories: mechanically controllable break junction MCBJ [9], [10] and electromigrated break junctions [53]. As illustrated in Fig. 7, MCBJs typically consist of a metallic free suspended bridge fixed on top of a bendable substrate. Moving a piezo-controlled rod bends the substrate until the metallic wire is elongated enough to break. Two nano sized electrode surfaces are created. The molecules that are supposed to bridge the gap can either be present in solution or in gas phase. The main advantage of MCBJs is the ability to repeat back-and-forth bending, which allows a large number of measurements that can be evaluated statistically. Since the details of the contact geometry and conformation strongly affect the electrical behaviour of single molecule junctions, and since these local configurations are not known for a specific experiment and vary significantly for each molecule studied [54], one needs a large number of experiments and then draws conclusions on the basis of histograms.

Scanning Tunneling Microscopy (STM) has the ability of combining high-resolution imaging and spatially resolved scanning tunneling spectroscopy, providing the local den-

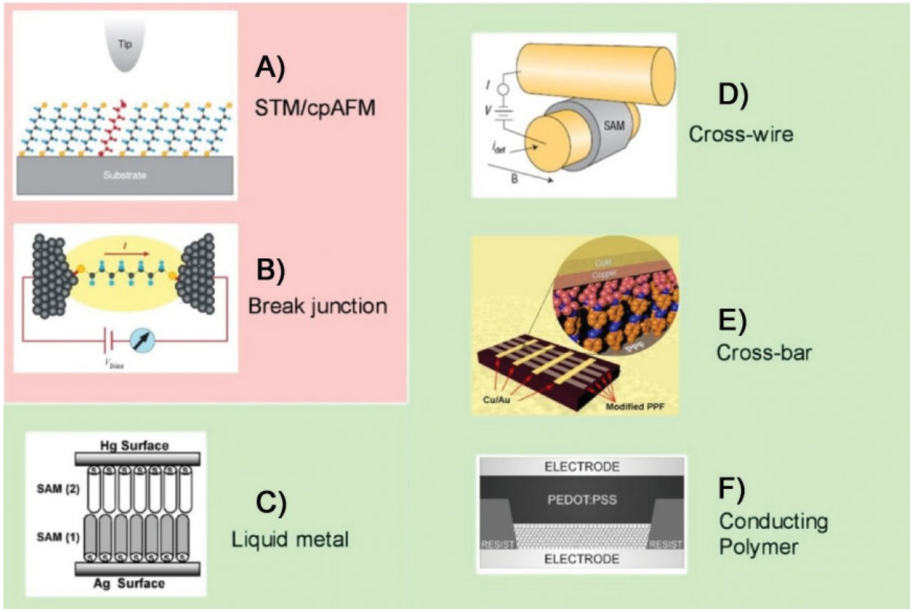

Figure 6: Examples of single molecule (red) and ensemble (green) molecular junctions. A) Single molecule interrogated using an STM or cpAFM tip. B) MCBJ formed by breaking a metallic wire until a gap opens, that is bridged by molecules. C) Liquid-metal junction formed by suspending an Hg drop over a metal surface in a solution of thiol molecules, which adsorb to form monolayers. D) Cross-wire junction formed at the intersection of two cylindrical metallic wires, one of which is coated with a SAM. E) Planar cross-bar junction made by evaporating a metal onto a molecular layer covalently bonded to a carbon substrate F)Junction made using a conductive polymer as the top contact. Reproduced with permission from Ref. [2] ©2012 WILEY-VCH Verlag GmbH&Co.KGaA, Weinheim

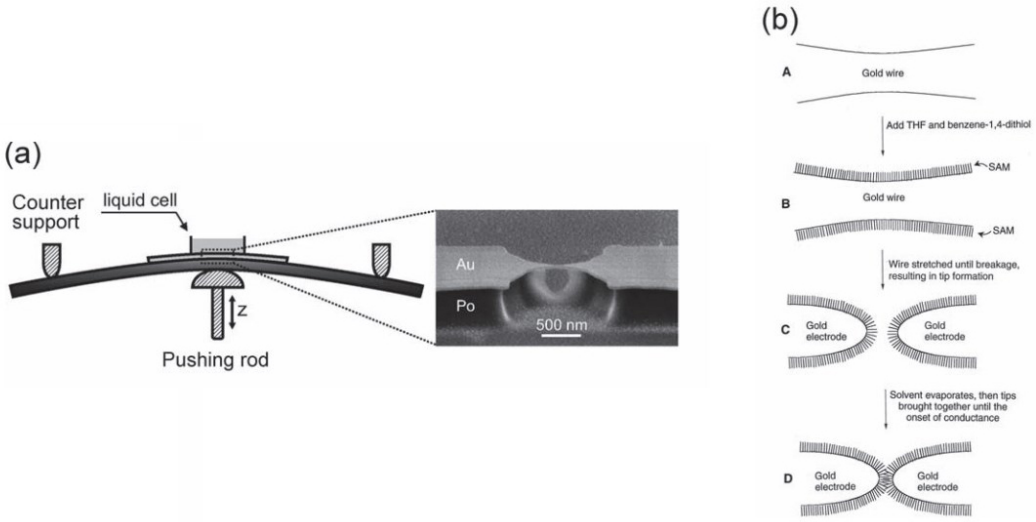

Figure 7: Schematics of the MCBJ principle (a) with the corresponding measurement process (b). Reproduced with permission from Ref. [1] ©2012 WILEY-VCH Verlag GmbH&Co.KGaA, Weinheim

sity of states with atomic resolution. An integration of the STM and the aforementioned break junction leads to a very commonly used technique, referred to as a STM-controllable break junction (STM-BJ) [29], where moving the STM-tip into and out of the contact with a metal surface in a solution containing the molecules, leads to quickly and repeatedly formed junctions, again allowing robust statistical analysis.
In conducting-probe **Atomic Force Microscopy** (CP-AFM) the metal-coated tip acts as the top electrode and is brought into contact with the molecules arranged on a conducting substrate, that acts as the bottom electrode. An external circuit measures current-voltage characteristics.

A main alternative to overcome these statistical fluctuations of single molecule junctions is the ensemble approach, where $> 10^3$ molecules are aligned in parallel between two conducting contacts. Of course, this increases the complexity of the junction and, as was partly discussed in section 1.2, the scaling of single molecules to large area junctions is not that clear. Still, there are several advantages of ensemble junctions over single molecule junctions concerning consistency, mass production and integration into conventional electronics.

One of the main challenges for large area junctions is making the top contact between the metal and the molecular monolayer. In particular one has to avoid metallic filaments penetrating the molecular layer. In fact, approaches like chemical vapour deposition or **liquid metal** junctions often lead to electrical shorts and cannot not eliminate the problem, in spite of improvements combining chemical vapour deposition with strong metal-molecule bonding [55].

Akkerman et al. [56] managed to overcome the penetration of metals into the molecular monolayer by using a highly **conducting polymer** as a top contact, followed by a gold layer, as illustrated in Fig. 6F. The junctions obtained by this technique show excellent stability and the desired reproducibility.

Crossed-wire junctions are formed when molecules bridge the gap between two cylindrical metal fibres (Fig. 6D), producing single molecule junctions as well as ensemble junctions. Using the magnetic Lorentz force the gap between the metallic wires (one of which is coated with a monolayer) can be tuned.

2 Theoretical Concepts

In this chapter, some basic theoretical considerations and derivations will be presented that are needed to calculate the relevant properties of the systems investigated in this thesis. The theoretical fundamentals of density functional theory (DFT) as well as a basic understanding of how DFT-based programs work will be given. The transport description will be theoretically discussed within the Landauer-Büttiker formalism. Since a combination of DFT and Green's function techniques will finally provide the current through molecular junctions, a theoretical description of that approach will be provided.

2.1 Density Functional Theory

Density **F**unctional **T**heory (**DFT**) is presently the most successful approach to investigate the electronic structure of complex many-body systems in physics and chemistry. Its application ranges from atoms, molecules and solids to nuclei and quantum and classical fluids. DFT is widely used to predict a great variety of molecular properties, like molecular structures, vibrational frequencies, ionization energies, electric and magnetic properties. More important for this work, DFT is at the moment the theoretical approach with the largest impact on molecular electronics.

Within this theory, the properties of a many-electron system can be determined by using functionals of the electron density, meaning that in principle one scalar function of position determines all properties of the system in its ground state. This is a big advantage over traditional methods, like e.g. Hartree-Fock theory, that are based on the complex many-electron wavefunction.

In this chapter an overview of the theoretical background of DFT shall be given. Additionally, some important facts about the programs that were used are contained. More practical information on the codes will be given in section 5. In this work two DFT based codes where applied: The **V**ienna **A**b-initio **S**imulation **P**ackage **VASP** [57] and the **S**panish **I**nitiative for **E**lectronic **S**imulations with **T**housands of **A**toms **SIESTA** [58].

There is very much recommendable literature on DFT. Of course the original papers of P. Hohenberg and W. Kohn [59], and W. Kohn and L. J. Sham [60], as well as Kohn's Nobel lecture [61]. Advisable books on DFT would be [5], [62] and [63]. The following is mainly based on [5], [62] and [64].

2.1.1 Schrödinger Equation

The ultimate goal and at the same time major challenge in most theoretical approaches in solid state physics and quantum chemistry is the solution of the non-relativistic, time-independent Schrödinger equation for the many-electron wave function Ψ,

$$\hat{H}\Psi(\mathbf{r}_1, \cdots, \mathbf{r}_N, \mathbf{R}_1, \cdots, \mathbf{R}_M) = E\Psi(\mathbf{r}_1, \cdots, \mathbf{r}_N, \mathbf{R}_1, \cdots, \mathbf{R}_M) \tag{2.1}$$

where $\hat{H}$ is the Hamiltonian for a molecular system in the absence of magnetic fields containing M nuclei and N electrons. $\mathbf{r}_i$ and $\mathbf{R}_I$ are the positions of the electrons and nuclei, respectively.

$$\hat{H} = -\frac{\hbar^2}{2m_e}\sum_{i=1}^{N}\nabla_i^2 - \frac{\hbar^2}{2M_I}\sum_{I=1}^{M}\nabla_I^2 - \sum_{i=1}^{N}\sum_{I=1}^{M}\frac{Z_I e^2}{|\mathbf{r_i}-\mathbf{R_I}|} + \frac{1}{2}\sum_{i=1}^{N}\sum_{\neq j}^{N}\frac{e^2}{|\mathbf{r_i}-\mathbf{r_j}|} + \frac{1}{2}\sum_{I=1}^{M}\sum_{\neq J}^{M}\frac{Z_I Z_J}{|\mathbf{R_I}-\mathbf{R_J}|} \tag{2.2}$$

The first two terms of $\hat{H}$ describe the kinetic energy of the electrons and the nuclei. The three remaining terms represent the attractive electrostatic interaction between nuclei and electrons and the repulsive potential due to electron-electron and nucleus-nucleus interactions.

A very common simplification of Eq. 2.1 can be achieved using the Born-Oppenheimer approximation. Since the much heavier nuclei move more slowly than the electrons, we can assume a separate motion of electrons and ions and we consider the electrons as moving in the field of the fixed nuclei.

The problem reduces to the Schrödinger equation for the electronic part

$$\hat{H}_{elec}\Psi_{elec} = E_{elec}\Psi_{elec} \tag{2.3}$$

where now the electronic Hamiltonian $\hat{H}_{elec}$ consists of the kinetic energy of the electrons $\hat{T}$, the electrostatic interaction between electrons and nuclei $\hat{V}$ and the electron-electron interaction $\hat{U}$.

$$\hat{H}_{elec} = \hat{T} + \hat{V} + \hat{U} = -\frac{\hbar^2}{2m_e}\sum_{i=1}^{N}\nabla_i^2 - \sum_{i=1}^{N}\sum_{I=1}^{M}\frac{Z_I e^2}{|\mathbf{r_i}-\mathbf{R_I}|} + \frac{1}{2}\sum_{i=1}^{N}\sum_{\neq j}^{N}\frac{e^2}{|\mathbf{r_i}-\mathbf{r_j}|} \tag{2.4}$$

The total energy E_{total} is represented by the sum of the electronic part E_{elec} and the constant nuclear repulsion term E_{nuc}.

$$E_{total} = E_{elec} + E_{nuc} \qquad\qquad E_{nuc} = -\tfrac{\hbar^2}{2M_I}\textstyle\sum_{I=1}^{M}\nabla_I^2 + \frac{1}{2}\sum_{I=1}^{M}\sum_{\neq J}^{M}\frac{Z_I Z_J}{|\mathbf{R_I}-\mathbf{R_J}|}$$

Although the Born-Oppenheimer approximation helped to decrease the number of degrees of freedom, it is still challenging to solve Eq. 2.3, because of the fact that the wavefunction $\Psi = \Psi(\mathbf{r}_1, \cdots, \mathbf{r}_N)$ is still a function of $4N$ electron coordinates including spin. Since typical problems in solid state physics deal with about $N = \mathcal{O}(10^{24})$ particles, an exact solution cannot be obtained.

Methods based on the expansion of the wavefunction in Slater determinants, like the Hartree-Fock-method give excellent results for sufficiently small molecules, like H_2. For large systems, the core advantage of DFT plays out, namely that the whole problem can be expressed entirely in terms of the electron density $n(\mathbf{r})$, as will be seen in the next chapter.

2.1.2 Hohenberg-Kohn Theorem

A very crude theory that was developed in 1927 shortly after the introduction of the Schrödinger equation is the so called Thomas-Fermi model [65], which can be viewed as a precursor to modern DFT. Based on the uniform electron gas, it stands separate from wave function theory as being formulated in terms of the electron density distribution $n(\mathbf{r})$ alone.

This idea was picked up in 1964 by P. Hohenberg and W. Kohn and led to the famous Hohenberg-Kohn Theorems [59], whose main statement is, that $n(\mathbf{r})$ implicitly determines all properties derivable from $\hat{H}$ through the solution of the Schrödinger equation. More precisely, ground state properties of a many-electron system are uniquely determined by an electron density that only depends on three spatial coordinates. In this way, the many-body problem of N electrons with 3N spatial coordinates can be reduced to 3 spatial coordinates through the use of functionals of the electron density.

The first Hohenberg-Kohn Theorem states: *"The ground state energy of a system of interacting electrons is a unique functional of the electron density"* [64], meaning that there is a unique relationship between the ground-state electron density $n_0(\mathbf{r})$ and the ground-state wavefunction $\Psi_0(\mathbf{r_1} \cdots \mathbf{r_N})$.

While the first theorem proofs the existence of the functional, the second Hohenberg Kohn Theorem defines its property: *"The electron density that minimizes the energy of the overall functional is the true ground-state electron density"* [64].

According to these theorems, the expectation value of the Hamiltonian of Eq. 2.4, that will be from now on stated as $\hat{H}$ can be written as

$$< \Psi|\hat{H}|\Psi >= E[n(\mathbf{r})] \tag{2.5}$$

where $E[n(\mathbf{r})]$ is the total energy functional of the electron density. If the exact form of this functional could be established, the variational problem to be addressed would be

$$\frac{\delta E[n(\mathbf{r})]}{\delta n}\Big|_{n=n_0} = 0 \tag{2.6}$$

with the constraint

$$\int d^3 r n(\mathbf{r}) = N. \tag{2.7}$$

The electron density that minimizes the energy-density functional and, therefore, corresponds to the minimum energy E_0 is the ground-state density.

To proceed in practical calculations, the total energy as a functional of the electron density can be written as

$$E[n(\mathbf{r})] = T[n(\mathbf{r})] + V[n(\mathbf{r})] + U[n(\mathbf{r})] \tag{2.8}$$

where

$$V[n(\mathbf{r})] = \int v(\mathbf{r})n(\mathbf{r})d\mathbf{r} \tag{2.9}$$

and, therefore

$$E[n(\mathbf{r})] = \int d\mathbf{r}v(\mathbf{r})n(\mathbf{r}) + F_{HK}[n(\mathbf{r})], \tag{2.10}$$

which seperates $E[n(\mathbf{r})]$ into contributions that depend on the actual system (the potential energy due to electron-nuclei attraction) and those which are universal, $F_{HK}[n(\mathbf{r})]$.

Finding what is called the universal functional $F_{HK}[n(\mathbf{r})] = T[n(\mathbf{r})] + U[n(\mathbf{r})]$ is the holy grail of DFT. The explicit form of both functionals $T[n(\mathbf{r})]$ and $U[n(\mathbf{r})]$ is unknown, but from the latter the classical character $J[n(\mathbf{r})]$ can be extracted,

$$U[n(\mathbf{r})] = \frac{e^2}{2}\int d\mathbf{r}\int d\mathbf{r}'\frac{n(\mathbf{r})n(\mathbf{r}')]}{|\mathbf{r}-\mathbf{r}'|} + E_{ncl}[n(\mathbf{r})] = J[n(\mathbf{r})] + E_{ncl}[n(\mathbf{r})] \tag{2.11}$$

Eq. 2.11 devides the electron-electron interaction $U[n(\mathbf{r})]$ into a classical contribution, the electrostatic energy or Hartree energy $J[n(\mathbf{r})]$ and into a non-classical contribution, the self-interaction correction, the exchange and Coulomb correlation $E_{ncl}[n(\mathbf{r})]$ [5]. Finding explicit expressions for the kinetic energy $T[n(\mathbf{r})]$ and $E_{ncl}[n(\mathbf{r})]$ is the major challenge in DFT.

2.1.3 Kohn-Sham Approach

In 1965 W. Kohn and L. J. Sham suggested to calculate the exact kinetic energy of a non-interacting reference system with the same density as the real, interacting one [60]. The total energy functional can then be expressed as

$$E[n(\mathbf{r})] = T_S[n(\mathbf{r})] + J[n(\mathbf{r})] + \int v(\mathbf{r})n(\mathbf{r})d\mathbf{r} + E_{xc}[n(\mathbf{r})] \tag{2.12}$$

where $T_S[n(\mathbf{r})]$ is the kinetic energy functional of the non-interacting electron system moving in an effective Kohn-Sham potential V_{KS}. Since T_S is not equal to the true kinetic energy of the system, Kohn and Sham introduced the so called exchange and correlation energy $E_{xc}[n(\mathrm{r})]$ to account for everything that is unknown.

$$E_{xc}[n] \equiv (T[n] - T_S[n]) + (U[n] - J[n]) \tag{2.13}$$

This was a way to reduce the many-body problem into a one-electron problem. The resulting single-particle Kohn-Sham equations obtained by minimizing the total energy with respect to the electron density are

$$\Big[-\frac{\nabla^2}{2} + V_{KS}[n(\mathbf{r})]\Big]\Psi_i(\mathbf{r})] = \epsilon_i\Psi_i(\mathbf{r}) \tag{2.14}$$

where

$$V_{KS}(\mathbf{r}) = V + \int d\mathbf{r} \frac{n(\mathbf{r}')}{|\mathbf{r} - \mathbf{r}'|} + \frac{\delta E_{xc}[n(\mathbf{r})]}{\delta n(\mathbf{r})} = V + V_{Hartree} + V_{xc}. \tag{2.15}$$

The Kohn-Sham potential V_{KS} has a functional dependence on n. The latter is defined in terms of the Kohn-Sham wave functions

$$n(\mathbf{r}) = \sum_{i}^{occ} \|\Psi_i(\mathbf{r})\|^2. \tag{2.16}$$

Once the potential V_{KS} is known and, therefore, an expression for E_{xc}, it can be inserted into the Kohn-Sham-equations, which determine the Kohn-Sham orbitals and hence the ground state density and the ground state energy. But since V_{KS} itself depends on n, these equations have to be solved self-consistently, as is shown in Fig. 8. Starting with an initial density guess n(r), the effective potential V_{KS} can be determined (Eq. 2.15). With that one can solve the Kohn-Sham equation (Eq. 2.14) and from its solution, the Kohn-Sham orbitals and the new electron density can be calculated (Eq. 2.16). This will be self-consistently repeated until a convergence criterion is achieved. From the converged ground-state density one can get the ground-state energy.

An important aspect that has to be kept in mind is that, if one knows the exchange correlation energy exactly, the Kohn Sham strategy would lead to the exact energy. Therefore, people are widely attempting to find the best approximation for exchange correlation functionals.

2.1.4 Exchange-Correlation Functionals

After transforming the many-body problem into the effective single-electron problem, finding the best expression for the unknown exchange-correlation functional $E_{xc}[n(\mathbf{r})]$ is the major challenge in DFT. Very common and widely used approximations are the local density approximation (LDA) and the generalized gradient approximation (GGA) [5].

Derived from the homogeneous electron gas, LDA is the simplest approach and at the same time basis of all approximate exchange-correlation functionals. This method assumes electrons to move in a positive background charge distribution such that the total ensemble is neutral [5].

$$E_{xc}^{LDA}[n(\mathbf{r})] = \int n(\mathbf{r}) \epsilon_{xc}^{hom}(n(\mathbf{r})) d\mathbf{r} \tag{2.17}$$

$\epsilon_{xc}^{hom}(n(\mathbf{r}))$ is the exchange-correlation energy per particle of a uniform gas with the electron density $n(\mathbf{r})$, that is weighted with the probability $n(\mathbf{r})$ that there is an electron at this position.

A more accurate approximation can be achieved by including the gradient of the electron density (GGA). Typical numerous forms for this case would be the Perdew-Wang functional (PW91) [66] and the Perdew-Burke-Ernzerhof functional (PBE) [67]. In this

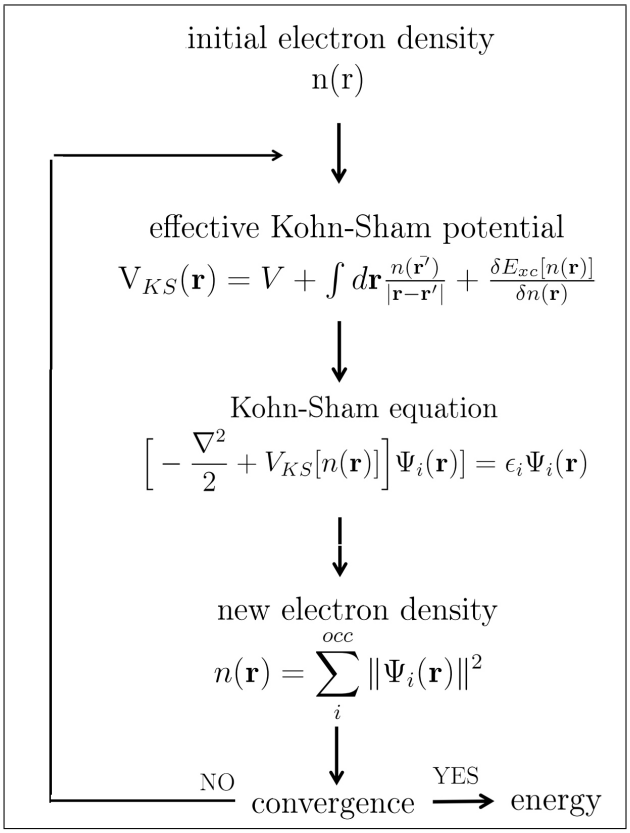

Figure 8: Schematic representation of the self-consistent Kohn-Sham cycle. Starting with an initial density guess n(r), the effective potential V_{KS} can be determined. With that one can solve the Kohn-Sham equation. From its solution, the Kohn-Sham orbitals $\Psi(\mathbf{r})$, the new electron density can be calculated. This procedure will be repeated self consistently until a chosen convergence criterion is fulfilled and the ground-state energy can be deduced.

thesis, the PBE functional has been used within VASP as well as SIESTA.

2.1.5 Basis Sets

To solve the Kohn-Sham equations, its solutions, the Kohn-Sham wave functions need to be expanded in a set of well chosen basis functions. A general expression for a proper basis has the following form [62]

$$\Psi_i(\mathbf{r}) = \sum_t a_t(\mathbf{k})\varphi_{k,t}(\mathbf{r}) \tag{2.18}$$

where $b_{i,k}$ is a set of coefficients and the functions $\varphi_k(\mathbf{r})$ are called the basis set.

There are two big groups concerning the choice of basis functions used to expand the solutions of the Kohn-Sham equations. Atomic-independent ones, typically plane waves, that are particularly well suited for extended systems and basis sets which use atom-centered functions, usually relatively compact ones.

Appropriate boundary conditions need to be specified when solving Eq. 2.14. VASP and SIESTA apply periodic boundary conditions, where the system of interest is assumed to be represented by a box of atoms, the unit cell, which is periodically repeated in all three spatial directions. The unit cell is described by three vectors $\mathbf{a_1}$, $\mathbf{a_2}$ and $\mathbf{a_3}$, whose reciprocal lattice vectors $\mathbf{b_1}$, $\mathbf{b_2}$, $\mathbf{b_3}$ define the volume Ω of the reciprocal unit cell, also called the first Broullin zone.

$$\mathbf{b_1}.(\mathbf{b_2} \times \mathbf{b_3}) = \frac{(2\pi)^3}{\Omega} \tag{2.19}$$

According to Bloch's theorem, the Kohn-Sham wave functions can be expressed as a product of a plane wave part and a lattice-periodic part

$$\Psi_i(\mathbf{r}) = u_{\mathbf{k}}(\mathbf{r})e^{i\mathbf{kr}}, \tag{2.20}$$

where $\mathbf{k}$ is a vector in reciprocal space. Kohn-Sham equations are mapped into reciprocal space and solved for each value of $\mathbf{k}$ independently. Therefore, a proper k-point sampling needs to be adopted using suitable values of $\mathbf{k}$ in the first Broullin zone. A very common and frequently used Broullin zone sampling in VASP and SIESTA is the so called Monkhorst-Pack Method [68]. There are also other methods and even a way to define k-points per hand, as will be described in detail in section 2.1.6.

For periodic systems, the **plane wave** basis set appears to be the natural choice

$$\Psi_i(\mathbf{r}) = \sum_t a_t(\mathbf{k})\varphi_{k,t}(\mathbf{r}) = \frac{1}{\sqrt{\Omega}}\sum_t a_t(\mathbf{k})e^{i(\mathbf{k}+\mathbf{K}_t)\mathbf{r}}, \tag{2.21}$$

where $\mathbf{K}_t$ are vectors in the reciprocal space. In practical calculations the sum over t needs to be finite. Therefore, only plane waves up to a certain cutoff wave vector are included in the basis set. Accuracy can be systematically enhanced by increasing the number plane

waves one takes into account to represent the wavefunction. Plane wave basis sets are implemented in the **VASP** code, where the number of basis functions can be controlled by a single parameter called the `ENCUT` parameter. It has to be converged for every system in question to guarantee correctness of the results.

The second group are atom-centred basis functions, so called localized **atomic orbitals**. They are, e.g., implemented in the **SIESTA** code. Using localized atomic orbitals is essential to make SIESTA to an order-N algorithms, where computer time and memory scale linearly with the simulated system size [69]. Order-N methods rely heavily on the sparsity of $\hat{H}$ and overlap matrices, which can only be achieved by strictly confined basis orbitals, that are zero beyond a certain cutoff radius.
Basis functions consisting of a linear combination of localized numerical atomic orbitals (LCAO) can be expressed as [70]

$$\Psi_{\mathbf{k}}(\mathbf{r}) = \sum_n e^{i\mathbf{k}\mathbf{R}_n} \varphi_n(\mathbf{r} - \mathbf{R}_n) \tag{2.22}$$

where the φ_n can be expressed as a product of a radial function times a spherical harmonic. Therefore, restrictions for the basis sets are (i) the functions have to be atomic-like (radial functions multiplied by spherical harmonics), and (ii) they have to be of finite range (radial function becomes zero beyond a certain cutoff). One can either create ones own basis or use a hierarchy of basis sets established by SIESTA. Following the nomenclature of quantum chemistry there are single ζ to multiple ζ basis sets where one can add polarization by choice. Each ζ orbital corresponds to the same spherical harmonic but with different radial function (single- ζ SZ, double-ζ DZ, triple-ζ TZ for 1, 2 and 3 radial functions). Including polarization leads to single-zeta-polarized SZP, double-zeta-polarized DZP etc. SIESTA offers standard basis functions from SZ and SZP to DZ and DZP. The range of these localized atomic orbitals can be set by a parameter called `PAO.EnergyShift`. This is a parameter describing the energy increase experienced by the pseudo-atomic orbitals (PAO's) when they get confined to finite range [71]. The energy is inversely proportional to the real space extension of the basis, described by the cutoff radius r_c. Details on different basis sets and cutoff will be given in chapter 6.2.1.

2.1.6 k-point Sampling

Since all functions with crystal symmetry are repeated beyond the first Broullin zone, the corresponding k-point grid is also constrained to this area. So all observables, such as energy, charge densities or potentials, are calculated as an integral over the 1.BZ that is converted into a sum over discrete points in k-space. The error induced by calculating the electronic states only at a finite number of k-points can be systematically reduced by increasing the density of the k-point mesh. Since each additional k-point means a new self-consistent Kohn-Sham system, accuracy should be maximized while reducing the number of k-points. Extensive descriptions of k-point generation in VASP and SIESTA can be found in the corresponding manuals [72] and [71] respectively.

k-point grids in VASP
There are several possibilities proposed in the literature to define k-points [68], [73], [74]. In VASP one can either use the automatic k-mesh generation, which seperatly offers different schemes, or one can enter all k-points explicitly. K-points settings are specified in the `KPOINTS` input file [72].

For automatic mesh generation, a typical format for this file is:

```
Nin_cov100      ! Comment
0               ! number of k-points = 0 -> automatic generation of k-points
Monkhorst       ! automatic generation scheme: Monkhorst, Gama, Auto
8 8 1           ! 8x8x1 grid
0 0 0           ! optional shift of the mesh
```

The first line is treated as a comment. If the second line equals zero, k-points will be generated automatically either using the Monkhorst Pack scheme [68] or if defined as `Gamma` the Γ centred method. The Monkhorst Pack scheme produces an equally spaced mesh in the 1.BZ with distributed k-points [68]

$$k = N_1\mathbf{b_1} + N_2\mathbf{b_3} + N_3\mathbf{b_3}. \tag{2.23}$$

$\mathbf{b_1}, \mathbf{b_2}, \mathbf{b_3}$ are the reciprocal lattice vectors and

$$N_i = \frac{2p_i - q_i - 1}{2q_i} \tag{2.24}$$

with $p_i = 1, 2, \cdots, q_i$ where q_i are the numbers of k-points in each direction.
(One can also use a fully automatic generation scheme 'Auto', that generates Γ centred Monkhorst-Pack grids, where no explicit number of subdivisions has to be declared, but this scheme was not used in this thesis.)

The third line either starts with 'M' or 'm' selecting the original Monkhorst Pack scheme or with 'G' or 'g' for generating meshes with their origin at the Γ point. The fourth line states the subdivisions N_1, N_2, N_3 along the reciprocal unit cell vectors. An optional, additional shift of the whole mesh can be introduced in multiples of the length of the reciprocal lattice vectors by entering the appropriate value in the fifth line.

The practical application of these different schemes will become aparent in section 3.3 where some investigated systems with different sized unit cells will be discussed. With increasing size of the unit cell, the volume of the 1.BZ becomes smaller and, therefore, fewer k-points are needed.

Since there were some problems with automatic generation, the possibility of explicitly entering k-points was also investigated. In the case of entering all k-points explicitly the `KPOINTS` file must contain the coordinates and relative weights for each k-point to create the grid. This will be also discussed in more detail in chapter 3.3 for exemplary systems investigated in this thesis.

k-point grids in SIESTA
In SIESTA there is no possibility of explicitly entering the desired k-point mesh, but there is of course the Monkhorst-Pack scheme defined in the data block of the corresponding `.fdf` Input file as [71]:

```
%block k_grid_Monkhorst_Pack
Mk(1,1) Mk(2,1) Mk(3,1)   dk(1)
Mk(1,2) Mk(2,2) Mk(3,2)   dk(2)
Mk(1,3) Mk(2,3) Mk(3,3)   dk(3)
%endblock k_grid_Monkhorst_Pack
```

where `Mk(i,j)` are integers defining the grid and `dk(i)` are again optional displacements of the whole mesh. From Mk the k-grid supercell will be defined. Details on SIESTA supercells will be given in section 5.

Another possibility for defining a mesh of k-points in SIESTA is by setting one single parameter, the so called `kgrid_cutoff`, which defines the fineness of the k-grid in the first Broullin zone, chosen in an optimal way according to the method of Moreno and Soler [74].

2.2 Transport in Nanocontacts

Perhaps the most popular and widely used method for describing transport in nano scale devices is the Landauer formalism [75], also known as the scattering approach. This theoretical model starts dominating when the size of the contact becomes so small that the wave nature of electrons can no longer be ignored, i.e. when entering the full quantum limit. The main approximation introduced by Rolf Landauer in the late 1950's is regarding electrons as non-interacting particles, also neglecting phonon contributions and, therefore, assuming coherent transport, meaning that there are no phase-breaking scattering processes involved. If inelastic interactions can be ignored, a transport problem can be viewed as a scattering problem. For this reason transport properties like electrical conductance get related to the transmission probability for an electron to cross the system. So the Landauer formula states "conductance is transmission". To determine the total conductance G, one has to solve the Schrödinger equation, find the current-carrying eigenmodes, calculate their transmission values and sum up their contributions. G is the given by

$$G = \frac{2e^2}{h} \sum_{n=1}^{N} T_n = G_0 \sum_{n=1}^{N} T_n, \tag{2.25}$$

where $G_0 = 2e^2/h$ $(12.9\,\mathrm{k\Omega})^{-1}$ is the quantum unit of conductance and the summation is performed over all available conduction modes, whose individual transmissions are T_n.

Derivation of the Landauer Formula
On basis of Ref. [5], a heuristic derivation of the Landauer formula shall be obtained. In typical transport experiments on molecular junctions the organic molecule is connected to macroscopic leads allowing the injection of currents and fix voltages. The scattering

approach relates transport properties into transmission and reflection probabilities of incoming waves impinging on a potential barrier. While the electrodes act as ideal electron reservoirs in thermal equilibrium, they incorporate all inelastic scattering processes entering in the description in terms of boundary conditions.

An incoming plane wave impinging on a one-dimensional potential, simulating the central part of the junctions, gets partially reflected and partially transmitted with probabilities r and $T = |t|^2$ respectively. The electrical current density J_k carried by one electron can be described by its wavefunction Φ

$$J_k = \frac{-e\hbar}{2mi}\Big[\Phi^*(x)\frac{d\Phi}{dx} - \Phi(x)\frac{d\Phi^*}{dx}\Big] = \frac{-e}{L}v(k)T(k) \tag{2.26}$$

with the group velocity $v(k) = \hbar k/m$, the length of the system L and the transmission probability T. Since in a molecular device many electrons contribute to the current, a sum over k has to be introduced. Additionally, the Pauli principle has to be taken into account by introducing a factor $f_L(k)[1 - f_R(k)]$, where $f_{L/R}$ are the Fermi functions of the electron reservoirs on the left/right side of the potential barrier. This factor allows, only initially occupied states on the left and empty ones on the right to contribute to the current. The Fermi functions are connected to the corresponding chemical potentials μ, that can be shifted by applying a voltage.

Alltogether, after converting the sum into an integral and changing from variable k to energy E, one gets a left-to-right current density $J_{L\to R}$, as well as a right-to-left current density $J_{R\to L}$:

$$J_{L\to R} = \frac{e}{h}\int T(E)f(E-\mu_L)[1-f(E-\mu_R)]dE \tag{2.27a}$$

$$J_{R\to L} = \frac{e}{h}\int T(E)f(E-\mu_R)[1-f(E-\mu_L)]dE \tag{2.27b}$$

The total voltage dependent current $I(V)$ can then be simply expressed by the difference of the current density from left to right and the one from right to left, resulting in the famous Landauer formula:

$$I(V) = \frac{2e}{h}\int T(E)[f(E-\mu_L) - f(E-\mu_R)]dE, \tag{2.28}$$

with the corresponding Fermi function for the left or right lead given by

$$f(E-\mu_{L,R}) = \frac{1}{1+exp\big[\frac{E-\mu_{L/R}}{k_BT}\big]}. \tag{2.29}$$

Fig. 9 shows the corresponding electronic situation of a metal-molecule-metal junction for zero bias (a) and with an applied bias V (b) that is represented as the difference of the left and right chemical potential $\mu_L - \mu_R = eV$. Eq. 2.28 clearly illustrates the close relation between current and transmission in this simplest version of the Landauer formula. To get the charge transport characteristics, an expression for the transmission function $T(E)$ of the system has to be obtained. This will be done by combining DFT with Green's

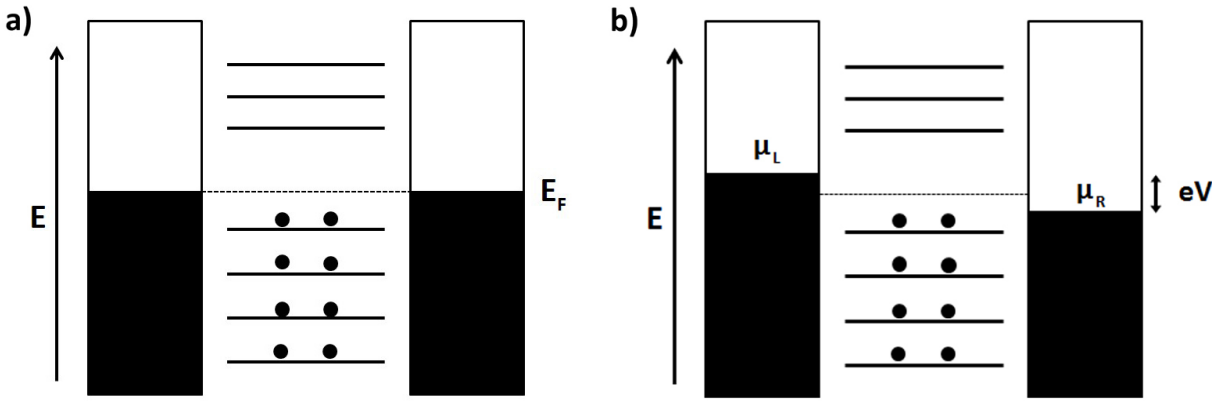

Figure 9: Schematic representation of the electronic structure of the metal-molecule-metal junction with (a) zero bias and (b) an applied bias V, where $\mu_L - \mu_R = eV$

Function techniques, as will be seen in the next chapter.

2.3 Green's Function Techniques

Since transport in nano devices can be described on the atomic level, a combination of **N**on **E**quilibrium **G**reen's **F**unctions NEGF and DFT leads to a very advantageous description of electronic transport characteristics. For coherent transport the NEGF formalism will reduce to the well known Landauer formula. While other methods have limitations concerning (i) the geometric restriction to either finite or periodic systems and (ii) the need of thermal equilibrium, combined NEGF and DFT calculations are able to describe non-periodic and infinite systems at finite bias in non-equilibrium situations.

In this work an extension of the aforementioned SIESTA code, the non-equilibrium electronic structure code TRANSIESTA [76] was used to calculate some of the transport characteristics. With this program the electronic structure of open systems consisting of a finite structure sandwiched between to semi-infinite metallic leads can be described. A finite bias can be applied between the leads to drive a finite current. But since there were many problems with convergence in applying this program to the systems investigated here, a program stemming from a cooperation between Georg Heimel and David A. Egger was applied. This code is called $\text{SIESTA}_{\text{TS}}$, since it is based on the SIESTA code and calculates transport properties at zero bias. A detailed description concerning practical applications will be given in chapter 5.

Regarding literature there are several recommendable articles, e.g. by S. Datta [77], [78], as well as a very comprehensible description by M.Paulsson [79]. The following theoretical description partly stems from [76] and [79].

2.3.1 Screening Approximation

To obtain transport characteristics a separation of the investigated open systems into three parts has to be done, as it is shown in Fig. 10. Two semi-infinite electrodes (a left

and a right one) serving as electron reservoirs are coupled via a contact region, which is often called central region. By including a few layers of the metal in the central region, surface effects due to perturbations of the molecule at the contact can be avoided and the contact gets sufficiently large to include screening.

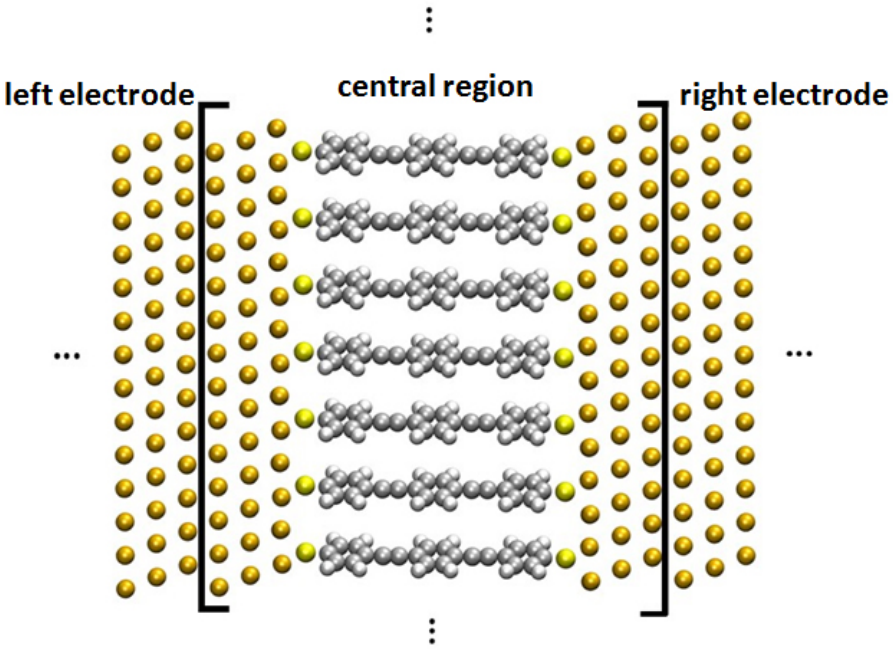

Figure 10: Molecular junction seperated into left electrode, central region and right electrode

The semi-infinite leads have a regular periodic structures in transport direction, while the central region is of finite size in z-direction. The incorporation of the influence of the infinitely extended leads on the finite size central region is the basic mission of the Green's function technique.

By using the so called screening approach, the total Hamiltonian of the system shown in Fig. 10 can be written as [76]

$$\mathbf{H}^{tot} = \begin{pmatrix} \mathbf{H}_L & \mathbf{H}_{LC} & 0 \\ \mathbf{H}_{CL} & \mathbf{H}_C & \mathbf{H}_{CR} \\ 0 & \mathbf{H}_{RC} & \mathbf{H}_R \end{pmatrix} = \begin{pmatrix} \mathbf{H}_L & \boldsymbol{\tau}_L & 0 \\ \boldsymbol{\tau}_L^\dagger & \mathbf{H}_C & \boldsymbol{\tau}_R^\dagger \\ 0 & \boldsymbol{\tau}_R & \mathbf{H}_R \end{pmatrix} \tag{2.30}$$

where $\mathbf{H}_L$, $\mathbf{H}_C$ and $\mathbf{H}_R$ are the Hamiltonian matrices for the left electrode, the central region and the right electrode respectively. $\mathbf{H}_{CL} = \mathbf{H}_{LC}^\dagger = \boldsymbol{\tau}_L$ and $\mathbf{H}_{RC} = \mathbf{H}_{CR}^\dagger = \boldsymbol{\tau}_R$ describe the interactions between the left/right electrode with the central region. The central region is large enough, so there is no direct interaction between the two electron reservoirs and, therefore, no cross terms $\boldsymbol{\tau}$ for the different electrodes. Notice that $\mathbf{H}_{L/R}$, $\mathbf{H}_{LC}$ and $\mathbf{H}_{CR}$ are all matrices of infinite dimension.

After partitioning the system into these three different regions we want to solve the

Schrödinger equation

$$\mathbf{H^{tot}}\mathbf{\Psi} = E\mathbf{S}\mathbf{\Psi} \tag{2.31}$$

where the overlap matrix $\mathbf{S}$ includes the effect of non orthogonal basis functions, where $\mathbf{S}$ is not the identity matrix. Solving the whole eigenvalue problem turns out to be a very difficult task. Therefore, Green's functions are introduced in the next section, from which most properties of the system can be calculated.

2.3.2 Green's Functions and Self Energies

To solve problems like Eq. 2.31 the retarded Green's function $\mathbf{G}^R$ corresponding to the Hamiltonian matrix $\mathbf{H}^{tot}$ of Eq. 2.30 is defined by the relation [76]

$$[E^+\mathbf{S} - \mathbf{H}^{tot}]\mathbf{G}^R = \mathbb{1} \tag{2.32}$$

where $E^+ = E + i\eta$ with η being an infinitesimal positive number, $\mathbf{S}$ is the overlap matrix and $\mathbb{1}$ the identity matrix.

Inserting $\mathbf{H}^{tot}$ into Eq.2.32 leads to

$$\begin{pmatrix} E^+\mathbf{S}_L - \mathbf{H}_L & -\boldsymbol{\tau}_L & 0 \\ -\boldsymbol{\tau}_L^\dagger & E^+\mathbf{S}_C - \mathbf{H}_C & -\boldsymbol{\tau}_R^\dagger \\ 0 & -\boldsymbol{\tau}_R & E^+\mathbf{S}_R - \mathbf{H}_R \end{pmatrix} \begin{pmatrix} \mathbf{G}_L^R & \mathbf{G}_{LC}^R & \mathbf{G}_{LR}^R \\ \mathbf{G}_{CL}^R & \mathbf{G}_C^R & \mathbf{G}_{CR}^R \\ \mathbf{G}_{RL}^R & \mathbf{G}_{RC}^R & \mathbf{G}_R^R \end{pmatrix} = \begin{pmatrix} \mathbf{I} & 0 & 0 \\ 0 & \mathbf{I} & 0 \\ 0 & 0 & \mathbf{I} \end{pmatrix} \tag{2.33}$$

A great benefit of this technique is that the Green's Function of the central region $\mathbf{G}_C^R$ - the part of interest- can be calculated without determining the Green's function of the whole system consisting of the electrodes and the central region. After some transformations and matching of terms one can obtain an expression for the retarded Green's function of the central region

$$\mathbf{G}_C^R = (E^+\mathbf{S}_C - \mathbf{H}_C - \mathbf{\Sigma}_L - \mathbf{\Sigma}_R)^{-1} \tag{2.34}$$

where $\mathbf{\Sigma}_{L/R}$ are the so called self-energies including all the effects coming from the coupling between central region and leads. They have the same finite dimension as $\mathbf{H}_C$.

$$\mathbf{\Sigma}_L = \boldsymbol{\tau}_L^\dagger \mathbf{g}_L \boldsymbol{\tau}_L \tag{2.35a}$$

$$\mathbf{\Sigma}_R = \boldsymbol{\tau}_R^\dagger \mathbf{g}_R \boldsymbol{\tau}_R \tag{2.35b}$$

$\mathbf{g}_L = (E^+\mathbf{S}_L - \mathbf{H}_L)^{-1}$ and $\mathbf{g}_R = (E^+\mathbf{S}_R - \mathbf{H}_R)^{-1}$ are the retarded Green's functions of the isolated semi-infinite left and right leads, also called surface Green's functions of the electrodes uncoupled to the device. They are calculated using an efficient iterative method proposed by Sancho et al. [80]. $\mathbf{S}_{R/L}$ are the overlap matrices of the left and right contact.

The physical interpretation of the self-energies $\mathbf{\Sigma}_{L/R}$ can be obtained from their real and imaginary parts [77]. These are associated to the energy level shift Δ and the broadening Γ of the molecular levels when the molecule attaches the semi-infinite leads, as illustrated in Fig. 11.

$$\Delta_{L/R}(E) = \Re\mathbf{\Sigma}_{L/R}(E) \tag{2.36}$$

$$\mathbf{\Gamma}_{L/R}(E) = i(\mathbf{\Sigma}_{L/R}(E) - \mathbf{\Sigma}^{\dagger}_{L/R}(E)) = -2\Im(\mathbf{\Sigma}_{L/R}(E) \tag{2.37}$$

The latter is inversely proportional to the lifetime τ of the electronic states on molecules and gives the self energy its physical meaning. When the molecule is coupled to the electrodes, electrons escape into the leads and spend some time τ in the state localized at the central region. An uncertainty principle between broadening and lifetime can be formulated:

$$\tau\mathbf{\Gamma} = \hbar. \tag{2.38}$$

A large self-energy, resulting from a great influence of the bulk, broadens the states in the corresponding DOS and, at the same time, reduces the sharpness of the peaks, yielding shorter measurable states.

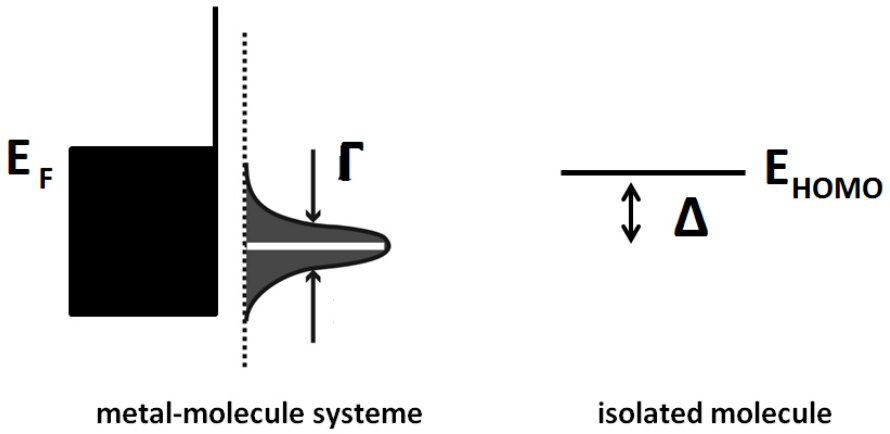

Figure 11: Graphical illustration of the energy level shift Δ and the broadening Γ of the molecular levels when the molecule is attached to the semi-infinite leads

With the use of Green's functions, the infinite-dimensional problem of Eq. 2.31 can be converted into a problem of the dimension of the central region, where the self-energies contain all information about the semi-infinite properties of the electrodes. While $\mathbf{H}_{L,R} + \Sigma_{L/R}$ are received from separate calculations for the bulk systems, $\boldsymbol{\tau}_{L,R}$ and $\mathbf{H}_C$ depend on the non-equilibrium electron density and are determined self-consistently.

2.3.3 Charge Density Matrix and Electrical Current

While an elaborate and comprehensible derivation of the charge density and the electrical current can be found in [76] or in [79], here, only the results will be summarized, to understand the combination of DFT and NEGF.

The density matrix $\mathbf{D}_C$ describes the distributions of electrons and can be separated into an equilibrium part and a non-equilibrium part [76]. It is mainly derived from the

Green's function of the central region $\mathbf{G}_C^R$ and the self energies $\mathbf{\Sigma}_{L/R}$. From $\mathbf{D}_C$ one can get the electron density according to

$$n(\mathbf{r}) = \sum_{\alpha\beta} \Phi_\alpha(\mathbf{r})(\mathbf{D}_C)_{\alpha\beta}\Phi_\beta(\mathbf{r}) \tag{2.39}$$

where $\Phi_\alpha(\mathbf{r})$ are localized atomic orbitals.
Since now an expression for the charge density is found, the NEGF formalism can be combined with DFT, see Fig. 12. So far the NEGF technique taught us to calculate self energies and retarded and lesser Greens Functions in the device region of an open boundary problem from the Hamiltonians of isolated device and metal leads. Now DFT can be used to calculate the self-consistent Kohn-Sham Hamiltonian matrix elements. Therefore, as a first step, a trial charge density is used to compute the Hamiltonian of the central region applying DFT. For the retarded Green's function the Hamiltonian for the central region is needed and also the self-energies. To compute the self-energies one needs to calculate the surface Green's functions for the isolated leads. Afterwards the density matrix D_C and finally the electron density can be obtained. A combination of input and output density gives the new trial densities. For an applied bias, this self-consistent loop is repeated until convergence is achieved.

Finally the current through the central region connected to two metal leads at different chemical potential μ_L and μ_R can be computed from the self-consistent Green's function and self energies,

$$I = \frac{2e}{h} \int \mathrm{Tr}(\mathbf{G}_C^\dagger \mathbf{\Gamma}_R \mathbf{G}_C \mathbf{\Gamma}_L)[f(E-\mu_L) - f(E-\mu_R)]dE \tag{2.40}$$

according to the Landauer formula. From that, an expression for the transmission function can be found as

$$T = \mathrm{Tr}(\mathbf{G}_C^\dagger \mathbf{\Gamma}_R \mathbf{G}_C \mathbf{\Gamma}_L) \tag{2.41}$$

where $\mathbf{\Gamma}_{L/R} = i(\mathbf{\Sigma}_{L/R} - \mathbf{\Sigma}_{L/R}^\dagger)$ are the broadening matrices and $\mu_{L/R} = E_F \pm \frac{eV}{2}$ account for the bias.

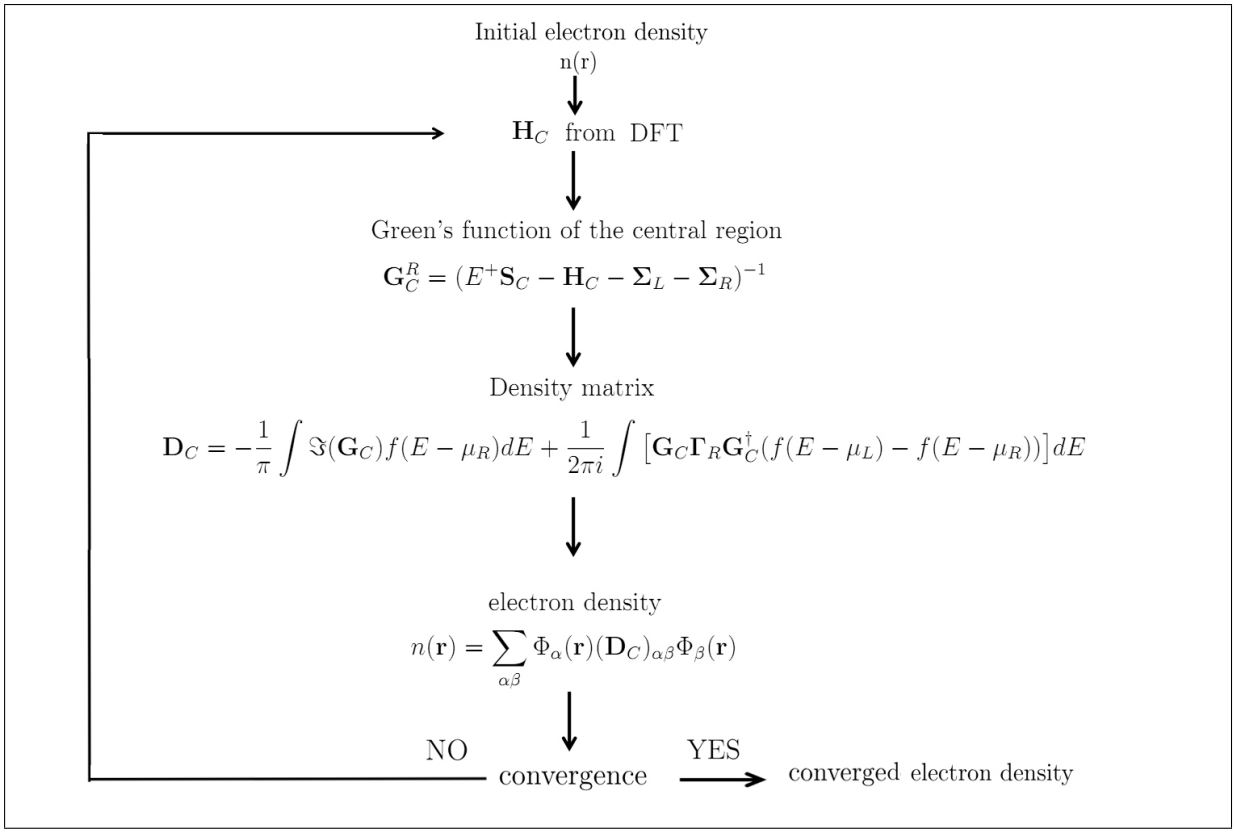

Figure 12: Schematic representation of the combined DFT and NEGF cycle. Starting with an initial density guess n(r), the Hamiltonian of the central region $\mathbf{H}_C$ is calculated applying a usual DFT run. From that together with the self energies $\mathbf{\Sigma}$ produced from the bulk calculations, one can determine the Green's function of the central region G_C^R. Afterwards the density matrix $\mathbf{D}_C$ and the new electron density can be calculated. In case of an applied bias, this new density usually mixed with the old one enters again $\mathbf{H}_C$ and the whole scheme is solved iteratively until convergence is achieved.

3 Investigated Systems

In the following chapter, the molecules investigated in this thesis shall be introduced. After a detailed description of the optimization of their geometry, it will be shown how different coverages of the monolayers comprised between the electrodes can be obtained in the simulation. Since the variation of coverage is strongly connected to k-points, the adaptation of the k-point meshes will be discussed as well.

3.1 Structure of the Molecules

The molecular junctions that were theoretically investigated in this work have the structure shown in Fig. 13. They consist of a left and a right gold electrode (Au(111)), and in between a π-conjugated organic part consisting of molecules, whose chemical structures are shown in Fig. 14.

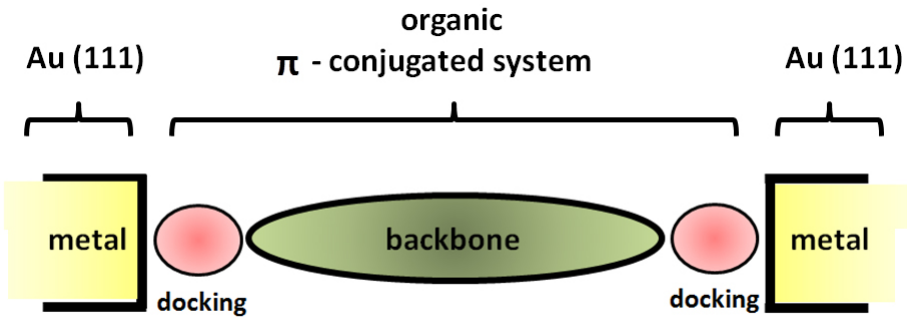

Figure 13: Molecular junction consisting of a left and a right gold electrode and the π-conjugated organic part in between

The first group of junctions that will be studied consists of molecules with internal dipoles distributed along their backbones, as depicted in Fig. 14a. They are denoted as N_{in} and N_{out} and were already introduced in chapter 1.2 as the two isomeric molecules investigated in [38]. Their internal dipoles are introduced by symmetrically replacing two of the carbon atoms by nitrogen in the outermost rings; on the inner side for N_{in} and on the outer side for N_{out}. Since these two isomeric molecules are fully symmetric, they have no net dipole moment. But for N_{in} the dipoles due to the pyrimidine ring and the thiol docking group add up to a local dipole moment on the peripheries, while they essentially cancel for the N_{out} molecule.
The methylene spacers were introduced to decouple the pyrimidine from the thiol docking group and to reduce hybridisation between metal states and π-backbone states.
A peculiarity of the widely used thiol docking group (-SH) is that the sulfur has to be saturated by hydrogen for the free-standing molecule to avoid a radical situation, as was stressed in [81]. Therefore, on a surface the S-H bonding will be replaced by the S-Au bond when connecting to the electrodes.

Expecting a strong influence of the docking group on the electronic structure of the junction [16], the molecules depicted in Fig. 14b were introduced. Referring to their anchor

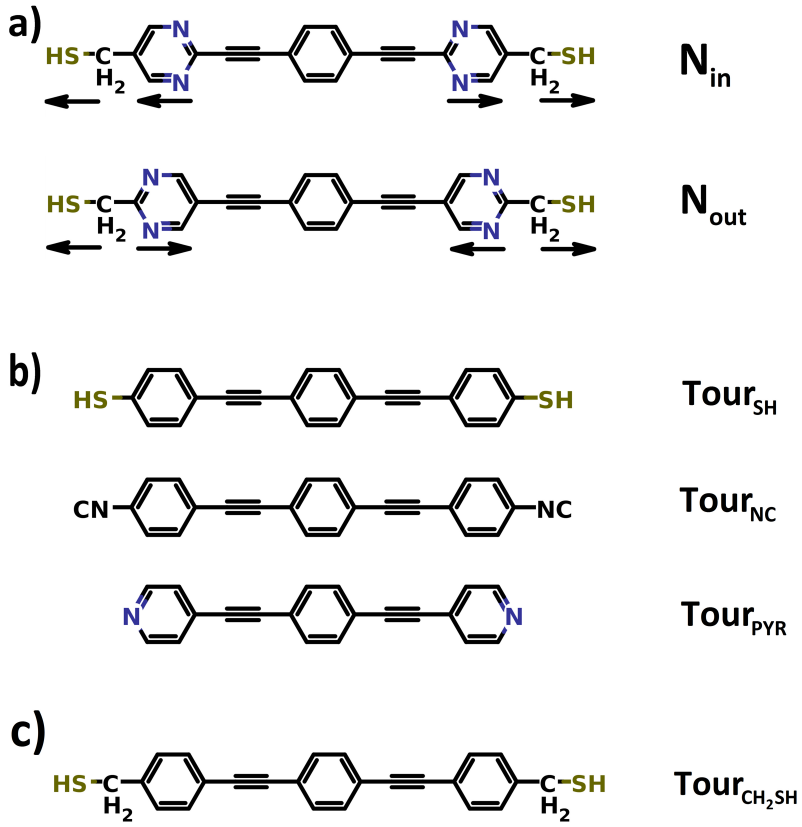

Figure 14: Chemical structures of the investigated systems. a) molecules with internal dipoles N_{in} and N_{out} with arrows indicating their polar bonds; b) molecules with different docking groups $Tour_{SH}$, $Tour_{NC}$ and $Tour_{Pyr}$ with thiol, isocyanide and pyridine anchor groups respectively; c) reference system $Tour_{CH_2SH}$ used for comparison

groups, they will be denoted as Tour_{SH} , Tour_{NC} and Tour_{Pyr} for the thiol, isocyanide and pyridine groups, respectively. Tour_{SH} represents the well known 'Tour wire' molecule, a prototypical model system in molecular electronics, named after James Tour [39]. When bonding this system to an electrode, again the S-H bond will be replaced by a S-Au bond. For Tour_{NC} and Tour_{Pyr} there will be a bond formation between C-Au and N-Au respectively. These docking groups have been frequently investigated by several groups, as was discussed in section 1.3.

To allow a comparison between the results obtained for the systems with internal dipoles, N_{in} and N_{out}, and the ones with different docking groups studied without CH_2 spacers, a reference system needed to be introduced. In comparison to the classical 'Tour-wire', Tour_{SH} , it contains an additional methylene spacer and, therefore, is called $\text{Tour}_{\text{CH}_2\text{SH}}$. Its structure is shown in Fig. 14c.

As a starting point for the DFT based programs (VASP and SIESTA) an input geometry in terms of a unit cell that is periodically repeated in every spatial direction, has to be determined. Therefore, as a first step, a geometry optimization of the entire molecular junction structure has to be performed.

3.2 Geometry Optimization

To determine a stable molecular configuration in a consistent way, geometry optimizations of all molecular junctions were performed before calculating the electronic properties. Geometry optimization or relaxation means starting with a certain configuration of atoms and searching for the structure belonging to a local minimum of the total energy, using the Hellmann-Feynman theorem [82].

There are several programs to optimize geometries. In most of them one starts with a set of ionic coordinates, performs a DFT calculation to find the total energy and its gradient. Then an internal optimizer proposes a next set of ionic coordinates on the basis of the local energy hyperspace. In principle, the optimization problem would be solved, if the total energy hyper surface $E = E(\mathbf{r}_1, \cdots, \mathbf{r}_N)$ was known. Since this is not the case in practical calculations, the total energy is subsequently evaluated again and the process continues until a chosen convergence criterion is met. So for every configuration of ionic positions, the Schrödinger equation is solved for the electrons within the framework of DFT.

In this work an optimization scheme based on the geometrical direct inversion in the iterative subspace method (GDIIS) [83] using GADGET [84], as well as an internal optimization scheme of VASP, the conjugate gradient method [85], were used. In comparison to conventional optimization schemes implemented in VASP, which use Cartesian coordinates, GADGET offers the possibility to perform the geometry optimization process in internal coordinates. These have proven to perform significantly better in many geometry optimization problems when molecules are involved [86], [87]. Geometry optimizations were stopped as soon as the maximum force on the atom fell below 10^{-2} eV/Å. In all op-

timizations the innermost gold layers were also relaxed to include surface reconstructions.

In the case of molecular junctions, geometry relaxation means, optimizing structure as well as the length in z direction to find the optimum position of the docking groups with respect to the electrodes and the optimum electrode-electrode distance. This is of course a strategy, that is only an approximation to the experiment. In experiments the exact geometry of the molecules often significantly varies between individual molecules and, therefore, transport characteristics are evaluated on the basis of statistical analysis. Additionally, the electrodes are not necessarily flat [88], as is assumed in this thesis. Therefore, with geometry optimization one does not try to depict the situation that comes closest to one specific experiment, but rather tries to find a consistent way of describing geometries theoretically.

Since the geometry optimization was a quite extensive and conscientiously executed part of the thesis, a detailed discussion follows. At the beginning several strategies appeared to be reasonable, but after trial and error option C was found to be the best choice.

Strategy A
The most elegant and at the same time most time consuming idea to optimize the structure of the molecular junctions was to first make an optimization of the geometry of the monolayer attached only on one side to the metal elecrode to get the "natural" tilt of the molecules. This can be done by using the GADGET optimizer and introducing a large vacuum gap of about 20 Å on the unattached side of the molecule, since periodic boundary conditions are applied. Fig. 15a shows a corresponding starting geometry for the N_{in} molecule with a 2×2 unit cell.
As soon as the optimum geometry of the monolayer docked to one electrode is found, the metal-SAM system can be attached to the second electrode by setting the same distance between docking group and second electrode as was found for the first electrode. After that one has to optimize this junction structure, meaning that the total energies for different lengths of the unit cell, need to be determined. In this fashion the global minimum structure including an optimization of the electrode-electrode distance can be obtained.

Since GADGET works with internal coordinates, it is possible for atoms to move large distances to adopt optimum position. This is at the same time a big problem within this strategy, resulting in quite large tilt angles for some of the SAMs. The tilt angle of a molecule attached to a surface is defined as

$$\alpha = \arccos\left(\frac{\mathbf{a}\cdot\mathbf{e_z}}{|\mathbf{a}|\cdot|\mathbf{e_z}|}\right) = \arccos\left(\frac{a_z}{|\mathbf{a}|}\right) \tag{3.1}$$

where $\mathbf{a}$ is the axes along the molecular backbone, defined as the vector connecting the lowest and top atom of the molecule and $\mathbf{e_z}$ is the unit vector in z-direction perpendicular to the surface.

As depicted in Fig. 15b the N_{in} molecule tilts quite significantly with $\alpha = 35\,^\circ$, making the attachment to the second electrode kind of inconvenient. Fig. 16 and 17 show the situations for $Tour_{NC}$ and $Tour_{Pyr}$. While for the former a tilt angle of about $\alpha = 34\,^\circ$

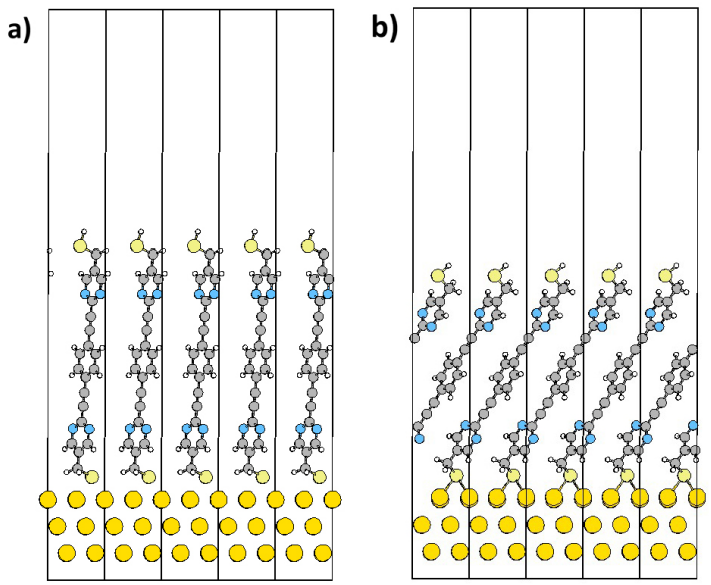

Figure 15: N_{in} molecule attached to one electrode before (a) and after (b) geometry optimization with GADGET following strategy A; tilt angle after optimization: $\alpha = 35$ °

was found, similar to the N_{in} molecule, the latter exhibits a tilt of only $\alpha = 4$ ° i.e. the molecules stand almost upright. Since in this work, chemically different docking groups and their resulting dipole moments shall be investigated, these different tilt angles would lead to an additional effect superposing the effects under investigation. Therefore, to make traceable comparisons between the different systems and, additionally, since the impact of the tilt angle has been discussed in different publications anyway [18], it was decided not to account for different tilts and to move on to strategy B.

Strategy B
Instead of optimizing the individual monolayers a simple perpendicular arrangement of the molecules in between the electrodes was assumed. This is associated with a little complication since the unit cells have the form ABC-molecule-ABC (A, B, C referring to the (1,1,1) Au layers in a closed packed fcc structure). As a consequence, there would be different docking positions for the two ends of the molecules, due to the fact that the molecule bonds to a "C" layer on one side and to an "A" layer on the other side. An idea was to change the layer stacking of the unit cell to ABCA-molecule-ABC, but such an asymmetric unit cell was decided to be not compatible with the Green's function based transport calculations.

Strategy C
As a combination of the two aforementioned options we designed the following strategy for obtaining consistent geometries that would avoid interference with effects stemming from different tilt angles and at the same time overcome the problem of different docking positions obtained for a simple perpendicular arrangement. As a first step the molecules were "pre-optimized" in gas phase using GAUSSIAN09 [89] (applying the PBE functional [67] and the 6-31G* basis set [90]). To overcome the problem concerning the different dock-

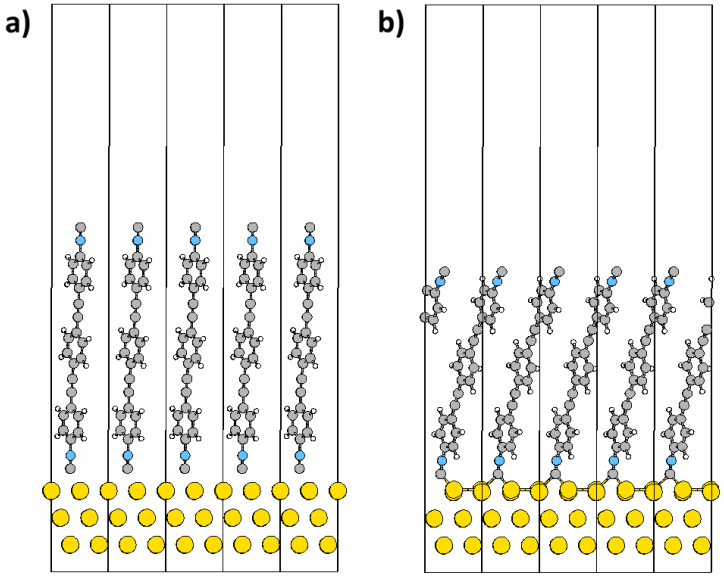

Figure 16: Tour_{NC} molecule attached to one electrode before (a) and after (b) geometry optimization with GADGET following strategy A; tilt angle after optimization: $\alpha = 34$ Å

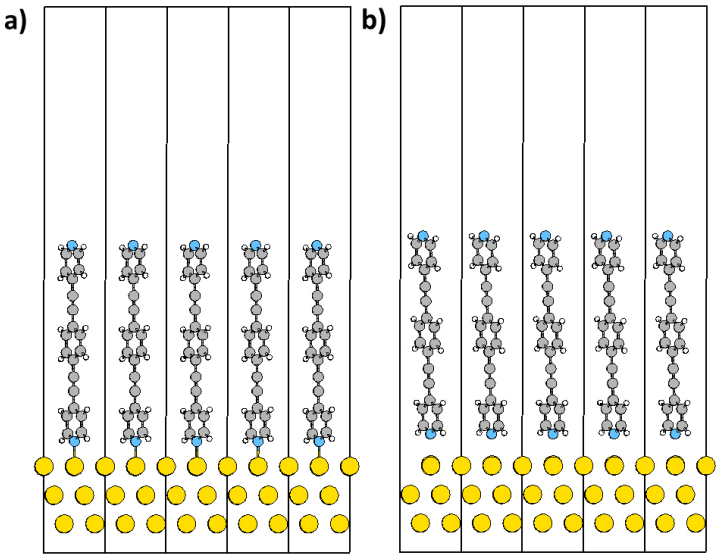

Figure 17: Tour_{Pyr} molecule attached to one electrode before (a) and after (b) geometry optimization with GADGET following strategy A; tilt angle after optimization: $\alpha = 4$ Å

ing positions on each side of the junction discussed above for the fully perpendicular arrangemenet, a slight tilt of the molecules was introduced to achieve two equivalent docking positions. To get consistent results, this had to be done in the same way for all junctions, especially regarding the twist angle of the molecules. This shall be demonstrated on the example of N_{out}. As can be seen in Fig. 18, the twist angle strongly influences the symmetry of the optimized structure. Fig. 18A1 shows the top view of the molecular junction with a twist angle that leads to a close approach of the hydrogene atoms and the molecular backbones are almost arranged in line. Optimizing this structure leads to a completely asymmetric geometry, as shown in Fig. 18A2. Since this asymmetry would strongly impact the dipole moment in z-direction and, therefore, the whole collective effect, a different twist angle is chosen, as can be seen in Fig. 18B1. With this arrangment the optimized geometry becomes symmetric (Fig. 18B2). All molecules where arranged in a structure according to Fig. 18B1.

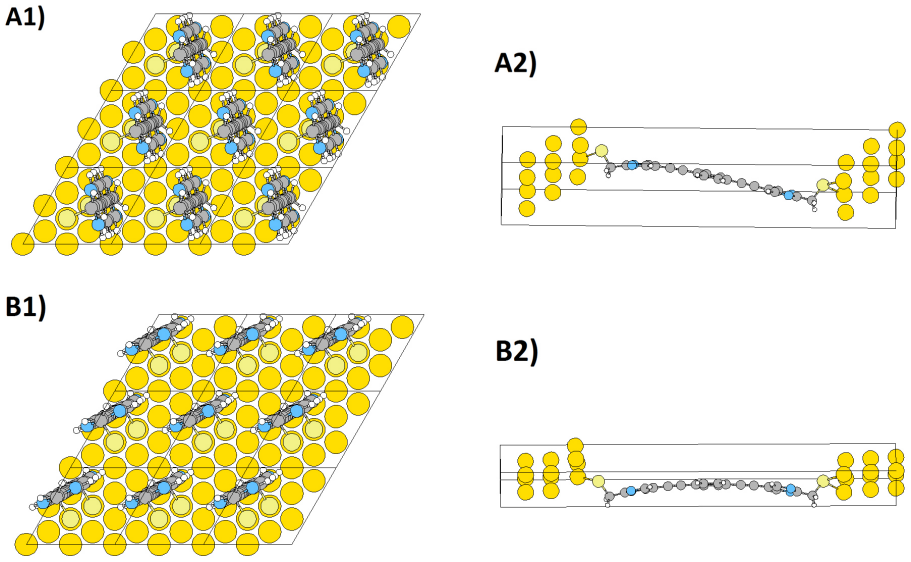

Figure 18: Top view of N_{out} starting geometry with different twist angles A1), A2) resulting in an asymmetric (A2) and symmetric (B2) geometry after optimization according to strategy C.

As a next step, the optimimum distance between the electrodes had to be determined, as described in option A. To that aim, the distance between the docking group and the innermost Au layer was first set to a certain value (starting geometry $z = 0$ in Fig. 19) and then varied in steps of ± 0.1 Å. For every z distance, the geometry was fully optimized. By making the unit cell larger and smaller and calculating the minimum energy for each electrode-electrode distance, a parabolic relationship between distance and energy was found, as illustrated in Fig. 19 for the different systems (black circles referred to as "standard" method). To find the geometry with the lowest energy, a first idea was to apply a parabolic fit to the black circles of Fig. 19 and take the geometry with the electrode-electrode distance belonging to the minimum energy. This fit turned out to be strongly dependent on the number of points taken into account. Additionally, some of the systems exhibit more assymetry in the parabolic behaviour than others. Alltogether, the

position of the minimum turned out to be too sensitive to make consistent statements. Therefore, another strategy was found to get access of the geometry with minimum energy. As a first suggestion, the optimized geometry with the electrode-electrode distance belonging to the lowest energy (minimum of the black circles) was taken to be the minimum. To ensure that one is close to a minimum, the optimized structure of the minimum found so far was used to start new geometry optimizations reducing and enlarging the unit cell in z-direction by ±0.05 Å. If the change in energy was found to be $\Delta E < 0.0002$ eV, the geometry was taken to be the optimum one (as for the Tour_{SH} and Tour_{Pyr} junctions in Fig. 19d and e referred to as "check 1"). For energy differences larger than 0.2 meV the sanity check was repeated (as for the N_{in}, N_{out} and $\text{Tour}_{\text{CH}_2\text{SH}}$ junctions in Fig. 19a, b and c referred to as "check 2").

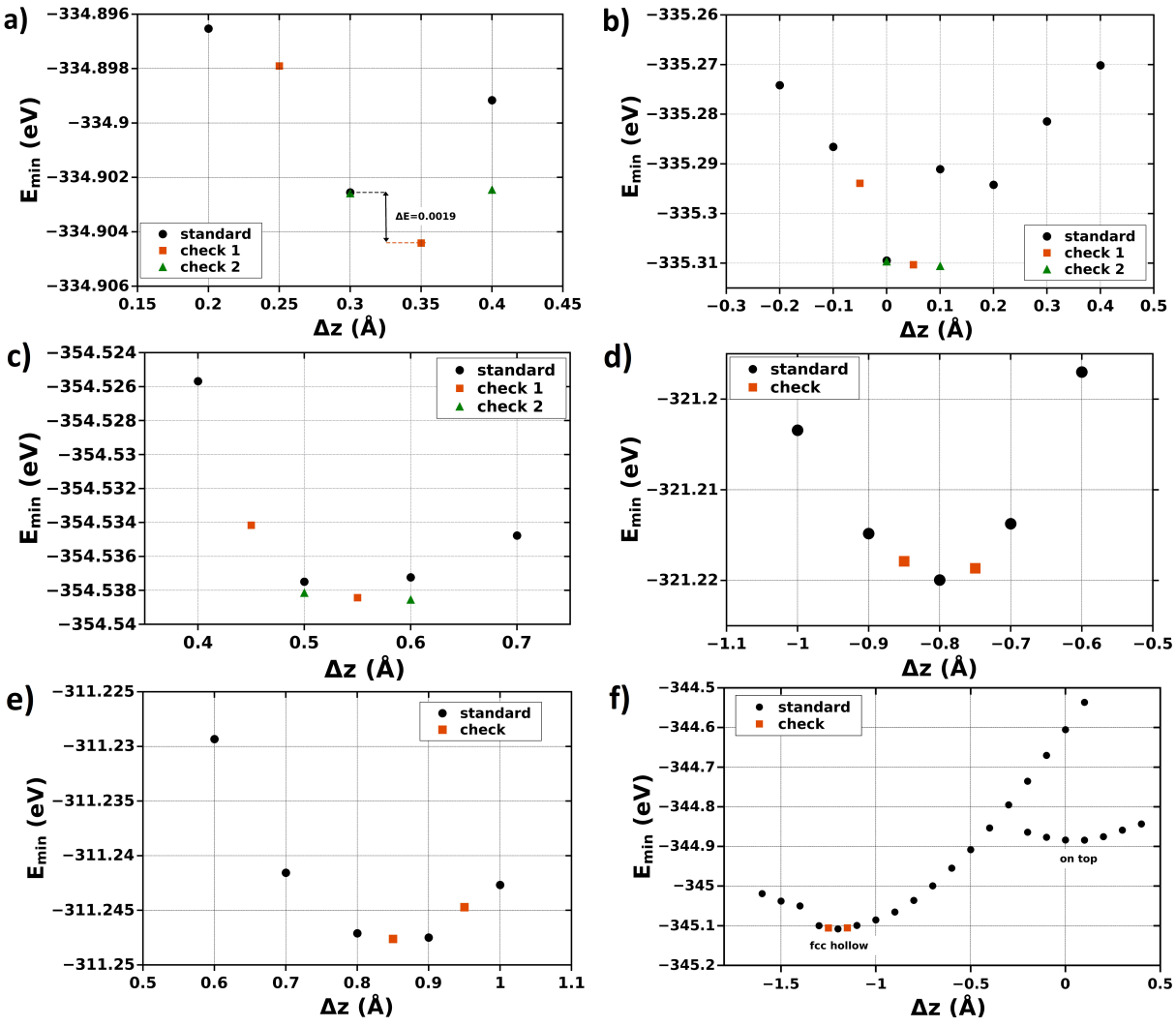

Figure 19: Minimum energies as a function of different electrode-electrode distances for a) N_{in}, b) N_{out}, c) $\text{Tour}_{\text{CH}_2\text{SH}}$, d) Tour_{SH}, e) Tour_{Pyr} and f) Tour_{NC}. Starting with an initial configuration at $z = 0$, the electrode-electrode distance was varied in steps of ±0.1 Å and for every Δz the geometry was optimized, resulting in a parabolic relationship between minimum energy E_{min} and distance.

The optimized geometries corresponding to the minimum energy taken from Fig. 19 are illustrated in Fig. 20a-f for N_{in}, N_{out}, $Tour_{CH_2SH}$, $Tour_{SH}$, $Tour_{NC}$ and $Tour_{Pyr}$ respectively. The organic parts of the long molecular junctions N_{in}, N_{out} and $Tour_{CH_2SH}$ were slightly bent, while the shorter ones $Tour_{SH}$, $Tour_{NC}$ and $Tour_{Pyr}$ remained straight. For the thiol docking group, -S was found to dock on the hollow position (only fcc hollow position was tried), while for the pyridine -N an on top docking position was favoured. For $Tour_{NC}$ two energy minima were found, see Fig. 19d, corresponding to different docking positions. Energetically the fcc hollow docking position turned out to be the favourable docking position.

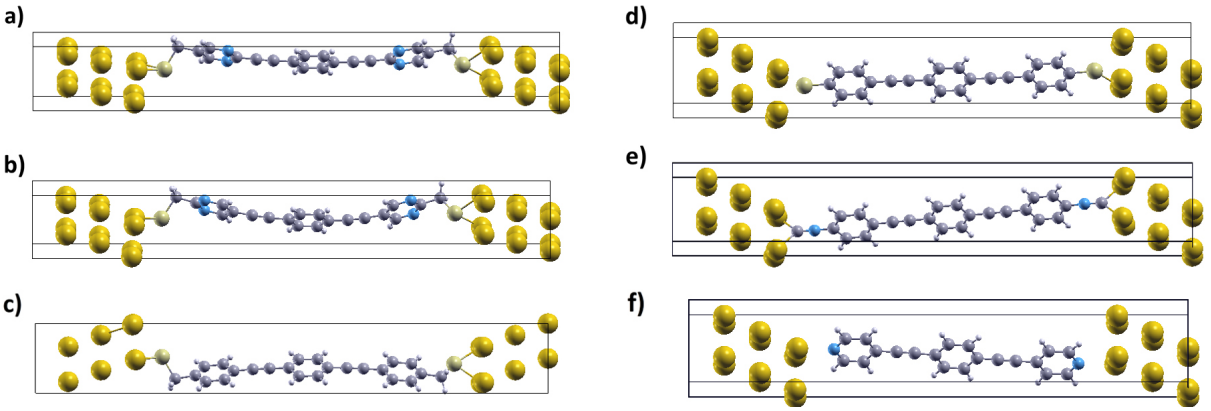

Figure 20: Fully optimized molecular junctions according to strategy C for all investigated systems: (a) N_{in} (b) N_{out} (c) $Tour_{CH_2SH}$ (d) $Tour_{SH}$ (e) $Tour_{NC}$ (f) $Tour_{Pyr}$

3.3 Variation of Coverage

To achieve intermediate situations between single molecule and full monolayer junctions, the density of the molecules bridging the electrodes was varied by changing the size of the unit cell and successively removing molecules. All systems are based on a $p(2 \times 2)$ unit cell, as shown in Fig. 21a. Repeating this unit cell in every spatial direction, results in a full monolayer junction with coverage $\Theta = 1$. Doubling this unit cell in x direction and at the same time deleting one molecule, yields the unit cell depicted in Fig. 21b. One molecule in a doubled sized unit cell repeated in every spatial direction mimics half of the coverage of a full monolayer, $\Theta = 0.5$. (After deleting the redundant molecule in the unit cell, the relaxed gold atoms on these places where manually replaced by unrelaxed ones.) By alternatingly doubling the unit cell in x and y direction and always keeping only one molecule per unit cell, coverages of $\Theta = 0.25$, $\Theta = 0.125$ and finally $\Theta = 0.0625$ were generated, as shown in Fig. 21c, d, e. The lowest coverage achieved here, $\Theta = 0.0625$, is assumed to mimic the single molecule situation.

For all coverages, molecules were kept frozen at the equilibrium geometry found for full coverage to highlight effects of purely electronic nature. Additionally, full geometry optimizations of reduced coverage would be computationally extremely costly.

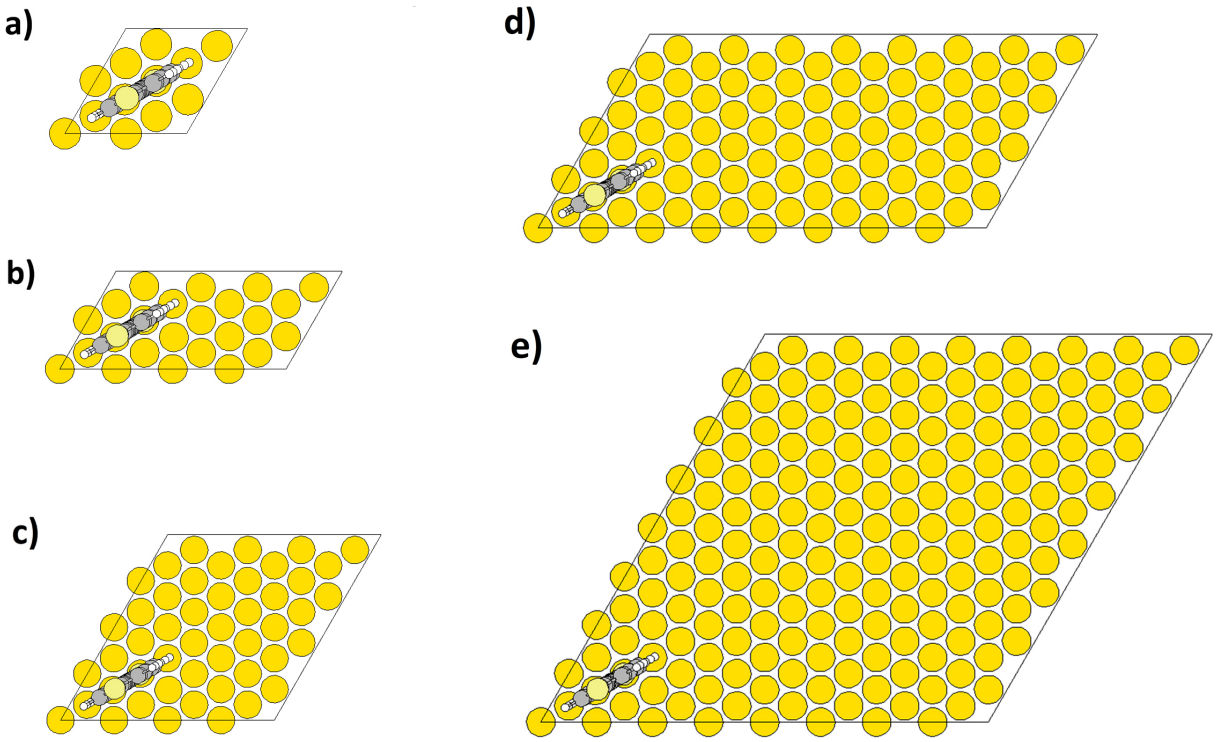

Figure 21: Top view of molecular junctions of different coverage. Variation of coverage by varying the size of the unit cell, in particular by alternately doubling the unit cell in x and y direction. $\Theta = 1$ (a), $\Theta = 0.5$ (b), $\Theta = 0.25$ (c), $\Theta = 0.125$ (d), $\Theta = 0.0625$ (e).

Finally, it should be mentioned that such an approach for varying the coverage of a monolayer has been successfully applied in previous studies, for example in those by Romaner et al. [91] on the basis of metal-SAM systems and by Wang et al. [47] for molecular junctions comprising alkane monolayers of different densities.

3.4 Adaptation of k-Point Mesh

For these differently sized unit cells, the k-point meshes had to be adapted. A typical scheme for k-point generation is the Monkhorst-Pack method, that was introduced in section 2.1.6.

For full coverage, $\Theta = 1$, an 8×8 k-point mesh was considered to be sufficient. (A 10×10 k-point mesh led to an insignificant energy difference of 0.007 eV in the corresponding density of states.) According to the inverse relationship of unit cell vector length and k-points, the k-mesh was systematically decreased when going to lower coverages, meaning larger unit cells: 4×8 for $\Theta = 0.5$, 4×4 for $\Theta = 0.25$, 2×4 for $\Theta = 0.125$ and 2×2 for $\Theta = 0.0625$.

Using the Monkhorst-Pack method implemented in VASP, problems arose for coverages $\Theta = 1$, $\Theta = 0.25$ and $\Theta = 0.0625$, corresponding to unit cells with same lengths of the basis vectors in x and y directions. For these cases too many and non-equidistant k-vectors were taken into account by the Monkhorst-Pack generation, as can be seen in Fig. 22. For $\Theta = 1$, an 8×8 k-point mesh would result in at most 64 k-points without considering any symmetry operations. As can be seen in Fig. 22 (black circles) VASP created 96 k-points within the first Broullin zone, which where at unexpected postitions. When proceeding to $\Theta = 0.5$, the right number of 16 k-points after exploiting symmetry is produced on a suitable mesh. For the next lower coverage, $\Theta = 0.25$, again the problem that VASP generates wrong and too many k-points is encountered, while for $\Theta = 0.125$ again correct points are produced.

To overcome this problem and to provide consistent k-point meshs the possibility of entering all k-points "manually" was used. This can be done by specifying the coordinates in x, y and z-direction and the corresponding weights for each k-point in the `KPOINTS` file. The coordinates are to be specified in reciprocal space in fractions of the unit cell vectors of the 1.Broullin zone. An example for a `KPOINTS` file of a 4×4 mesh (corresponding to a coverage $\Theta = 0.25$) would be:

```
manually
8
reciprocal
 0.125 0.125 0.0000 2
 0.375 0.125 0.0000 2
-0.375 0.125 0.0000 2
-0.125 0.125 0.0000 2
 0.125 0.375 0.0000 2
 0.375 0.375 0.0000 2
-0.375 0.375 0.0000 2
-0.125 0.375 0.0000 2
```

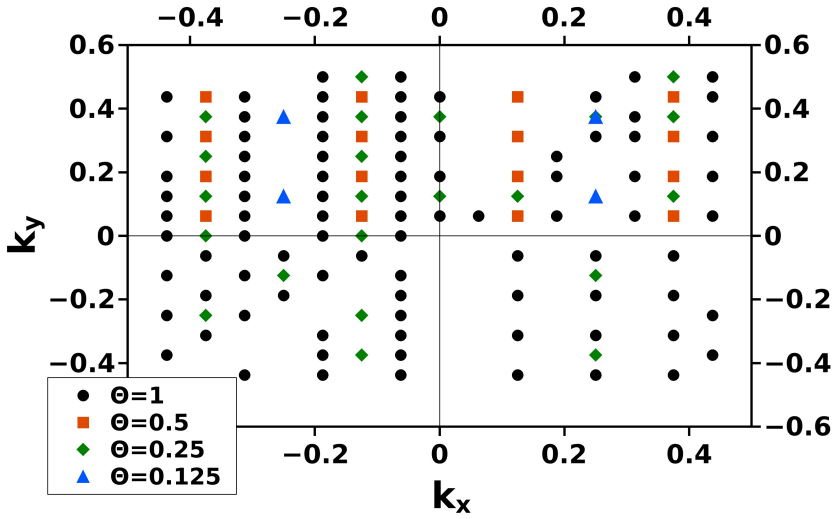

Figure 22: k-point meshes within the 1.Broullin zone for different coverages produced by VASP with the Monkhorst-Pack method. $\Theta = 1$ corresponds to a 8×8 mesh, $\Theta = 0.5$ to a 4×8 mesh, $\Theta = 0.25$ to a 4×4 mesh and $\Theta = 0.125$ corresponds to a 2×4 mesh.

there, the first line is treated as a comment, the second line defines the number of k-points and the third line can be either `reciprocal` or `real`, defining the k-point mesh in reciprocal space or real space, respectively. In the following, the first three columns specify the coordinates and the last row the weight. For a 4×4 grid, there would be 16 k-points, but by using the Kramers-Kronig-relationship ($\Psi(\mathbf{k}) = \Psi(-\mathbf{k})$), one can reduce the number of k-points to 8. In this case only positive k_x values are specified and each k-point has the double weight. Fig. 23 shows the k-meshes of different sizes obtained using manual input. In this way, consistently and correctly defined k-points for differently sized unit cells are obtained.

In comparison to the Monkhorst-Pack method that, implemented in VASP, leads to wrong k-points, the correct, manually produced k-point mesh results in an insignificant energy shift of at most 0.004 eV in the corresponding density of states (with the actual value depending on the investigated system and the coverage). Therefore, the effect of the actual mesh is rather small and it is obviously not that important, which k-point mesh will be used. In general, the VASP manual recommends to apply Γ centred methods to be much more efficient for hexagonal unit cells. This was actually found too late to do corrections for all calculations. But, since Γ-centred grids led to an energy shift of only 0.03 eV compared to the Monkhorst-Pack method, again, the effect coming from the mesh was found to be very small. Therefore, the manually generated `KPOINTS` file was used throughout the whole thesis.

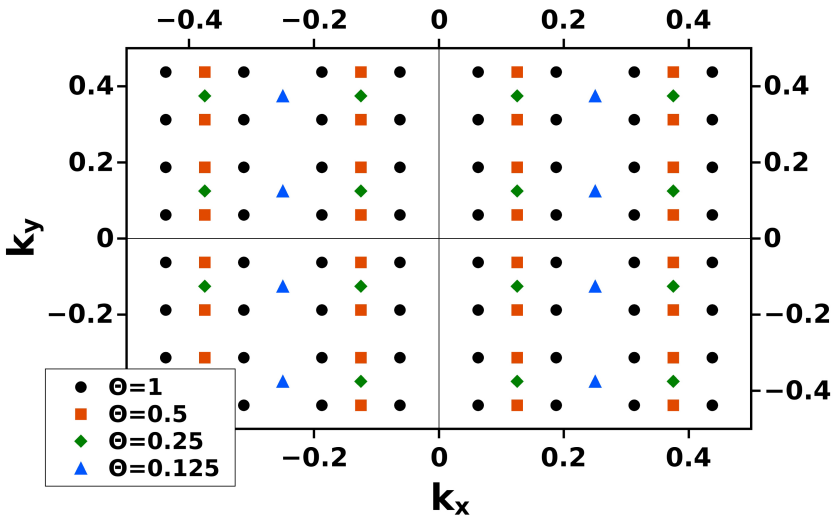

Figure 23: Manually generated k-point meshes within the 1.Broullin zone for different coverages. $\Theta = 1$ corresponds to a 8×8 mesh, $\Theta = 0.5$ to a 4×8 mesh, $\Theta = 0.25$ to a 4×4 mesh and $\Theta = 0.125$ corresponds to a 2×4 mesh.

4 Quantities of Interest

In this chapter the main quantities as well as some basic concepts to understand the later analysis and discussion shall be introduced. The level alignment in the density of states (DOS) will be found to strongly determine the charge transport characteristics. For the examples of N_{out} the typical procedure applied in this thesis to find the right transmissive states will be demonstrated. Additionally, it will be shown that the transport characteristics can be further analyzed on the basis of thermoelectricity and charge transport polarity. Basic definitions of the ionization potential (IP) and the electron affinity (EA) will be given. Additionally, their calculated values for all investigated systems will be listed. An important conceptional idea, on which the analysis of the coverage-dependent effects will be based on, will be introduced in the subsection 4.4.

4.1 Band Alignment

The alignment of the frontier molecular orbitals with the Fermi energy of the metal electrode is expected to be the key parameter governing charge transport characteristics through molecular junctions [40], [77]. In particular, it is the energy separation between the Fermi level E_F and the electronic bands derived from the highest occupied molecular orbital, HOMO, and the lowest unoccupied molecular orbital, LUMO, determining the charge injection barriers, that charge carriers need to overcome to make current flow.

Since upon metal-SAM bond formation, the energy bands in the SAM are broadened and overlap [92], it is often not straightforward to associate the peaks in the PDOS (density of states projected onto the molecular part) around E_F with any particular molecular orbital of the isolated molecule. Additionally, in particular for pyrimidine, problems with overlaping σ and π states arise and therefore the highest and lowest lying peaks in the

DOS are not always the transmissive ones. Therefore, instead of HOMO and LUMO it appears more adequate to refer to the highest energy state in the occupied region of the molecular PDOS as *highest occupied transport channel* HOTC and to the lowest transmissiv energy peak in the unoccupied region as *lowest unoccupied transmission channel* LUTC.

For the examples of N_{out} the typical procedure applied in this thesis to find the right transmissive states shall be demonstrated. To investigate the DOS shown in Fig. 24a for the free-standing N_{out} monolayer at full coverage, a script called `interpolation_and_integration` written by Bernhard Kretz was used to find the energy intervals, in between two electronic states (one spin up and one spin down) are defined. These intervals are indicated by black vertical lines. Additionally, the local density of states LDOS was obtained by integrating the DOS in steps of 0.1 eV in the interesting energy regions. The obtained HOMO-1, HOMO, LUMO and LUMO+1 LDOSs are illustrated in Fig. 24b. As can be seen from the delocalization, the HOMO-2 is the highest occupied transmissive channel and the LUMO is the lowest unoccupied transmissive channel. These results can be compared to the energy intervals of the corresponding DOS in (a) and the HOTC and LUTC can be uniquely identified from these combined findings, as indicated in Fig. 24a.

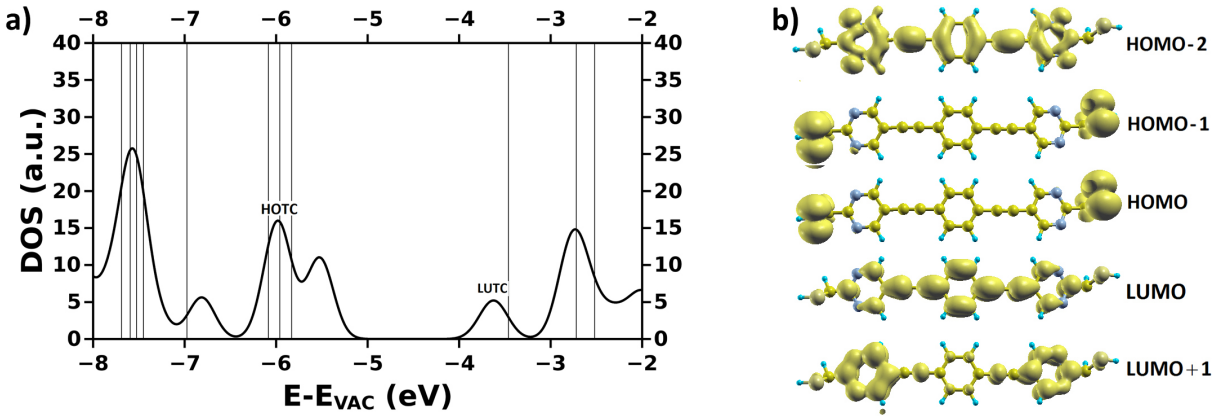

Figure 24: a) DOS for N_{out} molecular monolayer at full coverage. The vertical lines indicate the intervals, in between which two states are found. b) Corresponding isodensity plots of the LDOS.

As illustrated in Fig. 25, the energetic offset of the HOTC and LUTC peaks with the metals E_F, termed as ΔE_{HOTC} and ΔE_{LUTC} constitutes the effective tunnel barrier for holes and electrons respectively. In particular, the molecular level closest to the Fermi level determines the transport characteristics.

Many works concentrated on the dependence of different docking groups on the band alignment e.g. [35] for metal-SAM systems or [47] for molecular devices. In this work, it will be shown that the band alignment in molecular junctions is very sensitive to the selected docking group as well as to the specific coverage.

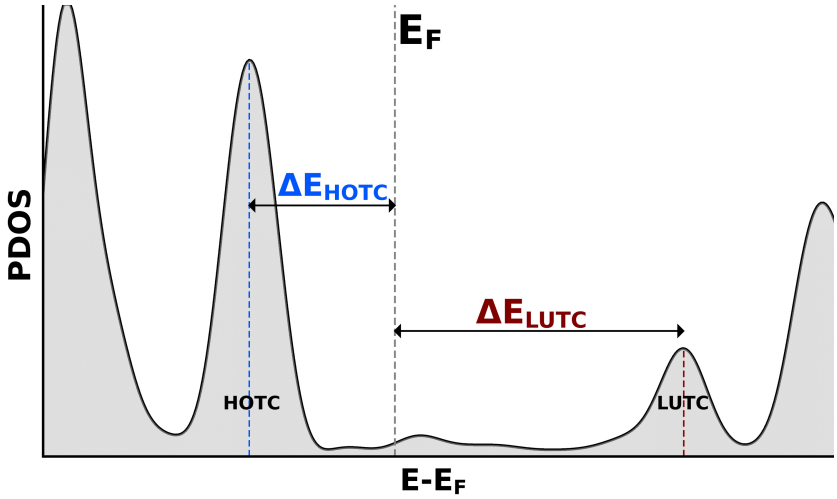

Figure 25: Schematic representation of the charge injection barriers ΔE_{HOTC} and ΔE_{LUTC} as energy offset between the HOTC and LUTC and the Fermi level E_F of the electrodes

4.2 Thermoelectricity and Transport Polarity

The thermopower, also called the Seebeck coefficient S of a material reflects the magnitude of an induced thermoelectric voltage in response to a temperature difference across the material. In 2003 M. Paulsson and S. Datta proposed in a theoretical paper [93], that the sign of the Seebeck coefficient of a molecular junction can indicate the nature of charge transport and the relative position of E_F with respect to the HOMO or LUMO levels. With that, new insights into charge transport in molecular junctions is provided, that cannot be achieved by traditional current-voltage measurements alone. As an alternative, it has been suggested to get the location of the Fermi energy from the asymmetry of the $I(V)$ curves [94], but for that a detailed knowledge of the contact structures would be required. In contrast, the thermoelectric voltage is rather insensitive to the detailed coupling and at the same time large enough to be measured. Additionally, these measurements can not only provide insights about the electronic structure of the molecular junction, but are also expected to have an impact on a yet unexplored field of thermoelectric energy conversion based on molecules [95].

In 2007 P. Reddy et al. reported the first thermoelectric measurements on single molecule junctions [95]. They used STM-BJs (Scanning Tunneling Microscope-based break-junction) to trap molecules between two gold electrodes with a temperature difference across them and statistically measured the thermoelectric voltage. From the histograms for each temperature differential they estimated the junction thermopower, or Seebeck coefficient $S_{junction}$

$$S_{junction} = S_{Au} - \frac{\Delta V}{\Delta T}. \tag{4.1}$$

Here, S_{Au} is the bulk Seebeck coefficient, which is 1.9 μVK^{-1} at 300 K. The relative position of HOMO and LUMO levels with respect to E_F of the electrodes can be related to the measured value of $S_{junction}$. Via the Landauer formula the relationship between the Seebeck coefficient and the slope of the transmission function at the Fermi level can be

obtained as

$$S_{junction} = -\frac{\pi^2 k_B^2 T}{3e} \frac{\partial ln(T(E))}{\partial E}\Big|_{E=E_F}, \tag{4.2}$$

where k_B is the Boltzman constant.

Depending on the position of the Fermi energy with respect to the molecular levels, the thermopower can either be positive or negative. The Seebeck coefficient was found to be positive, when E_F lies closer to the HOMO level, resulting in a so called **p-type** or hole-dominated current, or negative, when E_F is closer to the LUMO, equivalently providing **n-type** or electron-dominated current [95], [96].

In an experimental paper [97] Baheti et al. used thermopower measurements to characterize the dominant transport orbitals of molecular junctions with different chemical structure. While substituents on BDT generated only small changes in the transmission, changing the docking group from thiol to cyanide radically changed the transport dominated by HOMO for the former to LUMO-determined transport for the latter. This was also confirmed by a combined experimental and theoretical work done by Tan et al. [98]. Since the docking group has a strong effect on the level alignment, it of course, also influences thermoelectricity. End group effects on thermopower were also recently studied in a theoretical work [96] by Balachandran et al. They analysed triphenyl molecules coupled to gold for different docking groups and confirmed the possibility of tuning the nature of transport by changing the docking group. Pyridine and amine docking groups in conjunction with conductance and thermopower measurements were done in [99], finding a negative Seebeck coefficient for pyridine-Au linked LUMO - conducting junctions and a positive one for amine-Au linked HOMO- conducting junctions. As pointed out in the introduction, there is also the possibility to switch transport polarity by pure electrostatic effects [38]. In this thesis it will be demonstrated that changes in charge transport polarity can also be achieved by collective effects as well as by different docking groups, as shown in section 6 and 7.

In our theoretical considerations, the nature of charge transport can be obtained by calculating the current through occupied and unoccupied states separately. Therefore, the transmission function is set to zero, $T(E) = 0$ for $E > E_F$ in the case of calculating occupied states and, accordingly, $T(E) = 0$ for $E < E_F$ in the case of calculating unoccupied states. Afterwards, the Landauer Equation 2.28 is re-evaluated again to get the current (as it was done in [38]).

4.3 Ionisation Potential and Electron Affinity

The molecular **I**onisation **P**otential (IP) is defined as the energy that is needed to remove one electron from a molecule in gas phase. It can be expressed as the energy difference between the cation E^+ and the neutral molecule E^0 and is often approximated as the negative HOMO energy, according to Janaks theorem [100].

$$IP = E^+ - E^0 \tag{4.3}$$

For the **E**lectron **A**ffinity (EA) similar considerations can be adopted. Defined as the energy change when an electron is added to the molecule in gaseous state, it can be expressed as the energy difference between the neutral molecule E^0 and the anion E^+, approximately related to the LUMO energy.

$$EA = E^0 - E^- \tag{4.4}$$

Molecular IPs and EAs were calculated using GAUSSIAN09, applying the PBE functional together with the 6-31**G basis set. In contrast to VASP , this code applies open boundary conditions and is, therefore, able to treat the molecule as an isolated moiety. According to Eq. 4.3 and 4.4, the IPs and EAs of all investigated systems were determined by subtracting the total energy of the neutral species from that of the charged radical ion, see table 1.

Table 1: Molecular IP and EA of the investigated molecules obtained from GAUSSIAN09

	$\mathbf{N}_{\mathrm{in}}$	$\mathbf{N}_{\mathrm{out}}$	$\mathbf{Tour}_{\mathrm{CH2SH}}$	$\mathbf{Tour}_{\mathrm{SH}}$	$\mathbf{Tour}_{\mathrm{NC}}$	$\mathbf{Tour}_{\mathrm{Pyr}}$
IP[eV]	6.88	6.84	6.40	6.14	6.81	7.24
EA[eV]	1.52	1.61	1.03	0.88	1.63	1.03

As emphasized in the introduction, $\mathrm{N_{in}}$ and $\mathrm{N_{out}}$ are very similar in gas phase leading to nearly the same molecular IP. In comparison $\mathrm{Tour_{CH_2SH}}$ provides the same docking group but a clearly different molecular IP and EA. Interestingly, $\mathrm{Tour_{NC}}$ has a very similar IP and EA compared to $\mathrm{N_{in}}$ and $\mathrm{N_{out}}$, but a different docking group. For $\mathrm{Tour_{SH}}$ and $\mathrm{Tour_{Pyr}}$ a different docking group as well as different IP s and EA s are calculated.

These trends of the IPs and EAs are mainly reproduced, when evaluating the HOMO and LUMO energies of the investigated single molecules with GAUSSIAN09, as shown in table 2, with exception of the pyridine docking group whose HOMO now fully agrees with the one of $\mathrm{N_{out}}$.

Table 2: HOMO and LUMO energies of the investigated single molecules obtained from GAUSSIAN09

	$\mathbf{N}_{\mathrm{in}}$	$\mathbf{N}_{\mathrm{out}}$	$\mathbf{Tour}_{\mathrm{CH2SH}}$	$\mathbf{Tour}_{\mathrm{SH}}$	$\mathbf{Tour}_{\mathrm{NC}}$	$\mathbf{Tour}_{\mathrm{Pyr}}$
HOMO[eV]	-5.39	-5.43	-4.88	-4.65	-5.27	-5.43
LUMO[eV]	-3.07	-3.14	-2.55	-2.43	-3.10	-2.71

We can now compare these results to IPs and EAs obtained from VASP calculations, where, in contrast to the open boundary conditions provided by GAUSSIAN09, periodic boundary conditions are applied. IPs and EAs are approximated within the VASP calculations as HOMO and LUMO energies of the monolayer at lowest coverage, $\Theta = 0.0625$, with respect to the vacuum level, $\mathrm{E_{VAC}}$. As shown in the corresponding schematic illustration in Fig. 26, $\mathrm{E_{VAC}}$ can be obtained from the plane-averaged potential energy of the free-standing SAM at lowest coverage.

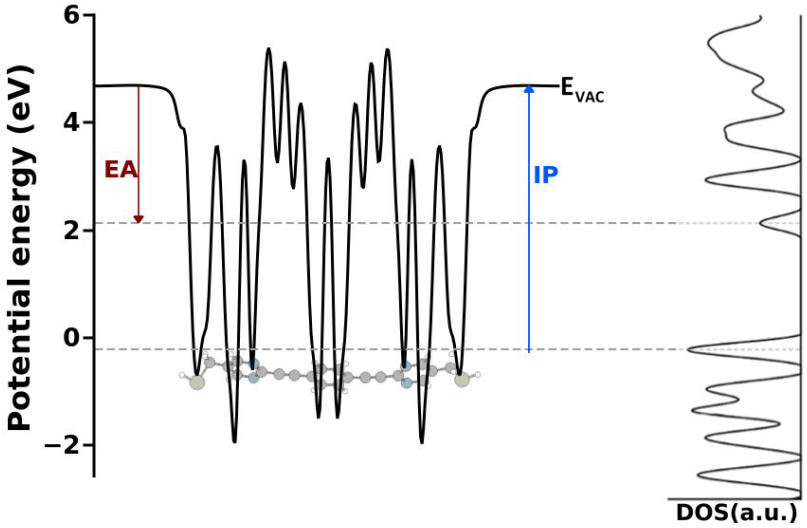

Figure 26: Plane averaged electrostatic potential and DOS of the monolayer with values for the IP/EA, as energy differences between the HOMO/LUMO and E_{VAC} respectively

When comparing the results from table 2 and 3 one can obtain nice agreements in the trends for all molecules. This fact emphasizes the correctness of the single-molecule picture used in this thesis.

Table 3: Molecular IP and EA of the investigated molecules obtained within VASP from the HOMO and LUMO energies for monolayers at lowest coverage $\Theta = 0.0625$ aligned to vacuum level taken from the according plane-averaged potential.

	$\mathbf{N}_{\text{in}}$	$\mathbf{N}_{\text{out}}$	$\mathbf{Tour}_{\text{CH2SH}}$	$\mathbf{Tour}_{\text{SH}}$	$\mathbf{Tour}_{\text{NC}}$	$\mathbf{Tour}_{\text{Pyr}}$
IP[eV]	-5.80	-5.83	-5.17	-4.93	-5.72	-5.86
EA[eV]	-3.48	-3.40	-2.87	-2.76	-3.60	-3.48

4.4 Charge Rearrangements and Bond Dipole

When a SAM is deposited onto a metal surface, the formation of chemical bonds leads to charge density rearrangements [101], [91], [51]. To describe these modifications of the charge density upon bond formation, it is convenient to conceptionally partition the metal-molecule-metal system into metallic and molecular part.

Therefore, charge rearrangements, $\Delta\rho$, can be expressed as the difference between the charge density of the full metal-molecule-metal system ρ_{sys} and the sum of the densities of the isolated non-interacting subsystems, consisting of the charge density of the metal surface ρ_{slab} and the molecular part ρ_{mol} (Eq. 4.5a). In the case of a thiol docking group, the sulfur has to be saturated in the free standing monolayer and the charge density of hydrogen ρ_H needs to be subtracted upon bond formation (Eq. 4.5b). So bonding of SH to gold is a bond replacement rather than a bond formation [81].

$$\Delta\rho = \rho_{sys} - [\rho_{mol} + \rho_{slab}] \tag{4.5a}$$

$$\Delta\rho = \rho_{sys} - [(\rho_{mol} - \rho_H) + \rho_{slab}] \tag{4.5b}$$

These charge rearrangements include contributions from bond formation/replacement as well as contributions stemming from the Pauli pushback [101], [102]. This is the pushback of the exponentially decaying tail of the electron density leaking out of the metal surface into the vacuum, when the monolayer attaches the surface. $\Delta\rho(x, y, z)$ can be integrated in the (x, y) plane over the unit cell reducing the dimensionality to $\Delta\rho(z) = \int\int \Delta\rho(x, y, z)dxdy$, which only depends on the z-direction and is given in units of $[-e/\mathring{A}]$. Fig. 27 shows the charge rearrangements for the reference system $\text{Tour}_{\text{CH}_2\text{SH}}$. It can be seen that they are strongly localized at the immediate interface region between the metal and the molecule. Depending on the chain length and on the docking group this is not always the case, especially for pyridine anchor groups [51], leading to Fermi level pinning [51], as will be shown in section 7.

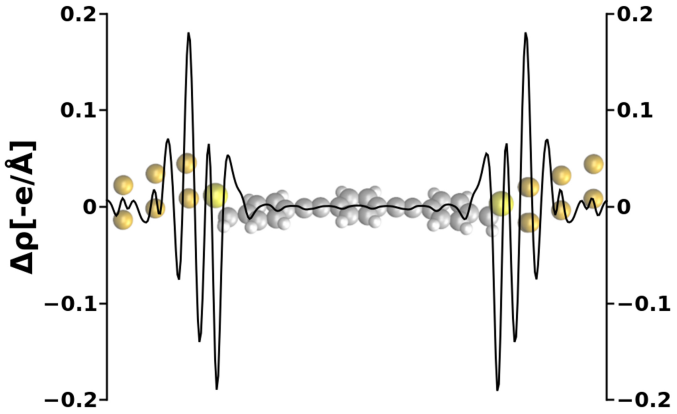

Figure 27: Charge rearrangements $\Delta\rho$ upon bond formation integrated over the (x, y) plane of the surface unit cell for $\text{Tour}_{\text{CH}_2\text{SH}}$ molecular junction of full coverage $\Theta = 1$

Further insight into the implication of charge rearrangements can be obtained by integrating $\Delta\rho$ over the transport direction z, yielding the amount of transferred electrons $(-e)$, reflected in the net charge transfer $Q(z)$, illustrated in Fig. 28.

$$Q = \int_{-\infty}^{z} \Delta\rho(z')dz' \tag{4.6}$$

The alternating sequence of charge accumulation and depletion corresponds to a series of dipoles rapidly decaying both in the metal and in the SAM leading to a single, pronounced step in the electrostatic potential. A relation to the charge rearrangements is given by the one-dimensional Poisson equation

$$\nabla^2 V = -\frac{\Delta\rho}{\epsilon_0} \tag{4.7}$$

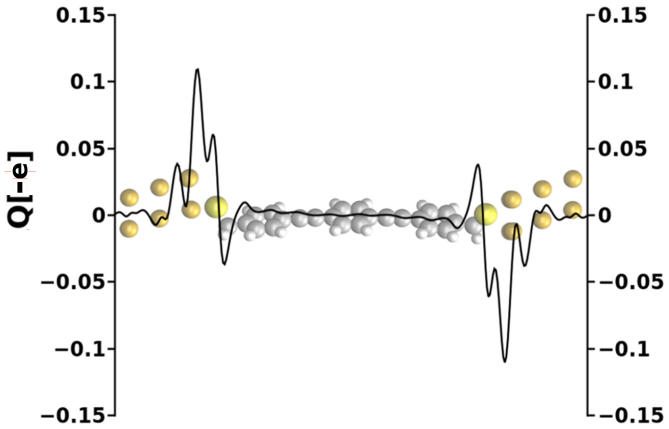

Figure 28: Charge transfer Q integrated over the (x, y) plane of the surface unit cell for $\text{Tour}_{\text{CH}_2\text{SH}}$ molecular junction of full coverage $\Theta = 1$. Since there is one molecule per unit cell, this is the charge transfer per molecule.

Fig. 29 shows the corresponding change in the electrostatic potential energy $\Delta E(z)$, that is again confined to the interface between metal and molecule. The magnitude of the total step in the potential energy is typically referred to as bond dipole $\Delta\text{E}_{\text{BD}}$ [101], [35]. Shape and magnitude of the the bond dipole depend strongly on the nature of the docking group [35], on the metal substrate [35] as well as on the packing density [91], [47], as will be seen in chapters 6.1 and 7.

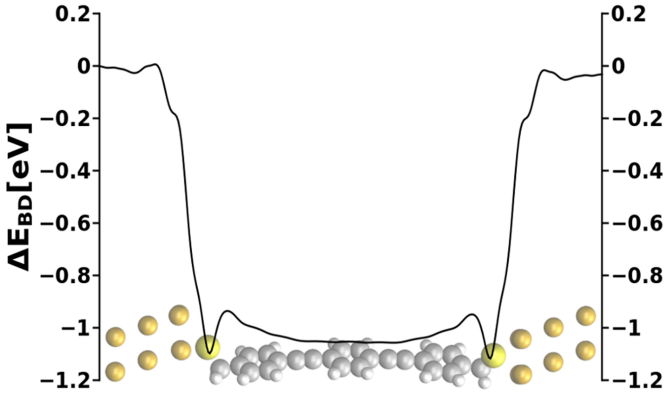

Figure 29: Bond dipole ΔE_{BD} arising from charge rearrangements for $\text{Tour}_{\text{CH}_2\text{SH}}$ molecular junction of full coverage $\Theta = 1$.

The quantities $\Delta\rho(z)$, $\Delta Q(z)$ and $\Delta\text{E}_{\text{BD}}$ can be obtained using some VASP post-processing routines that use the aforementioned equations. These routines have been written by former group members. The `average` script yields the plane averaged *potential.dat* and *charge.dat* for each subsystem and afterwards executing
`induced_density_(un)saturated_monolayers` provides the *bond_ dipole.dat* file containing the plane-averaged quantities.

5 Computational Methods

In this thesis three different programs were used to get the electronic as well the transport properties of the investigated systems: VASP, $\text{SIESTA}_{\text{TS}}$ and TRANSIESTA. While their theoretical fundamentals were already discussed in section 2, this chapter focuses on their practical application. Since VASP was used in its "typical operation scheme" (as e.g. in [35]), only the transport programs shall be addressed here in detail.

To get the transport properties of the investigated systems two programs, both based on SIESTA were used to do combined DFT and Green's function calculations. On the one hand, a generally available expansion of SIESTA called TRANSIESTA [76] was deployed, and, on the other hand, a code called $\text{SIESTA}_{\text{TS}}$, has been used. The latter was developed in a cooperative work of Georg Heimel and David A. Egger. For this, no official description is available. A very detailed description of TRANSIESTA can be found in its users manual [103]. A comparison of the transport characteristics obtained from these two codes is given in section 6.2.2. The reason for changing between these codes were enormous convergence problems with TRANSIESTA, when going to coverages lower than $\Theta = 1$, which so far have not been overcome. Therefore, results obtained from TRANSIESTA and $\text{SIESTA}_{\text{TS}}$ will be compared for full coverage, while low coverages will be calculated with $\text{SIESTA}_{\text{TS}}$. In this thesis, only zero-bias transmission was calculated, not considering a voltage drop to evaluate current at finite voltage. This is justified up to relatively low voltages, where the transmission function was found not to change significantly in the relevant small energy window [104], [105].

5.0.1 General Description - TRANSIESTA

Obtaining the transmission function of a typical molecular junction with TRANSIESTA involves three consecutive calculations: the **bulk** calculation, the **central region** calculation and afterwards the **tbtrans** run, where the transmission function is determined. Using localized basis sets enables the partitioning of the system into left electrode, central region, and right electrode, as shown in Fig. 30.

The **bulk calculation** is a standard SIESTA run with periodic boundary conditions, where an additional file, the `electrode.TSHS` is generated. It contains all information about the electrodes, which is necessary to perform the calculation for the central region and also the tbtrans run. This file comprises the real-space Hamiltonian and the overlap matrices together with some information used to calculate the surface Green's functions. The electrode atoms will not enter explicitly into the TRANSIESTA calculation, but only through the self-energies that they produce.

In general, the organic system can be sandwiched between two different kinds of semi-infinite leads and two appendant electrode calculations can be performed separately. In this thesis left and right gold electrodes have identical structures (see Fig. 30), so the same `electrode.TSHS` file can be used to describe both.

When performing the calculations, a couple of things have to be considered. `SolutionMethod`

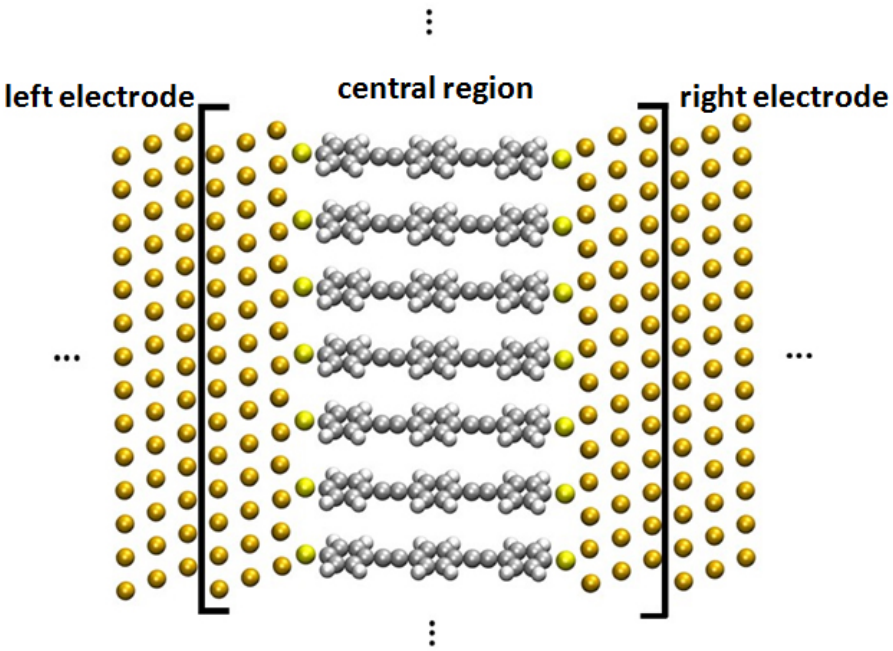

Figure 30: Molecular junction seperated into left electrode, central region, and right electrode for TranSiesta calculations

must be set to `diagon` when performing a Siesta run. `TS.SAVEHS` has to be set to true, to generate and save the `.TSHS` file containing Hamiltonian and overlap matrix. This can be seen in the following part of a `.fdf` input file for a bulk calculation:

```
##########################################################################
# Atomic coordinates and Unit cell specification                         #
##########################################################################
AtomicCoordinatesFormat      Ang    # Bohr (Ang, ScaledCartesian, Fractional)
AtomCoorFormatOut            Ang    # Bohr (Ang, ScaledCartesian, Fractional)
%block AtomicCoordinatesAndAtomicSpecies
4.4284645500    2.5567752000    0.0000000000    1
1.4761548500    2.5567752000    0.0000000000    1
0.0000000000    0.0000000000    0.0000000000    1
2.9523097000    0.0000000000    0.0000000000    1
2.9523097000    3.4090336000    2.4105910000    1
5.9046194000    3.4090336000    2.4105910000    1
1.4761548500    0.8522584000    2.4105910000    1
4.4284645500    0.8522584000    2.4105910000    1
7.3807742500    4.2612920000    4.8211820000    1
5.9046194000    1.7045168000    4.8211820000    1
4.4284645500    4.2612920000    4.8211820000    1
2.9523097000    1.7045168000    4.8211820000    1
%endblock AtomicCoordinatesAndAtomicSpecies
```

Atomic coordinates have to be arranged in ascending order along the z-axis, corresponding to the transport direction. Moreover, the individual atoms have to have the same

order as in the corresponding `centralregion.fdf` file. The left electrode will be defined to be the first atoms in the central region calculation and the right electrode to be the last ones. As can be seen from the atomic coordinates, three layers of Au(111) are sufficient to describe the metallic character of the electrodes in the unit cell on each side.

Attention has to be paid to the length of the bulk unit cell in transport direction. It should be large enough to ensure that orbitals spread only into nearest neighbour cells. Therefore the size of the bulk unit cell is associated to the extent of the orbital basis functions, which is determined by the `PAO.EnergyShift`, discussed in section 6.2.1. Generally, SIESTA works with a so called internal auxiliary supercell ($n_x \times n_y \times n_z$), describing the number of unit cells needed in every spatial direction to include interactions correctly. In summary, to include only nearest neighbour interactions, for the electrode the unit cell along the z-direction needs to fulfill two criteria: (i) the internal auxiliary supercell should be 2 in z-direction ($n(z) = 2$) and (ii) $2R_{max} < L_z$ with R_{max} being the maximum cutoff radius of the basis functions and L_z being the length of the unit cell in z-direction.

Besides, care should be taken to always have the same settings in the input file of the electrode as in the central region calculation. Otherwise, wrong results will be obtained within the tbtrans run.

In TRANSIESTA, k-points have have to be set in the specification part of the `electrode.fdf` file according to the Monkhorst-Pack's scheme:

```
##########################################################################
# K-point grid specifications                                            #
##########################################################################
%block KGridMonkhorstPack
   8   0   0  0.0
   0   8   0  0.0
   0   0   6  0.0
%endblock KGridMonkhorstPack
```

They have to be adapted for different coverages corresponding to the inverse relationship between the appropriate number of k-points and the unit cell length. This k-point sampling, more precisely the first and the second column, have to be the same as the one used for the central region. Otherwise, the code will stop.
To start the bulk calculation, one needs the electrode's pseudo-potential file, `Au.psf` and the `electrode.fdf` file.

As soon as the `electrode.TSHS` file is available, the TRANSIESTA calculation for the **central region** can be executed. Starting with a usual SIESTA Kohn-Sham scheme for periodic systems, the converged density matrix is obtained, serving as an initial input for the Green's functions self consistent cycle shown in Fig. 12. The Hamiltonian and overlap matrix is again stored in the corresponding `.TSHS` file.
All atomic coordinates again have to be ordered along the transport direction. `SolutionMethod` hast to be set to TRANSIESTA.

```
##########################################################################
# TRANSIESTA control                                                     #
```

```
#############################################################################
SolutionMethod               transiesta
TS.SaveHS                    .true.
TS.Voltage                   0.00 eV
TS.MixH                      .false.             # .false. (.true.)
TS.UpdateDMCROnly            .true.              # .true. (.false.)
TS.CalcGF                    .false.             # .true. (.false.)
TS.TriDiag                   .false.             # .false. (.true.)
```

The path to where the bulk calculations are stored has to be specified in the `central_region.fdf` file by setting `TS.HSFileLeft` and `TS.HSFileRight`:

```
#############################################################################
# electrode options                                                         #
#############################################################################
# LEFT ELECTRODE
TS.HSFileLeft  ./electrode.TSHS
TS.NumUsedAtomsLeft   12
TS.BufferAtomsLeft    0
# RIGHT ELECTRODE
TS.HSFileRight  ./electrode.TSHS
TS.NumUsedAtomsRight  12
TS.BufferAtomsRight   0
```

`TS.NumUsedAtomsLeft/Right` are integers defining the number of electrode atoms included in the left/right lead and must be equal to or less than the number of atoms in the unit cell of the electrode. With `TS.BufferAtomsLeft/Right` one can define a number of atoms, starting from the first/last atom of the unit cell, that should be neglected in the TranSiesta run.

To obtain the transport properties in a post-processing way after the TranSiesta run, the analysis utility **tbtrans**, developed by M. Brandbyge was used. It requires the `electrode.TSHS` file and the aforementioned `central_region.fdf` file with additional tbtrans options setup:

```
#############################################################################
# TBTRANS options                                                           #
#############################################################################
TS.TBT.HSFile ./central_region.TSHS
TS.TBT.Emin       -3.0 eV
TS.TBT.Emax       +3.0 eV
TS.TBT.NPoints    600
TS.TBT.NEigen     0
TS.TBT.Eta        0.000001 Ry
```

Here `TS.TBT.HSFile` determines the path to the corresponding `.TSHS` file of the central region. `TS.TBT.Emin/Emax` define the energy range for the computed transmission function, calculated at `TS.TBT.NPoints` points. Since the applied voltage is not stored in the

`.TSHS` files one also needs to define the voltage here.

As an output one gets the `AVTRANS` file containing the k-averaged transmission. For obtaining that for a given spin and energy value the contribution from each k-point is summed with its respective weight. For spin unrestricted calculations the obtained transmission function has to be divided by two. `AVTRANS` consists of 4 columns, the first one giving the energy relative to E_F, the second one showing the averaged transmission function, the third column containing the total density of states, and the last column comprising the density of states projected onto the molecular part PDOS. To specify the atom range on which the PDOS shall be calculated, the parameters `TS.TBT.PDOSFrom` and `TS.TBT.PDOSTo` can be specified in the `tbtrans` run, although this is not defined in the user's manual [71].
To summerize this paragraph an overview about the steps necessary to obtain the transmission function from **TranSiesta** is given below:

a) Calculation of the electrode

- `runtransiesta` with solution method *diagon*
- Input: `electrode.fdf`, `Au.psf`
- Output: `electrode.TSHS` file with Hamiltonian and Overlap matrix

b) Calculation of the central region

- `runtransiesta` with solution method `transiesta`
- Input: `central_region.fdf`, `S.psf`, `C.psf`, `N.psf`,..., `electrode.TSHS`
- Output: `central_region.TSHS` file with Hamiltonian and overlap matrix; `central_region.TSDE` file with density and energy density matrix

c) Tbtrans post-processing

- `runtbtrans`
- Input: `central_region.fdf`, `electrode.TSHS`, `central_region.TSHS`, `S.psf`, `C.psf`, `N.psf`,...
- Output: `.AVTRANS` file containing the transmission function averaged over all k-points

Once the transmission is computed the current can be calculated, according to the Landauer formula (see equation 2.28).

5.0.2 General Description - SIESTA$_{TS}$

As was previously described in section 2.3, the Greens function

$$\mathbf{G}_C^R = (E^+\mathbf{S}_C - \mathbf{H}_C - \mathbf{\Sigma}_L - \mathbf{\Sigma}_R)^{-1} \tag{2.32}$$

according to Eq. 2.32 has to be found to get the transmission function

$$T = \mathrm{Tr}(\mathbf{G}_C^{\dagger}\mathbf{\Gamma}_R\mathbf{G}_C\mathbf{\Gamma}_L) \tag{2.41}$$

and afterwards the current via the Landauer formula (Eq. 2.28). Therefore, the self energies $\mathbf{\Sigma}_{L/R}$ and the Hamiltonian matrix $\mathbf{H}_C$ and overlap matrix $\mathbf{S}_C$ of the central region need to be determined. Using SIESTA$_{\mathrm{TS}}$ three different calculations have to be done, similar as in the aforementioned description of TRANSIESTA provided in section 5.0.1.

Electrode calculation
The electrode calculation, as well as the one for the central region, are separated into two parts: a 'single-point' calculation and a second one, that is called here 'write-out' calculation. To determine the Hamiltonian and overlap matrix for the electrode, a SIESTA$_{\mathrm{TS}}$ calculation has to be performed, by using a modified `pdosK.F` file, that forces SIESTA to write out **H** and **S**. To enable this, one has to adjust the `nhist` parameter in the following part of the corresponding standard SIESTA `.fdf` Input file:

```
%block ProjectedDensityOfStates
 -10.0  5.0  0.2  1502  eV
%endblock ProjectedDensityOfStates
```

Usually, in a standard SIESTA run, this part of the input instructs to write the projected density of states PDOS between two given energies (first two values) with a peak width for broadening the eigenvalues (third value). The last number before eV is called `nhist` and usually determines the number of points in the energy window. In this modified SIESTA$_{\mathrm{TS}}$ version it enables to write out the Hamiltonian and overlap matrices to respective files for each k-point, by setting `nhist`=**1502**, in the case of an electrode. To perform this calculation, one additionally needs to create the so called `params.inp` file with the following structure:

```
SuperCellX 5
SuperCellY 5
SupercellZ 1
```

where the Internal auxiliary supercell has to be defined, that was already introduced in section 5.0.1 and has to satisfy the same conditions. Since this 'write-out' calculation at the moment only works on 1CPU, one has to perform a single point calculation first, to get the converged density matrix `electrode.DM` and the required information about the Internal auxiliary supercell. The Hamiltonian and overlap will be saved in the files `BulkElectrode.spinY.XXX` for each k-point XXX with given spin polarization Y.

Central region calculation
Similar to the electrode calculation, one performs again a single-point and a write-out calculation for the corresponding central region, with the single exception of setting `nhist`=**1503** to write out Hamiltonian and overlap matrices for the central region.

```
%block ProjectedDensityOfStates
 -10.0  5.0  0.2  1503  eV
%endblock ProjectedDensityOfStates
```

As an output one gets the `CentralRegion.spinY.XXX` files for each k-point, that contain the Hamiltonian and overlap matrices for each k-point, and additionally the so called

`Checkwings.dat` file, containing the first row of the central region Hamiltonian matrix, which will be needed for the calculation of the transmission.

Transmission
To get the transmission function there is a script `transmission.f90`, that calculates the zero-bias transmission spectrum at a given k-point in a symmetric two-probe junction via the Landauer-Büttiker formalism. It does not account for real bias, being rather an equilibrium Green's function code, than a NEGF program. The central region is assumed to be already in equilibrium with the electrodes, so no charge can flow in or out of the central region. This is implemented by setting the Fermi levels of the electrodes to the same value as for the central region. Additionally no actual voltage drop is considered in the calculation of the transmission spectrum. This is satisfied by the obseation, that for many organic molecules the transmission around E_F is not significantly affected at reasonable small voltages [105], [106].

For every k-point, spin polarization and energy, the left and right Green's functions $\mathbf{g_{L/R}}$ are iteratively calculated, according to the algorith introcuced in [80]. From that the self-energies $\mathbf{\Sigma}_{L/R}$ (Eq. 2.35) are computed, reflecting the perturbation part to the Hamiltonian of the surface layer that represents the coupling to the bulk. Knowing the self-energies, the Green's function of the central region can be computed according to Eq. 2.34 and from that together with the broadening matrices $\mathbf{\Gamma}_{L/R}$, defined as the anti-hermitian part of the self-energies, the transmission function $T = \mathrm{Tr}(\mathbf{G}_C^\dagger \mathbf{\Gamma}_R \mathbf{G}_C \mathbf{\Gamma}_L)$ can be obtained.

Since this is done for every k-point, a summation of all contributions corresponding to an integration over the 1.BZ can be done,

$$T(E) = \sum_k T_k(E). \tag{5.1}$$

`transmission.f90` needs the `CentralRegion.spinY.XXX`, containing the Hamiltonian and overlap matrices of the central region, the dimension of these matrices and the weight of the current k-point, the `BulkElectrode.spinY.XXX` containing the intra-and interlayer Hamilton and overlap matrices of the electrodes as well as the dimension of these matrices for each k-point, and additionally some general information defined in `tranmission.inp.spinY.XXX` for each k-point. These input files can be generated by executing the script `make_input`, which has the following form:

```
#!/bin/bash

for (( i=1; $i <= 37; i++ ))
do
echo "SpinKpoint          1 $i">transmission.inp.spin1.00$i
echo "MinMaxStepEne       -3.0 3.0 0.01
ElectrodeFermi      -4.1146
CentralRegionFermi  -5.2795
ClipWings           280
```

```
EpsilonIteration    1.e-10
DeltaImaginary      1.0e-5
StartStopDos_01     1   60
StartStopDos_02     61 120
StartStopDos_03     121 180
StartStopDos_04     181 578">>transmission.inp.spin1.00$i

done
```

In this file seven lines have to be defined: The first line, denoted with 'SpinKpoint' defines the spin polarization Y (1 or 2) and the k-point number to be calculated. The second line determines the range in energy for calculating the transmission and the discrete steps in units of eV relative to E_F. The next two lines are the Fermi energies f the respective central region and electrode SIESTA calculation. A very important value is set in the subsequent line, denoted with ClipWings. This is the dimension of the wings that need to be clipped for the Hamilton and overlap matrices of the central region, since the central region is supposed not to interact with its consecutive images, as we rather want it to connect to the electrodes. To get the right value, one needs to check the `CheckWings.dat` file obtained in the central region calculation. This file contains the first rows of the Hamiltonian (real and imaginary part) of the last k-point, where somewhere in the middle of the file all values become zero and then again nonzero. Fig. 31 shows the Hamilton matrix for the unclipped situation (a) and after cutting away the contributions coming from consecutive images (b). In this case about 800 lines have to be cut off (starting from the right), which is the number that needs to be specified in the line referred to as ClipWings.

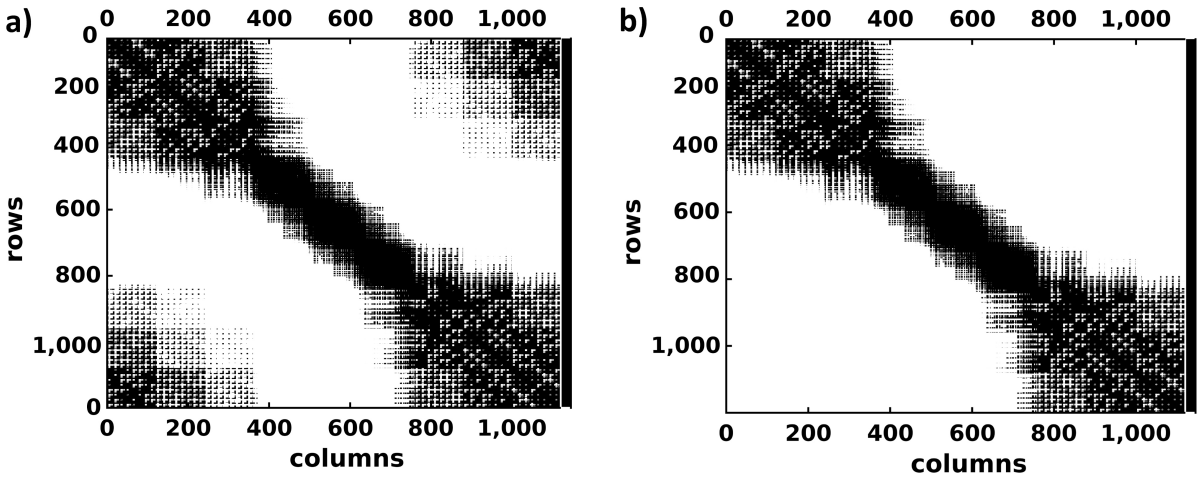

Figure 31: Hamilton matrix of the central region before clipping the wings (a) and after clipping the wings (b). To avoid undesired interactions of the central region with its consecutive images, a certain number of lines have to be cut off in the Hamilton matrix of the central region. This number can be found, by checking the `CheckWings.dat` file. Figures were produced by David. A. Egger.

`EpsilonIteration` is the convergence criterion for the self-energy iteration and `DeltaImaginary`

the imaginary infinitestimal η needed for the retarded Green's function of the device (see Eq.2.32). The last four lines are optional and can be specified to calculate the density of states projected onto an arbitrarily chosen range of atomic orbitals. In this case SartStopDOS_01 would calculate the bulk dos, whereas SartStopDOS_02, 03, 04 would result in the PDOS of the organic elements respectively.

`transmission.f90` creates the output file `transmission.spinY.XXX` for each k-point, containing the energy relative to the Fermi level (in eV), the transmission function, and the projected density of states (both multiplied by the weight of the respective k-point.

To summarize this paragraph an overview about the steps necessary to obtain the transmission function from **SIESTA**$_{\mathrm{TS}}$ is given below:

a) Calculation of the electrode

- **single-point** calculation
  - `runsiesta_TS` with `nhist` = 1501
  - Input: `electrode.fdf`, `Au.psf`
  - Output: `electrode.DM` and auxiliary supercell to define `params.inp`
- **write-out** calculation
  - `runsiesta_TS` with `nhist` = 1502
  - Input: `electrode.fdf`, `Au.psf`, `params.inp` and `electrode.DM`
  - Output: `BulkElectrode.spinY.XXX` files with Hamiltonian and Overlap matrix for each k-point

b) Calculation of the central region

- **single-point** calculation
  - `runsiesta_TS` with `nhist` = 1501
  - Input: `central_region.fdf`, `S.psf`, `C.psf`, `N.psf`, ...
  - Output: `central_region.DM` and auxiliary supercell to define `params.inp`
- **write-out** calculation
  - `runsiesta_TS` with `nhist` = 1503
  - Input: `central_region.fdf`, `S.psf`, `C.psf`, `N.psf`,..., `params.inp` and `central_region.DM`
  - Output: `CentralRegion.spinY.XXX` files with Hamiltonian and Overlap matrix for each k-point

c) Transmission

- `transmission.f90` for each k-point
- Input: `CentralRegionspinY.XXX`, `BulkElectrodespinY.XXX`, `transmission.inp.spinY.XXX`

- Output: `transmission.spinY.XXX` for each k-point containing the transmission function

k-Points in SIESTA$_{\mathrm{TS}}$
To calculate the transmission function for each k-point, one of course has to ensure to have the same k-points for the central-region, as for the electrode. To achieve this, the k-points of the central region have to match the k-points with zero z-component $k_z = 0$ of the electrode. For an 8×8 grid the Monkhorst-Pack scheme generates 37 k-points for the central region, as well as 37 $k_z = 0$ points for the corresponding electrode. For lower coverages, in particular for 4×4 and 2×4 grids, the numbers do not match, resulting in too many $k_z = 0$ points for the electrode.

Since there is no possibility in SIESTA to enter k-points explicitly and attempts to control the k-point mesh by the single parameter `kgrid_cutoff` did not result in any $k_z = 0$ points for the electrode, the ability of writing out the Hamiltonian and overlap matrices for special k-points, as it was used for surface band structure calculations in the master thesis of David. A. Egger, was supposed to solve the problem.

For calculating the surface band structure, one needs to force SIESTA to write out **H** and **S** at arbitrary k-points. To obtain the high accuracy that is provided when using a uniformly distributed k-point mesh, a standard SIESTA DFT calculation is performed for the primary mesh, to receive the converged density matrix. In a second calculation this density matrix is read in by setting `USESaveDM` to `.true.`, and the maximum SCF iterations is set to one (`MAXSCFIterations`=1), meaning SIESTA reads the density matrix and does nothing. To force SIESTA to write out Hamiltonian and overlap matrices at certain k-points, one needs to specify the desired k-points in the `kpoints.inp` file, where the first line defines the number of k-points followed by three columns of k_x, k_y and k_z coordinates. To enable the mechanism, again the `nhist` parameter has to be modified. When `nhist=1506` and the `kpoints.inp` file is available, SIESTA writes out Hamiltonian and overlap matrices at those k-points.

For the case of the 4×4 and 2×4 grids the k-points that were correctly produced for the central region were defined in the `kpoints.inp` file to specify the k-points for the electrode. With this strategy agreement between electrode's and central region's k-points could be achieved for all coverages in a consistent way with no loss in accuracy.

6 Impact of coverage for molecules with intra-molecular dipoles

In this chapter we want to investigate the impact of coverage for molecular junctions consisting of the already introduced N_{in} and N_{out} molecules with polar bonds built into their molecular backbones, see Fig. 32. A detailed analysis of the origins of these coverage effects on the basis of VASP calculations will be followed by transport calculations obtained from SIESTA$_{TS}$, including a comparison to TRANSIESTA results.

After optimizing the geometries of the metal-molecule-metal systems (see section 3.2), the obtained geometry can be used to do electronic structure calculations with the VASP code. Using the script `obtaining_dos` by Gerold M. Rangger one can easily get the density of states DOS as an output, describing the number of states per energy that can be occupied by electrons. Coverage effects will be analysed on the basis of the DOS because the alignment of the molecular energy levels relative to the Fermi energy of the metallic electrodes to a large extent determines charge transport characteristics, as was discussed in section 4.1.

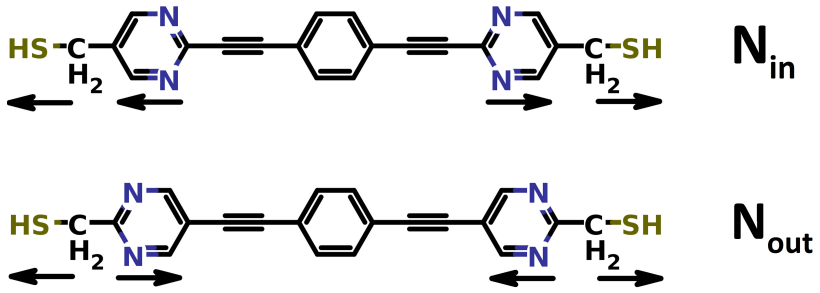

Figure 32: Chemical structure of N_{in} and N_{out}

The N_{in} and N_{out} molecules are put between two gold electrodes and assembled with different densities. Fig. 33a shows their density of states projected onto the molecular part (PDOS) for full coverage $\Theta = 1$. One can clearly identify the HOTC and LUTC peaks and in between the Kohn-Sham gap. There is a pronounced energy difference of 0.8 eV for the HOTC and 0.86 eV for the LUTC between the N_{in} and N_{out} systems. Fig. 33b, c, d and e show the corresponding PDOS for lower coverages, $\Theta = 0.5$, $\Theta = 0.25$, $\Theta = 0.125$ and $\Theta = 0.0625$, respectively. When going to lower densities, the DOS of the systems become increasingly similar. At the single molecule junction level ($\Theta = 0.0625$) there is only a difference of about 0.24 eV for the HOTC and 0.21 eV for the LUTC. Going to even lower densities, $\Theta = 0.03125$ results in no further increase of the shifts in the DOS of N_{in} and N_{out}. The energy difference of about 0.2 eV at the "single molecule level" comes on the one hand from the slightly different IPs of the molecules in gas phase and the rest stems from differences of the local bonding at the contact region. The latter is reflected in the bond dipole that was introduced in section 4.4

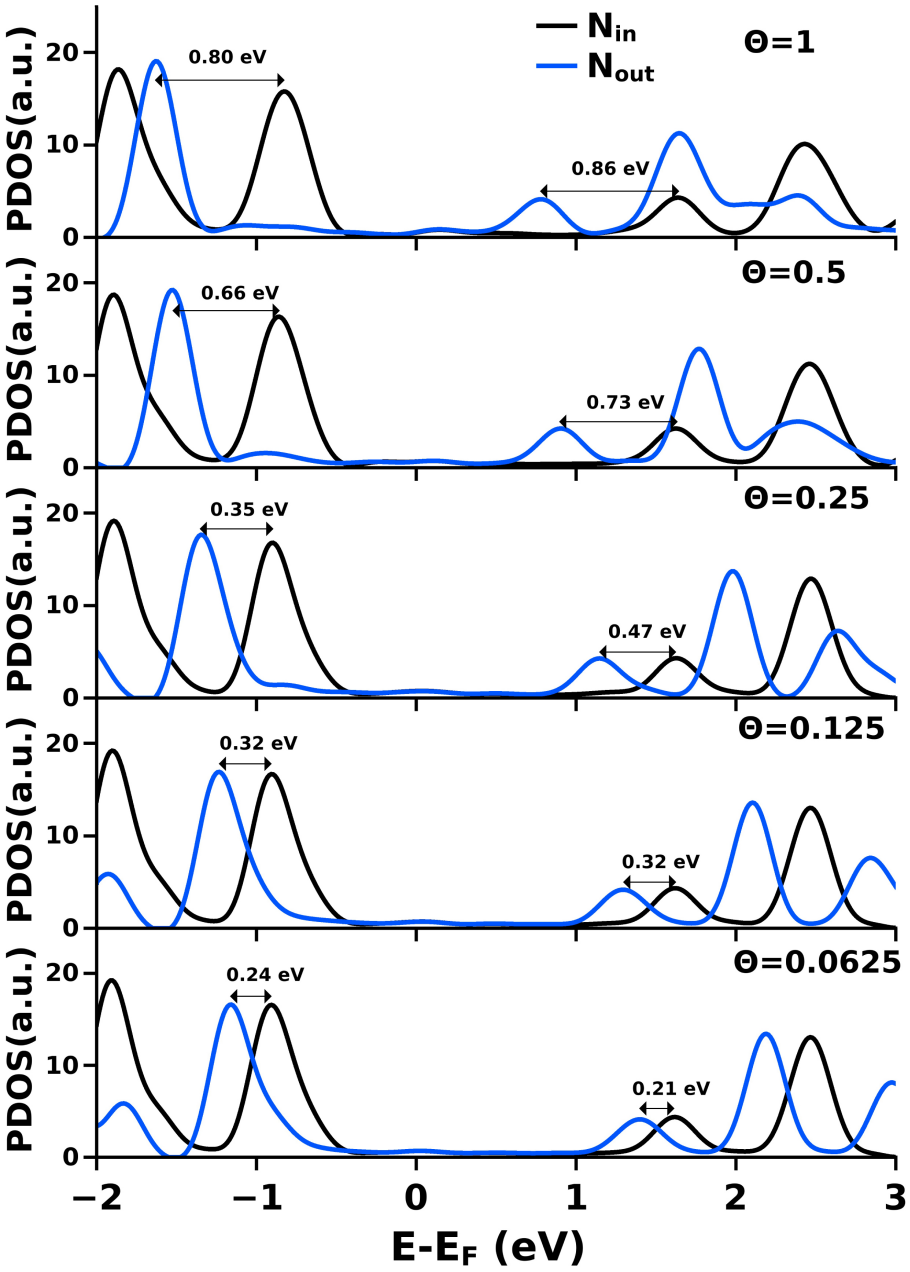

Figure 33: Density of states projected onto the molecular part PDOS for N_{in} and N_{out} junctions of different coverages $\Theta = 1$ (a), $\Theta = 0.5$ (b), $\Theta = 25$ (c), $\Theta = 0.125$ (d), $\Theta = 0.0625$ (e). While the two isomeric molecules have a very similar behaviour in the single molecule junction at lowest coverage, they get more and more different when going to higher coverages.

The shifts in the PDOS of N_{in} and N_{out} junctions shown in Fig. 33 shall be illustrated seperately for each system to investigate the trends in more detail. Fig. 34 shows the PDOS of the N_{out} junction for different coverages Θ, aligned to the Fermi energy E_F. Starting from the densely packed full monolayer, $\Theta = 1$ an energy shift of about 0.5 eV to higher energies is found when going to the single molecule junction $\Theta = 0.0625$. Varying the molecular density for N_{out} junctions has a great effect on the positions of the frontier molecular orbitals, while the Kohn-Sham gap essentially stays the same for different coverages. Screening effects that in real bulk systems reduce the fundamental gap are not captured by (semi)local DFT.

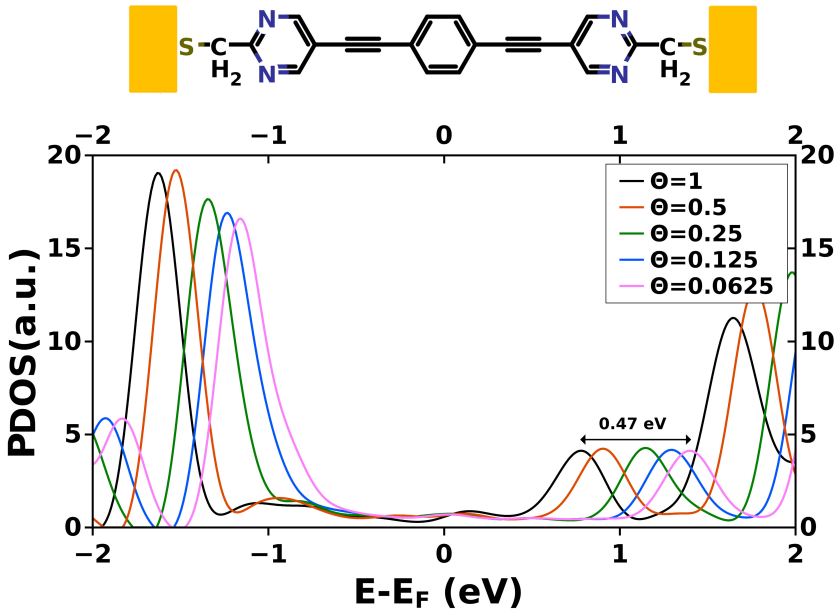

Figure 34: Density of states projected onto the molecular part PDOS for N_{out} junctions of different coverages Θ. PDOS shifts about 0.5 eV when going from full monolayer $\Theta = 1$ to single molecule junction $\Theta = 0.0625$

Equivalent coverage dependent calculations for the N_{in} junction are shown in Fig. 35. Surprisingly, in this case the PDOS does not essentially shift with coverage. The HOTC energy differs about 0.1 eV between full monolayer and single molecule. So for this molecular junction there seems to be no coverage effect.

When assembling these two isomeric molecules in between gold electrodes and varying the coverage, two fundamentally different trends arise. While there is a coverage effect shifting the PDOS for the N_{out} molecular junction, there is no modification in the band alignment for the N_{in} junction. Remembering that N_{in} and N_{out} have the same electrical properties in gas phase, this is a quite surprising result. In the next section, the origin of this behaviour will be associated with two collective effects, analyzed on the basis of the knowledge that was introduced in chapter 4.4.

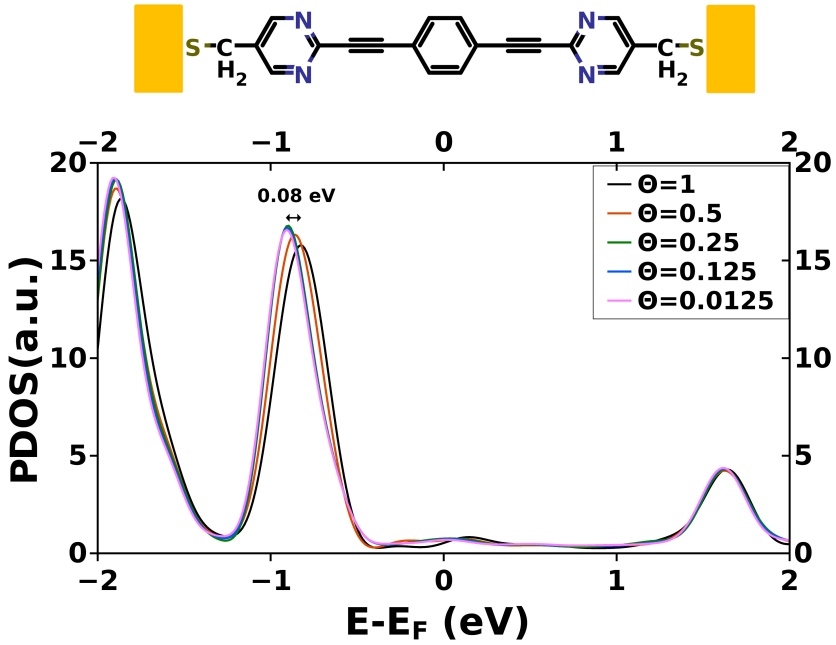

Figure 35: Density of stated projected onto the molecular part PDOS for N_{in} junctions of different coverages Θ. PDOS does not shift much when changing the coverage

6.1 Origin of Collective Effects

To investigate the origin of the trends in the PDOS found so far for N_{in} and N_{out} molecular junctions of different coverages, the systems will be split into separate fractions, as described in section 4.4. On the one hand, the effect stemming from the metal-molecule-bond formation will be investigated, and, on the other hand, the hypothetical case of a free standing monolayer. The collective contributions of these two effects should essentially explain the coverage-dependent behaviour of the respective metal-molecule-metal systems.

Metal-Molecule Bond Formation

As a first step the effect of the metal-molecule-bond formation in molecular junctions will be investigated. For both systems, N_{in} and N_{out}, the bond dipole ΔE_{BD}, associated with the charge rearrangements upon bond formation will be analysed. Since there is a thiol docking group for both systems it is mainly a bond replacement rather than a bond formation, as was already discussed in section 4.4.

Fig. 36a and 36c show the plane averaged charge-density rearrangements $\Delta\rho$, according to Eq. 4.5b, between the molecular junction and the sum of the corresponding subsystems for full coverage for the N_{in} and N_{out} junction, respectively. For both systems they are strongly localized at the contact region between metal and molecule and do not significantly extend into the region of the molecular backbone. The resulting dipoles strongly affect the electrostatic potential at the interface region. This can be seen in Fig. 36b and d, where the plane averaged potential-energy difference between the whole systems and the sum of the subsystems, ΔE_{BD}, for different coverages is shown. Note that this

is a (x,y)-plane averaged potential and, therefore, care should be taken with the interpretation at lower coverages, where an average across a very big unit cell is performed. As was already mentioned in the introduction (section 1.2), Natan et al. found in their work [34] that the characteristic decay-length of the electric field for a two-dimensional array of dipoles is $d/(2\pi)$, with d being the lateral distance of the dipoles. With this, we can estimate this decay-length for lowest coverage, $\Theta = 0.0625$, to be approximately $16\mathring{A}/2\pi \approx 3\mathring{A}$. Therefore, the average potential for lower coverages is a good approximation.

In contrast to the aforementioned different coverage effect of the N_{in} and N_{out} junctions (Fig. 35 and 34), there is a strong coverage dependence of the bond dipole, ΔE_{BD}, for both of the systems in a similar way. ΔE_{BD} drops sharply at the contact and becomes approximately flat inside the monolayer. Of course there is a difference in the local shape of ΔE_{BD} at the contact region, due to the different positions of the nitrogen atoms in N_{in} and N_{out}. The potential drop at the center reduces with decreasing monolayer density, starting with about -0.74 eV for full coverage resulting in only -0.16 eV for lowest coverage for the N_{in} system. In the case of N_{out} the bond dipole at full coverage is about -0.98 eV and reduces to -0.09 eV for lowest coverage.

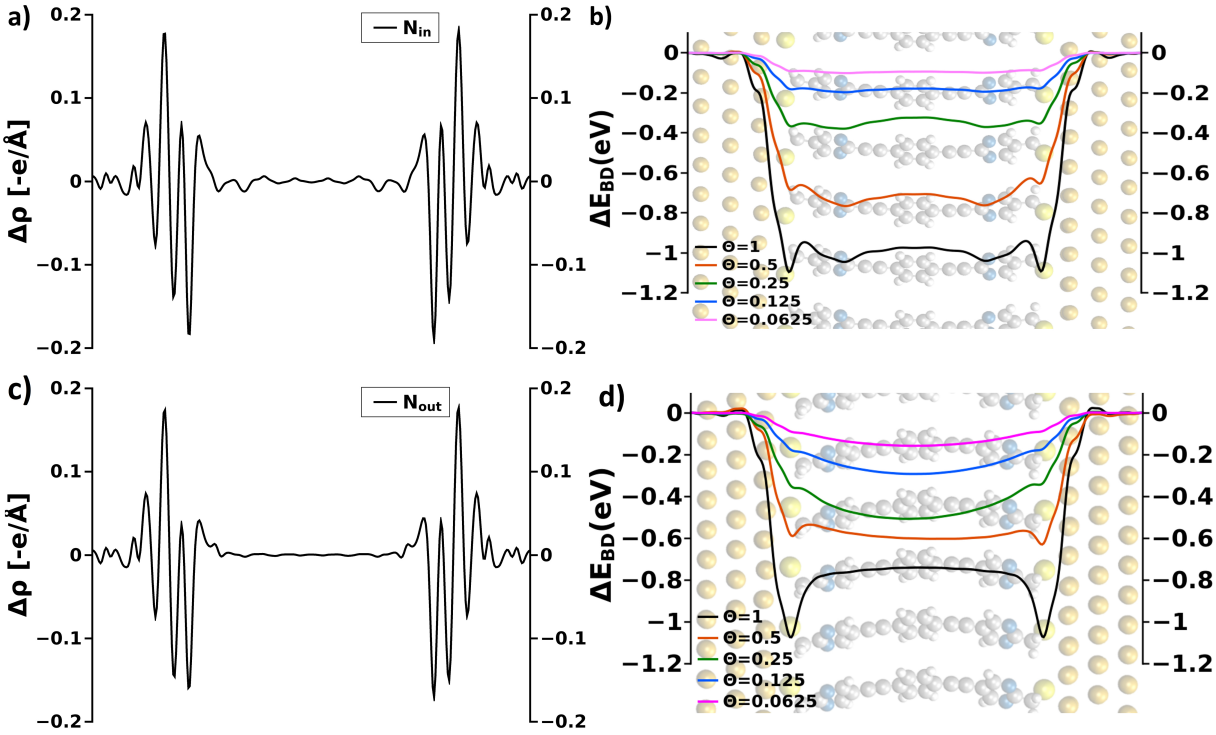

Figure 36: Charge rearrangements $\Delta\rho$ upon bond formation and corresponding jump in the electrostatic potential energy, referred to as Bond dipole ΔE_{BD} for N_{in} (a), (d) and N_{out} junctions (c), (d) of different coverages Θ. Charge rearrangements are mainly concentrated to the interface region, as well as the bond dipole, that decreases when lowering the coverage.

The first collective effect, investigated here, is very similar for both systems, contrary

to the behaviour that was found regarding the coverage dependent shifts in the PDOS. Further investigations need to be done to describe the different effects in the PDOS of the junctions comprising N_{in} and N_{out} molecules.

Free-standing Monolayer

The second step to investigate the coverage effects in more detail is to look at the hypothetical case of a free standing monolayer in the absence of the gold electrodes. In this case, the molecules are frozen corresponding to the optimized geometry of the whole junction and the sulfur is saturated with hydrogen. Again VASP calculations can be done for different coverages. Fig. 37 shows the results for N_{in} and N_{out} monolayers of different densities. One can see the coverage dependent HOMO and LUMO energies aligned to the vacuum level for both systems depending on the coverage Θ. The reported values correspond to the peaks in the corresponding DOSs. Now, for the N_{in} monolayer there is a pronounced shift of about 1 eV when going from lowest to highest density (black line), while the N_{out} monolayer exhibits only a slight coverage dependent shift. In contrast to the metal-molecule-metal systems (Fig. 34 and 35), a complete opposite behaviour is found for the free standing SAMs.

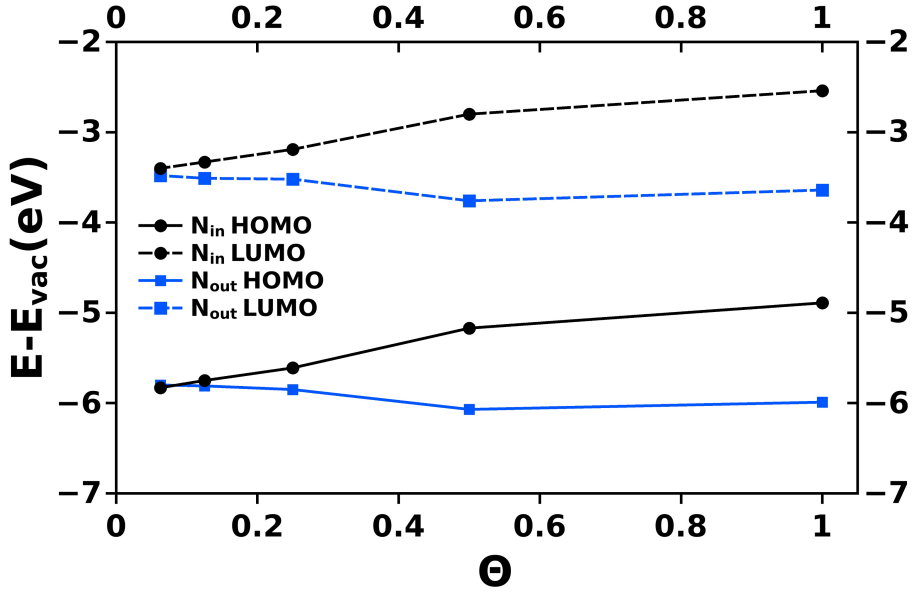

Figure 37: HOMO and LUMO energies aligned to the vacuum energy for N_{in} and N_{out} monolayers of different densities Θ

This can be explained by looking at the electrostatics of the local dipoles of the free standing monolayer, as was initially discussed in section 1.2. For the N_{in} molecule, local dipoles at the peripheries were generated by introducing pyrimidine rings with nitrogens on the inner side. Assembling these molecules into a monolayer of different coverages corresponds to adding up local dipoles of different densities. The summation of these local dipoles leads to a dipole layer, that introduces a step in the electrostatic potential V according to its dipole density $D = \mu/A$:

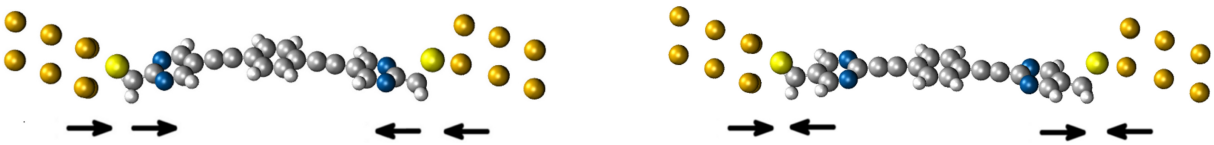

Figure 38: Collective effects of N_{out} (left side) and N_{in} (right side) junctions; the arrows are indicating the counteracting effects of the bond formation and the local dipoles for N_{in} and the compound effects for N_{out}

$$\Delta V = -\frac{1}{\epsilon_0} D(\vec{r}). \tag{1.2}$$

Since for the N_{out} molecule these polar bonds at the peripheries of the molecule point into opposite direction, they partly cancel resulting in a very small coverage dependent shift of about 0.2 eV, as can be seen in Fig. 37 (blue line).

The second collective effect found on the basis of the free-standing monolayer is very different for N_{in} and N_{out}, and can, together with the effect stemmig from the molecule-metal bond formation essentialy explain the trends of the coverage dependent PDOS shifts of the corresponding metal-molecule-metal systems.

Combining two collective effects

A combination of the two collective effects, found so far, can indeed provide the answer to the diffenert coverage-dependent effects of junctions consisting of isomeric N_{in} and N_{out} molecules. As can be seen from the arrows indicated in the left panel of Fig. 38 for the N_{out} molecule the effect coming from the metal-molecule bond formation and one for the free standing monolayer add up, leading to a shift of about 0.5 eV in the DOS, when going from single molecule to full monolayer. In contrast, for the N_{in} molecule these two effects are counteracting and fully cancel, see right panel of Fig. 38, leading to a vanishing coverage-dependent effect for this molecular junction.

To obtain also a quantitative description of these trends, we want to discuss these collective electrostatic effects on the basis of the following equations:

$$\delta E_{HOPS} = \delta E_{HOMO} + \delta E_{BD} + 2\delta E_{corr}^{HOMO} \tag{6.1a}$$

$$\delta E_{LUPS} = \delta E_{LUMO} + \delta E_{BD} + 2\delta E_{corr}^{LUMO} \tag{6.1b}$$

These quantities are schematically illustrated in Fig. 39 on the example of the reference system $Tour_{CH_2SH}$ and the concept shall be now explained on the basis of this system. δE_{HOTC} and δE_{LUTC} define the energy shifts of the HOTC and LUTC when going from full coverage, $\Theta = 1$, to lowest coverage ,$\Theta = 0.0625$, in the corresponding metal-molecule-metal system (Fig. 39a). These shifts should in principle be explained by a combined action of the collective effects stemming from the free standing monolayer and the ones coming from the bond formation. δE_{HOMO} and δE_{LUMO} define the energy shifts of the HOMO and LUMO when going from full density $\Theta = 1$ to lowest density $\Theta = 0.0625$ in

the free standing monolayer (Fig. 39b). δE_{BD} defines the energy difference of the bond dipole between full coverage $\Theta = 1$ and lowest coverage $\Theta = 0.0625$ in the middle of the molecular backbone (Fig. 39c). A quantitative analysis of the trends revealed that the coverage dependent energy shifts in the PDOS of the molecular junction cannot just be described by simply adding the bond dipole effect to the alignment in the non-interacting case. Rather, small correction terms $\delta \mathrm{E}_{\mathrm{corr}}^{\mathrm{HOMO}}$ and $\delta \mathrm{E}_{\mathrm{corr}}^{\mathrm{LUMO}}$ have to be added, which altogether leads to the aforementioned Eq. 6.1a and 6.1b.

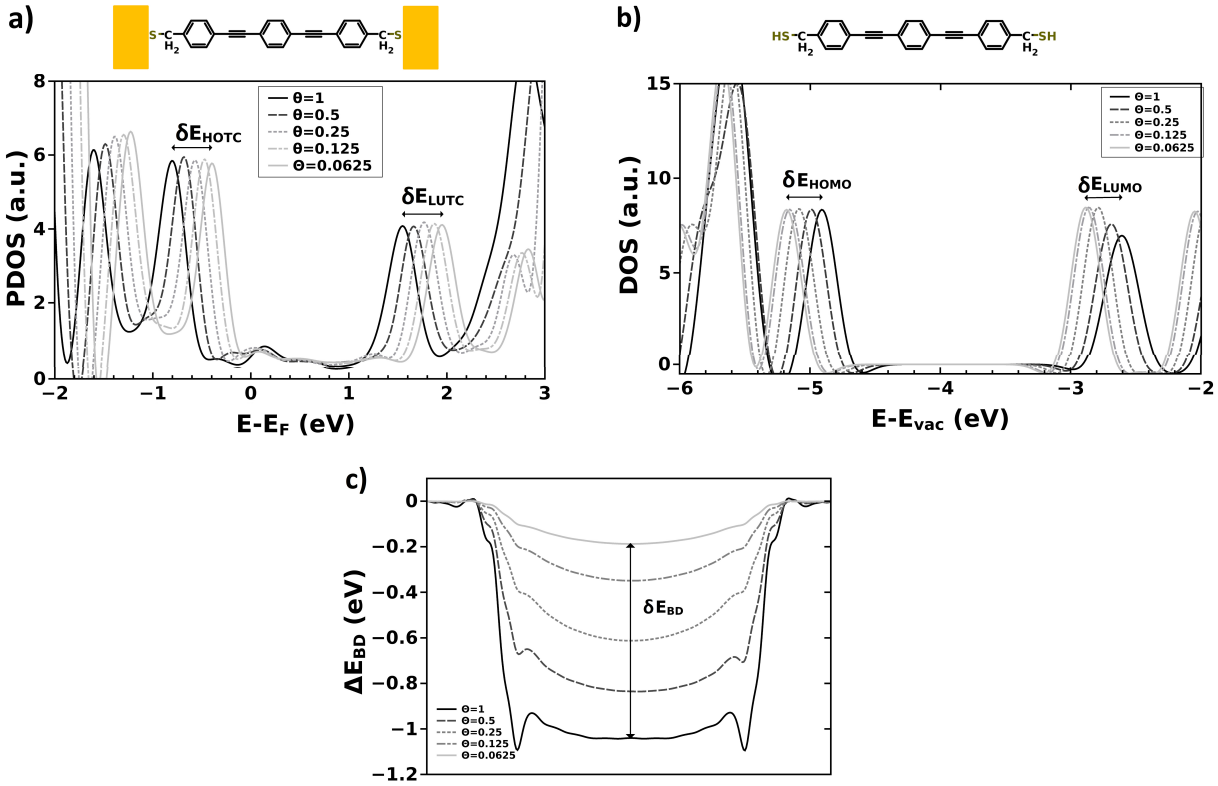

Figure 39: Schematic representation of the quantities described in Eq. 6.1a and 6.1b on the example of the reference system $\mathrm{Tour}_{\mathrm{CH_2SH}}$. a) PDOS of the **molecular junction** for different coverages; $\delta \mathrm{E}_{\mathrm{HOTC}}$ and $\delta \mathrm{E}_{\mathrm{LUTC}}$ define the energy shift of the HOTC and LUTC when going from full coverage $\Theta = 1$ to lowest coverage $\Theta = 0.0625$. b) DOS of the **free-standing monolayer** for different densities; $\delta \mathrm{E}_{\mathrm{HOMO}}$ and $\delta \mathrm{E}_{\mathrm{LUMO}}$ define the energy shift of the HOMO and LUMO when going from full coverage $\Theta = 1$ to lowest coverage $\Theta = 0.0625$. c) Shift in the electrostatic potential due to **bond formation** for different coverages; δE_{BD} defines the energy difference between full coverage $\Theta = 1$ and lowest coverage $\Theta = 0.0625$ in the middle of the molecular backbone.

The correction terms, $\delta \mathrm{E}_{\mathrm{corr}}^{\mathrm{HOMO}}$ and $\delta \mathrm{E}_{\mathrm{corr}}^{\mathrm{LUMO}}$, which were also introduced in [101], [35], [107] for metal-SAM systems, can be rationalized by the fact that (i) the bond formation between metal and SAM slightly perturbs the internal electronic structure of the SAM and, consequentely sligthly modifies its energy levels, and (ii) for lower coverages the potential drop, δE_{BD}, is not sudden at the interface. $\delta \mathrm{E}_{\mathrm{corr}}^{\mathrm{HOMO}}$ and $\delta \mathrm{E}_{\mathrm{corr}}^{\mathrm{LUMO}}$ were already found to be coverage-dependent, in a work done by Romaner et al. [91], where the dependence of the

electronic structure of Au(111) covered by SAMs of conjugated molecules on their packing densitiy was investigated. Typical values are < 0.3 eV and in most cases decrease with increasing chain length [35]. For comparison with the aforementioned papers δE_{corr}^{HOMO} and δE_{corr}^{LUMO} have to be taken twice, since in the case of molecular junctions two metal-SAM contacts are established.

The quantities described in Eq. 6.1a and 6.1b shall now be evaluated for the N_{in} and N_{out} junctions. Table 4 summarizes the values. The shifts of N_{in} and N_{out} junctions can

Table 4: Quantities described in Eq. 6.1a and 6.1b for N_{in} and N_{out} molecular junctions: $\delta E_{HOTC}/\delta E_{LUTC}$ are the differences in the HOTC/LUTC energies between full monolayer and single molecule junctions. $\delta E_{HOMO}/\delta E_{LUMO}$ are the differences in the HOMO/LUMO energies between the corresponding free full monolayer and single molecule. δE_{BD} reflects the energy difference of the bond dipole upon charge rearrangements between full coverage and lowest coverage. δE_{corr}^{HOMO}, δE_{corr}^{LUMO} are correction energies.

Systems	δE_{HOTC}/eV	δE_{HOMO}/eV	δE_{BD} /eV	δE_{corr}^{HOMO}/eV
N_{in}	-0.08	-0.94	0.87	-0.01
N_{out}	0.47	0.18	0.58	-0.15
Systems	**δE_{LUTC} /eV**	**δE_{LUMO}/eV**	**δE_{BD} /eV**	**δE_{corr}^{LUMO}/eV**
N_{in}	0.00	-0.86	0.87	0.05
N_{out}	0.47	0.16	0.58	-0.14

indeed be explained by a combined investigation of two collective effects, stemming on the one hand from the free standing monolayer, assigned by its local dipoles, and on the other hand from the metal-molecule bond formation. The correction terms for N_{in} is very small: -0.01 eVand -0.05 eV for the HOMO and LUMO, respectively. This is in agreement with the largely stretched thiol docking group including the methylene spacer. N_{out} exhibits larger correction terms: -0.15 eV and -0.14 eV for the HOMO and LUMO. This has to be investigated in more detail in the future. Higher correction terms will be found for some of the investigated systems with different docking groups that exhibit stronger couplings, see section 7.

Summarizing, two isomeric molecules N_{in} and N_{out}, that are essentially the same in gas phase and very similar in single molecule junctions, were found to behave very differently when assembled in molecular junctions of high densities. Responsible for this different behaviour are collective electrostatic effects. Interestingly, these collective effects can also be switched off by cleverly designed electrostatic dipoles, as in the case of N_{in} junctions. This strategy offers a possibility to selectively control collective electrostatic effects.

6.2 Transport Calculations

As already mentioned in chapter 2 I had to switch from VASP to SIESTA to do transport calculations on the basis of combined DFT and Green's function techniques. As a

first step, a comparison between these two codes is necessary. The focus will be on the density of states as this is a quantity highly relevant for transport. Surprisingly, SIESTA calculations with commonly used parameters resulted not only in a mismatch in energy compared to VASP, but also in a quite large reduction of the collective effects that were found for N_{in} and N_{out} junctions.

6.2.1 Testing Parameters in SIESTA

To adjust the level alignment to that obtained from VASP a lot of parameters were tested, with special emphasis on the `PAO.BasisSize`, `PAO.EnergyShift`, `MeshCutOff`, `DM.Tolerance` and `DM.MixingWeight`. These investigations shall be summarized for the N_{in} molecular junction.

PAO.BasisSize
As mentioned in section 2.1.5 the size of the basis set can either be chosen from the pre-supplied `SZ`, `SZP`, `DZ` and `DZP` basis functions or can be generated considering the restriction of finite-support, atomic-like basis functions. In this thesis the preset basis functions were used.

In [108] Strange et al. compared transmission functions using a DFT based plane wave code and the SIESTA code. They found that the transmission functions converges towards the plane-wave result as the SIESTA basis is enlarged and in particular the `DZP` basis provides sufficient agreement.

Unfortunately, these trend could not be reproduced for the systems investigated in this thesis. Fig. 40 shows the DOS for the N_{in} junction at full coverage, $\Theta = 1$, obtained from SIESTA, as a function of basis set (solid lines) and the one obtained from VASP with `ENCUT`= 273.894 (dashed line). Since in SIESTA the DOS is determined per spin, the curves have half of the height compared to VASP. (To better compare the results obtained from SIESTA and VASP in the corresponding figures, the heights have not been adapted.) When extending the basis set from `SZ` (pink line), to `SZP` (blue line), to `DZ` (green line) and `DZP` (orange line), no systematic convergence can be achieved. (Such a test was also done for lowest coverage, obtaining an equivalent result.) As was seen in many other works, the best agreement can be obtained with the `DZP` basis set, but there remained an energy shift of about 0.1 eV to lower energies compared to the plane wave result.

This energy difference between the two codes was initially intended to be accepted, but when changing the coverage in N_{in} and N_{out} junctions, unpredictable problems arose resulting in worse agreement compared to VASP when going to lower densities. This can be seen in Fig. 41a and b for N_{in} and N_{out}, respectively. In the SIESTA calculations, the black line corresponding to $\Theta = 1$ and the orange one corresponding to $\Theta = 0.5$, reflect the plane-wave result relatively well, but for lower densities huge discrepancies are found. Especially for the lowest coverage, $\Theta = 0.0625$ there is a disagreement of 0.33 eV in the case of N_{in} and 0.27 eV in the case of N_{out}. But also for $\Theta = 0.25$ and $\Theta = 0.125$ there is a significant mismatch.

This disagreement dramatically weakens at the same time the collective electrostatic ef-

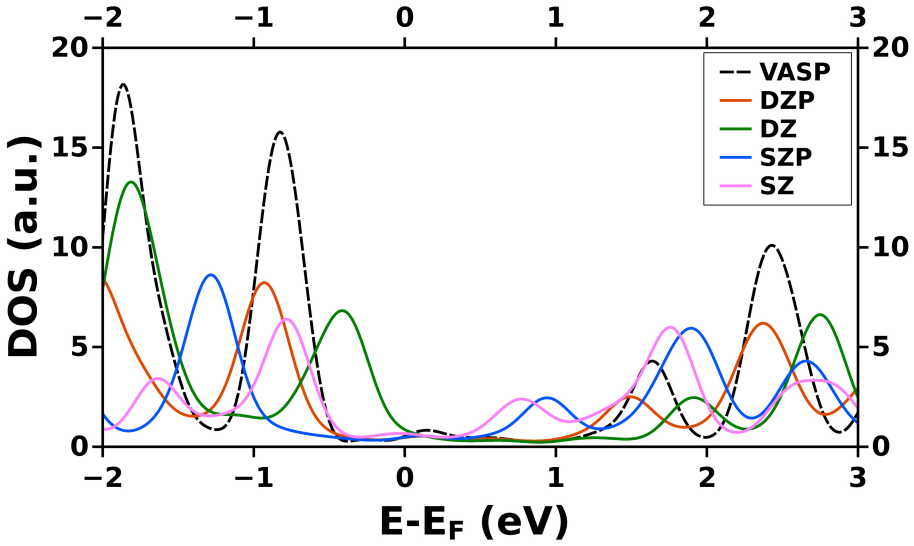

Figure 40: DOS of N_{in} junction obtained from SIESTA for different basis sets (solid lines) compared to results obtained from VASP (dashed black line). There is no systematic trend when enlarging the basis set. With an energy difference at the HOMO of 0.1 eV between SIESTA and VASP, the `DZP` basis set provides the best agreement. (Since in SIESTA the DOS is determined per spin, the curves have half of the height compared to VASP.)

fects obtained from VASP, leading to even opposite trends than the ones found with VASP. This shows that with the standard set of parameters one cannot describe the collective effects. Since `DZP` is the best basis set provided, other parameters were tested trying to improve the situation.

MeshCutOff
For calculations of integrals or potentials and charge densities, SIESTA defines a three dimensional grid, whose fineness is determined by its plane-wave cut off, also called the `MeshCutOff` [71]. All periodic plane waves with kinetic energies lower than the cut off can be represented in the grid without aliasing. Besides the default value of 100 Ry, `MeshCutoff` was also set to 150 Ry, 200 Ry and 300 Ry for N_{in} and $Tour_{SH}$ junctions. The default value provides the result most similar compared to VASP, closely followed by the other values, all leading to essentially the same alignment of the DOS.

DM.Tolerance
With regard to the SCF convergence, a very important parameter is the tolerance of the density matrix, `DM.Tolerance` [71], defined as the maximum difference between the output and input charge density in a SCF cycle. `DM.Tolerance` was set to 10^{-4} (default value), 10^{-5} and 10^{-6} for the N_{in} and $Tour_{SH}$ system. For sure, with decreasing density matrix tolerance the amount of steps increased, but no differences in the DOS were found. Hence 10^{-4} was taken, as it is the fastest one.

PAO.EnergyShift
A crucial parameter, that was found providing the means to significantly increase the agreement with VASP is the `PAO.EnergyShift` [71]. This is a single parameter defining the confinement radii of all different orbitals, i.e., the energy increase that each orbital

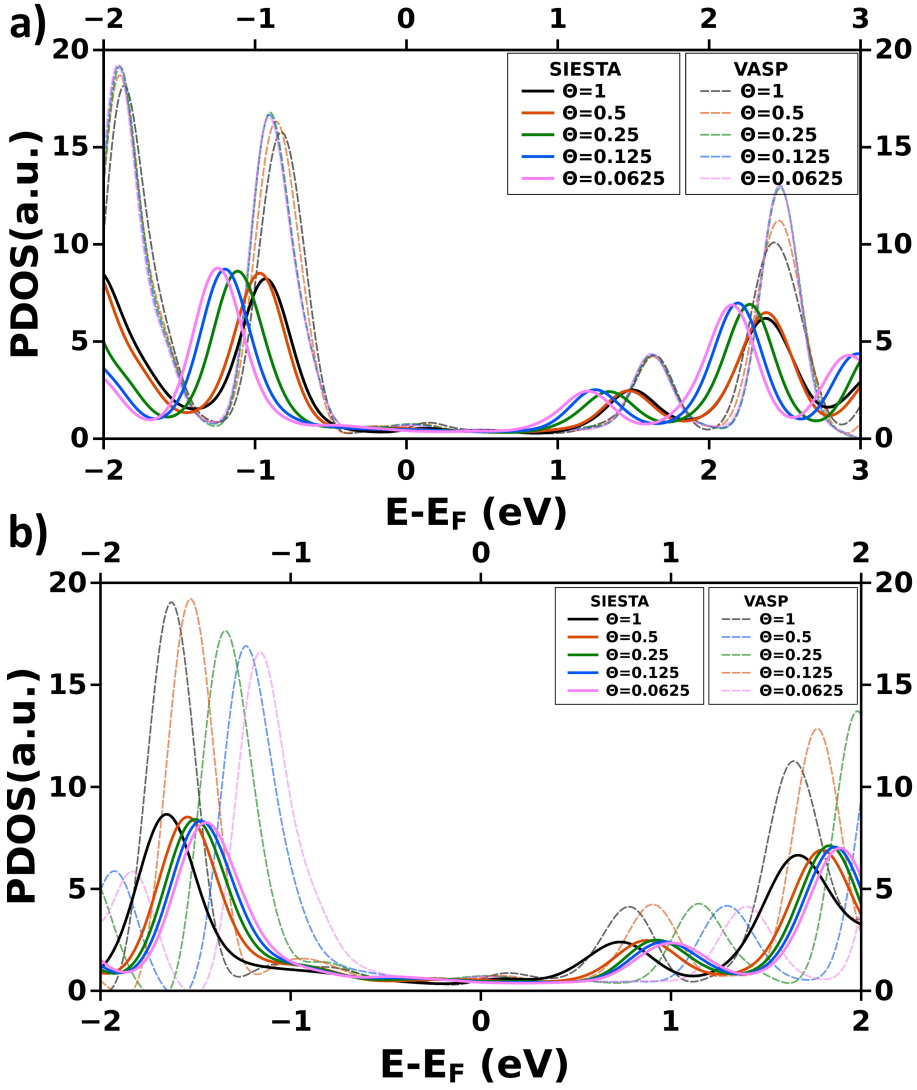

Figure 41: Coverage dependent PDOS of N_{in} junctions (a) and N_{out} junctions (b) obtained from SIESTA (solid lines) and VASP (dashed lines) for a `PAO.EnergyShift` of 0.01 eV. For full coverage there is a good agreement, but when decreasing the coverage, a significant mismatch between the codes is found. (Since in SIESTA the DOS is determined per spin, the curves have half of the height compared to VASP.)

experiences when confined to a finite sphere. With this parameter one can uniquely specify the range of the orbitals, determined by the cut off radius, beyond which the strictly localized orbitals are zero.

Typical default values, that were found to provide good agreement with plane-wave codes are $0.01 - 0.02$ Ry [108]. Its indirect relationship with the confinement of the orbitals, leads to very strongly localized atomic orbitals for high `PAO.EnergyShifts`. A small `PAO.EnergyShift` means more extended orbitals.

For the systems investigated in this work an agreement with VASP could not be found for the typical default values; at least not for lower coverages. But decreasing the `PAO.EnergyShift` led to better results. Going to lower energy shifts yields more extended basis functions, more and more approaching the plane wave result. Fig. 42 shows the PDOS of the N_{in} junction for different `PAO.EnergyShift`s for full coverage $\Theta = 1$. One can clearly see a shift into the right direction when lowering the `PAO.EnergyShift`, leading to a perfect agreement between VASP and SIESTA for full coverage for a `PAO.EnergyShift` of 0.001 Ry ($\Delta E = 0.06$ eV). Lowering the `PAO.EnergyShift` even more, does not improve the situation.

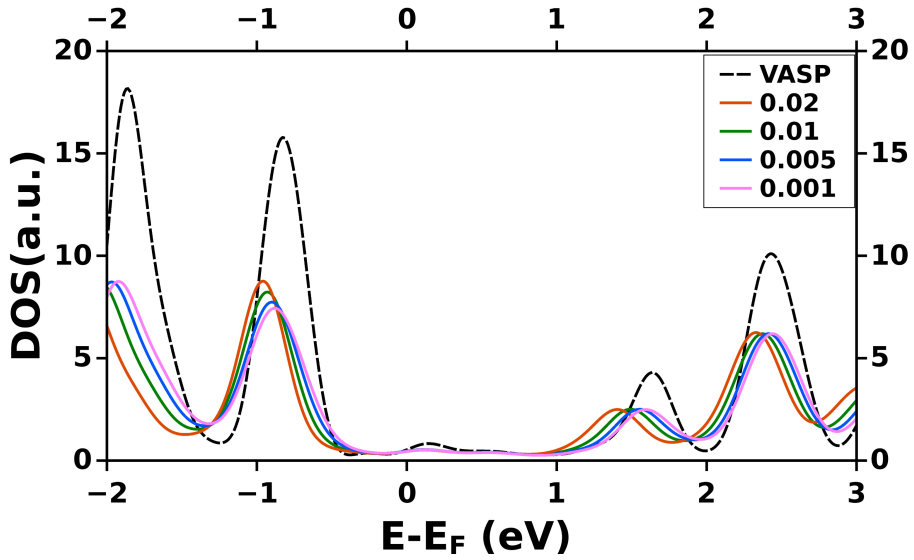

Figure 42: PDOS of N_{in} junction obtained from SIESTA for different `PAOEnergyShift`s in Ry compared to results obtained from VASP. (Since in SIESTA the DOS is determined per spin, the curves have half of the height compared to VASP.)

Utilizing the impact of this parameter N_{in} junctions with different coverages were calculated with the lowest `PAO.EnergyShift` of 0.001 Ry. In comparison to the aforementioned mismatch that was obtained with a `PAO.EnergyShift` of 0.01 Ry (Fig. 41), results could be improved considerably and now the general trends are reproduced, as can be seen in Fig. 43a and b. Still there is an increasing quantitative deviation when going to lower coverages, leading to a difference of about 0.1 eV for the lowest coverage $\Theta = 0.0625$ for N_{in} as well as for N_{out}.

A cause for this behaviour could be that the localized basis sets used in SIESTA can-

not describe the vacuum region very well. Going to lower coverages, means increasing the size of the unit cell and, therefore, introducing more and more vacuum. This could be a reason why the discrepancies increase with decreasing coverage. Keeping this in mind, the next step to improve the situation should be introducing ghost atoms into the vacuum region.

Ghost Atoms
Ghost atoms, or floating orbitals possess basis functions in positions determined by their coordinates, but do not affect the calculation. This means that no charges or projectors, i.e. no pseudopotentials or electrons are considered for these atoms. In this way we have the possibility to describe the vacuum region with basis functions specified on dummy centres, as can be seen in Fig. 44, where the pale molecules represent the ghost atoms.

In SIESTA ghost atoms can be defined by giving them a negative atomic number Z shown for the example of the N_{in} molecule as a part of the corresponding `.fdf` file:

```
%block ChemicalSpeciesLabel
   1    79   Au
   2    16   S
   3    6    C
   4    1    H
   5   -16   S_ghost
   6   -6    C_ghost
   7   -1    H_ghost
%endblock ChemicalSpeciesLabel
```

In addition, appropriate pseudopotential files have to be generated by just copying the `.psf` and renaming them into `_ghost.psf` respectively.

When doing these calculations with the optimum parameters found so far (`DZP` basis set, `PAO.EnergyShift` of 0.001 Ry) the situation cannot be improved. Tested on the example of $Tour_{SH}$ single molecule junction with $\Theta = 0.0625$, an energy shift in the DOS between the calculation with and without ghost atoms of only 0.02 eV was found. This is negligible, as can be seen from Fig. 45 (solid lines).

It was concluded that for this low `PAO.EnergyShift`, basis functions sufficiently tail into the vacuum region and, therefore, introducing additional basis functions into that region will not provide any essential improvement. To ensure that there was no error in my definitions of the ghost atoms, the same calculation done with a higher `PAO.EnergyShift` of 0.01 eV. Indeed, then a shift of about 0.12 eV into the right direction was found, as illustrated in Fig.45 (dashed lines).

The pale, black line in Fig.45 represents the VASP result. Obviously introducing ghost atoms could not improve the situation and the best results obtained from SIESTA are the ones already shown in Fig. 43a and b. But even though there are some discrepancies between VASP and SIESTA, slightly "weakening" the collective effects, the trends can be reproduced and collective effects can further be investigated calculating transport properties using SIESTA.

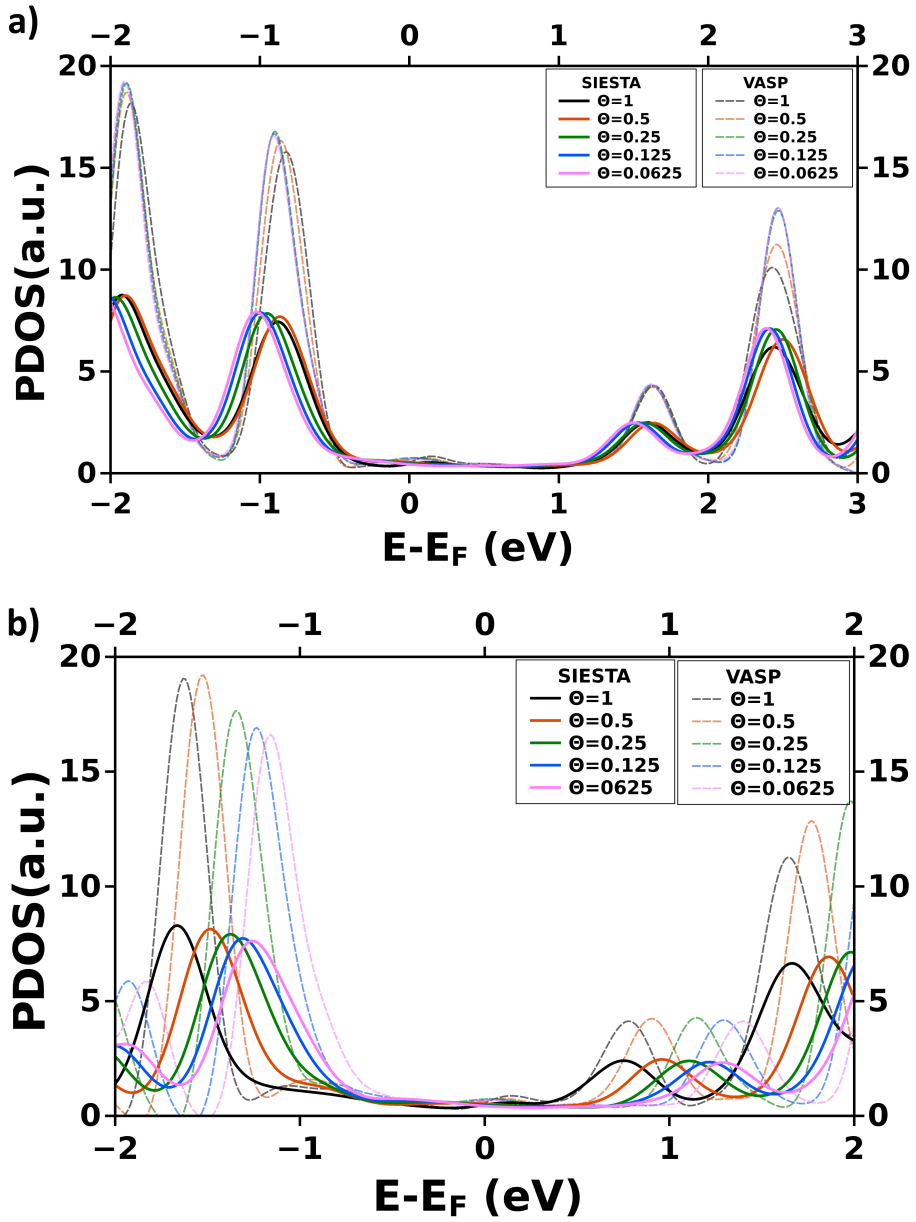

Figure 43: Coverage dependent DOS of N_{in} junctions (a) and N_{out} junctions (b) obtained from SIESTA (solid lines) and VASP (dashed lines) for a PAO.EnergyShift of 0.001 eV. (Since in SIESTA the DOS is determined per spin, the curves have half of the height compared to VASP.)

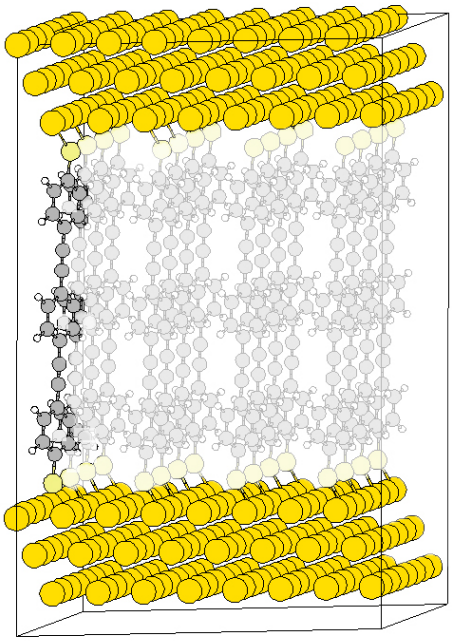

Figure 44: Unit cell for Tour_{SH} at $\Theta = 0.0625$ with ghost atoms (pale molecules) introduced into the vacuum region

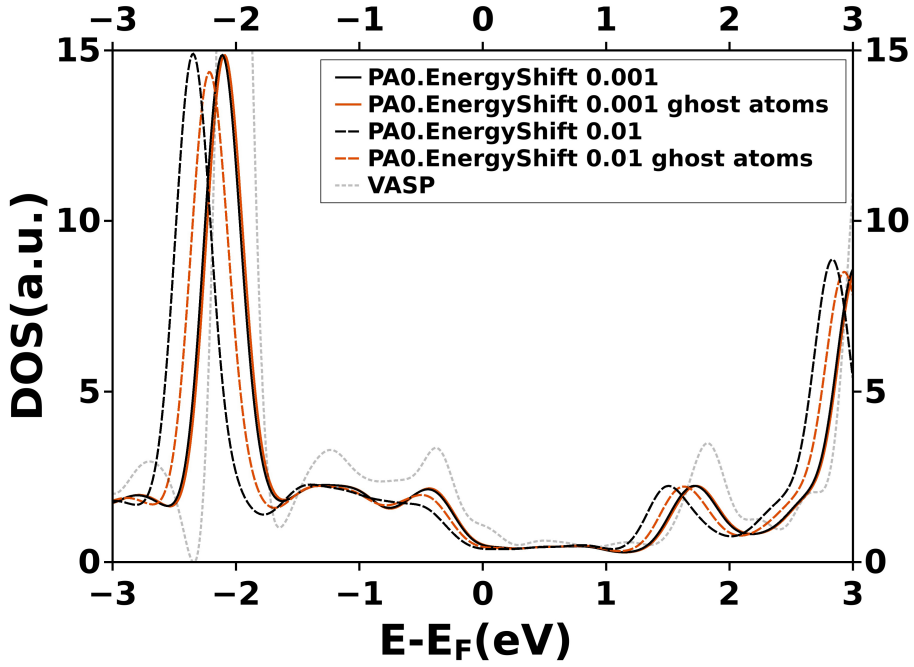

Figure 45: Effect of introducing ghost atoms in SIESTA on the example of Tour_{SH} at $\Theta = 0.0625$ for different `PAO.EnergyShifts` compared to the VASP result (grey, pale line). For the smallest energy shift 0.001 eV, the introduction of ghost atoms does not improve the situation. For more confined basis functions, when increasing the `PAO.EnergyShift` to 0.01 eV, an energy shift of 0.12 eV can be achieved by adding ghost atoms.

6.2.2 Current-Voltage Characteristics

In this section coverage dependent transmission functions and current-voltage characteristics of N_{in} and N_{out} junction are investigated using the SIESTAts code, that was extensively described in chapter 5.0.2. Additionally, there will be a comparison of the results obtained from $\text{SIESTA}_{\text{TS}}$ with the ones obtained from TRANSIESTA.

Full coverage junctions
At first a comparison of N_{in} and N_{out} junctions for full coverage $\Theta = 1$ shall be made. Fig. 46 shows the corresponding transmission functions (a) and resulting current-voltage characteristics (b) obtained from SIESTAts. What was calculated is the current per unit cell and since there is always one molecule in each unit cell of different coverage, it can be interpreted as current per molecule. The transmission function describes the probability for an electron to be transmitted through the SAM from one electrode to the other at a certain energy. One can clearly see the transmission channels contributing to the current. The two transmission curves differ in energy by about 0.88 eV for the highest occupied transport channel HOTC and 0.85 eV for the lowest unoccupied transport channel LUTC. The onset of the first transmission channel is slightly closer to E_F for N_{out} than for N_{in}, resulting in a slightly higher current per molecule for the N_{out} junction.

Since for N_{in} SAMs the HOTC is closer to E_F they provide p-type current (HOMO determined), meaning the electron concentration is higher on the cold electrode than on the hot electrode, driving the electrons from cold to hot. For N_{out} SAMs it is the other way round, since they provide a closest transport channel at an energy above E_F, leading to an electron flow from hot to cold and resulting in an n-type current.

When comparing the transport characteristics of N_{in} and N_{out} in Fig. 46 with the ones obtained in Ref [38] by David. A. Egger, reproduced in Fig. 5, differences can be found. This is due to the fact, that (i) geometries were fully optimized in this thesis, whereas they were only partly optimized in [38] and (ii) the `PAO.EnergyShift` is 0.001 Ry in this thesis and 0.01 Ry in Ref. [38]. When adapting the `PAO.EnergyShift` to 0.001 for both systems, see Fig. 47 for the N_{in} junction, the effect stemming from the geometry can be identified to be almost 0.2 eV. The influence of the `PAO.EnergyShift` was already discussed in section 6.2.1 and was here again found to be about 0.1 eV, see Fig. 48 (a) for the fully optimized N_{in} junction and (b) the partly optimized N_{in} junction of Ref. [38].

Since full coverage results could also be obtained from TRANSIESTA, a comparison between these codes shall be done at this point. Generally for TRANSIESTA enormous convergence problems were found for the `DZP` basis set combined with the small `PAO.EnergyShift`. Many parameters, like the `DM.Tolerance`, the `DM.MixingWeight`, or the `DM.NumberPulay` were varied to achieve convergence, with no success. A very crucial parameter concerning convergence in these systems, was the number of Au layers used in the central region. As schematically drawn in Fig. 49, a combination of 3 layers of gold in the electrode and 6 layers on each side of the central region finally led to converged results for full coverage. This is a relative surprising result, in the sense, that actually especially for the electrode 6 gold layers would be needed, to describe interactions correctly (see sec-

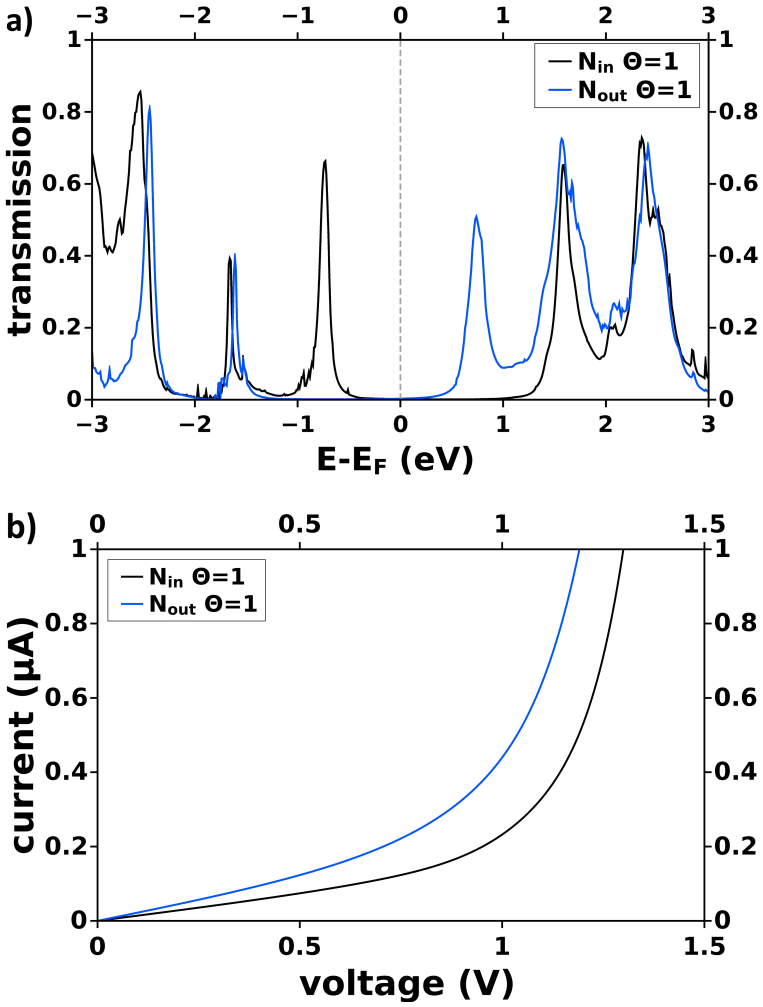

Figure 46: Transmission (a) and current per molecule (b) for N_{in} and N_{out} junctions of coverage $\Theta = 1$ obtained from SIESTAts

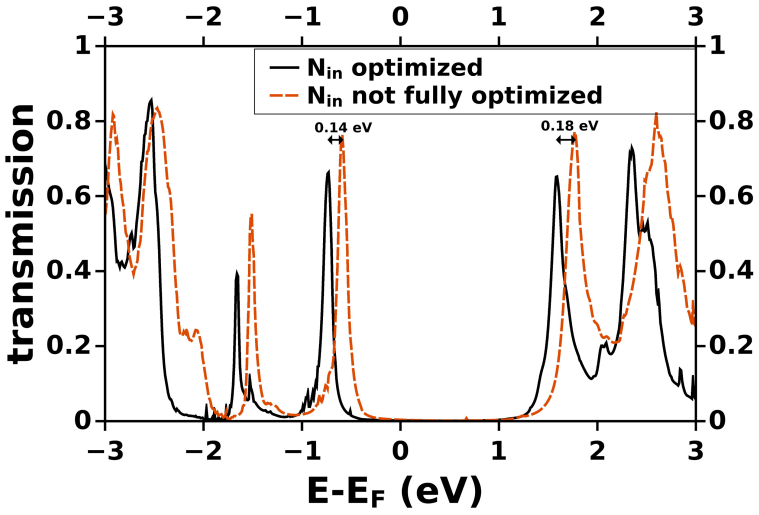

Figure 47: Transmission functions for the N_{in} full monolayer junction fully optimized in this thesis (black line) compared to the partly optimized N_{in} structure of Ref. [38] (orange line). The energy shift of the transmission peaks of about 0.2 eV completely stems from the different geometries.

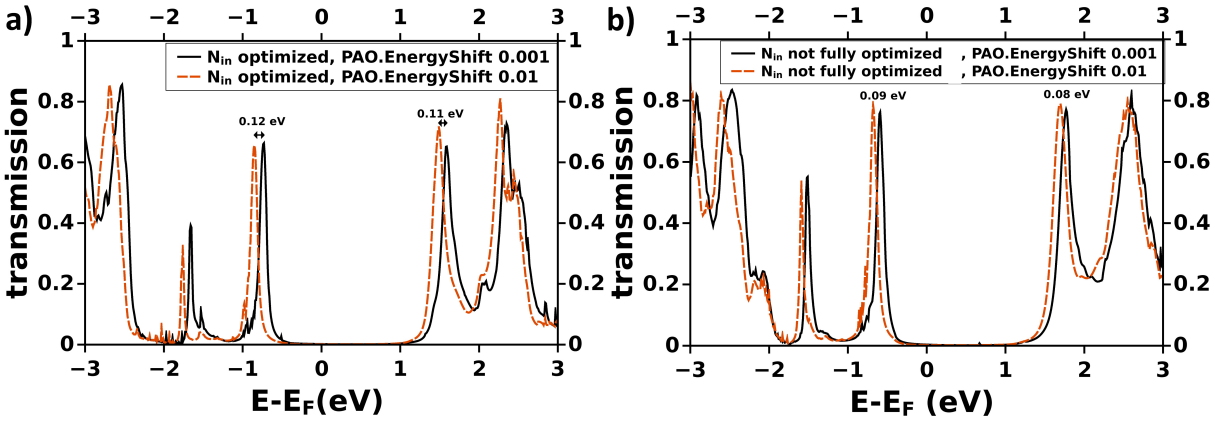

Figure 48: Transmission functions for the N_{in} full monolayer junction fully optimized in this thesis (a) and for the partly optimized N_{in} structure of Ref. [38] (b) for different `PAO.EnergyShifts` of 0.01 Ry (black line) and 0.001 Ry (orange line).

tion 5) and a combination of 6 layers in the electrode and 6 layers in the central region did not converge! This problem is still under investigation and parameters, like temperature and complex contour integration options will be more deeply investigated in the future. Nevertheless, a comparison of TranSiesta and Siesta was done and is shown in Fig. 49. The left panel (A) shows the transmission functions and (I-V)-characteristics of N_{in} and N_{out} SAM devices for TranSiesta and Siesta_{TS}. A rigid shift of about 0.1 eV can be found, stemming from the fact, that there were 6 layers of gold used on each side of the central region for TranSiesta, whereas there were 3 layers in the case of Siesta_{TS}. When adapting the number of gold layers used in the central region, one can find nice agreements between the two codes, as illustrated in the right panel (B).

Coverage dependent junctions
As a next step, transmission and current were calculated for N_{in} and N_{out} junctions as a function of coverage. Fig. 50 shows the coverage dependent transmission functions for N_{out}, that was produced by summing up all contributions from all k-points, according to Eq. 5.1. As was already found in section 6.1 by observing the corresponding Pdos, the transmission function also shows a significant coverage dependent effect of about 0.6 eV for N_{out} junctions when going from full monolayer to single molecule levels. Coverage-dependent calculations can be done for the N_{in} junctions, and again there is nearly no collective effect for this kind of molecule, as shown in Fig. 51.

From the transmission functions, one can easily get the current, applying the Landauer-Büttiker formula from Eq. 2.28. Fig. 53a shows the current-voltage characteristics for different coverages for the N_{out} junction. On the y-axis the current per molecule is plotted. There is a clear decrease in current per molecule when going to lower coverages. So the local environment, determined by collective electrostatic effects, makes the current per molecule vary for different coverages.

When investigating the charge transport polarity, as was described in section 4.2, one finds that almost all of the current is of n-type for coverages $\Theta = 1, 0.5$ and 0.25. For lower coverages there is, however, a switch from n to p-type current. This can also be easily seen in the corresponding Siesta Pdos (Fig. 43). Since the channel closest to the Fermi energy determines the charge transport polarity, there has to be a switch from n- to p-type for the transition from $\Theta = 0.125$ to $\Theta = 0.0625$, because then the Lutc is suddenly closer to E_F than the Hotc. Due to collective effects one can obviously achieve a switch in charge transport polarity for this kind of molecule as a function of coverage that results in a change in sign of the corrsponding Seebeck coefficient. I.e. for N_{out} one can change the charge transport polarity of the junctions by collective electrostatic effects.

Fig. 53a and b show the coverage dependent current-voltage characteristics and the corresponding charge transport polarities for the N_{in} molecule. Since there was almost no coverage effect in the Pdos or in the transmission, a very similar, slightly decreasing current per molecule is found, when decreasing the coverage. Since the Hotc for all coverages is closer to E_F, the current is of p-type for all densities and S does not change sign.

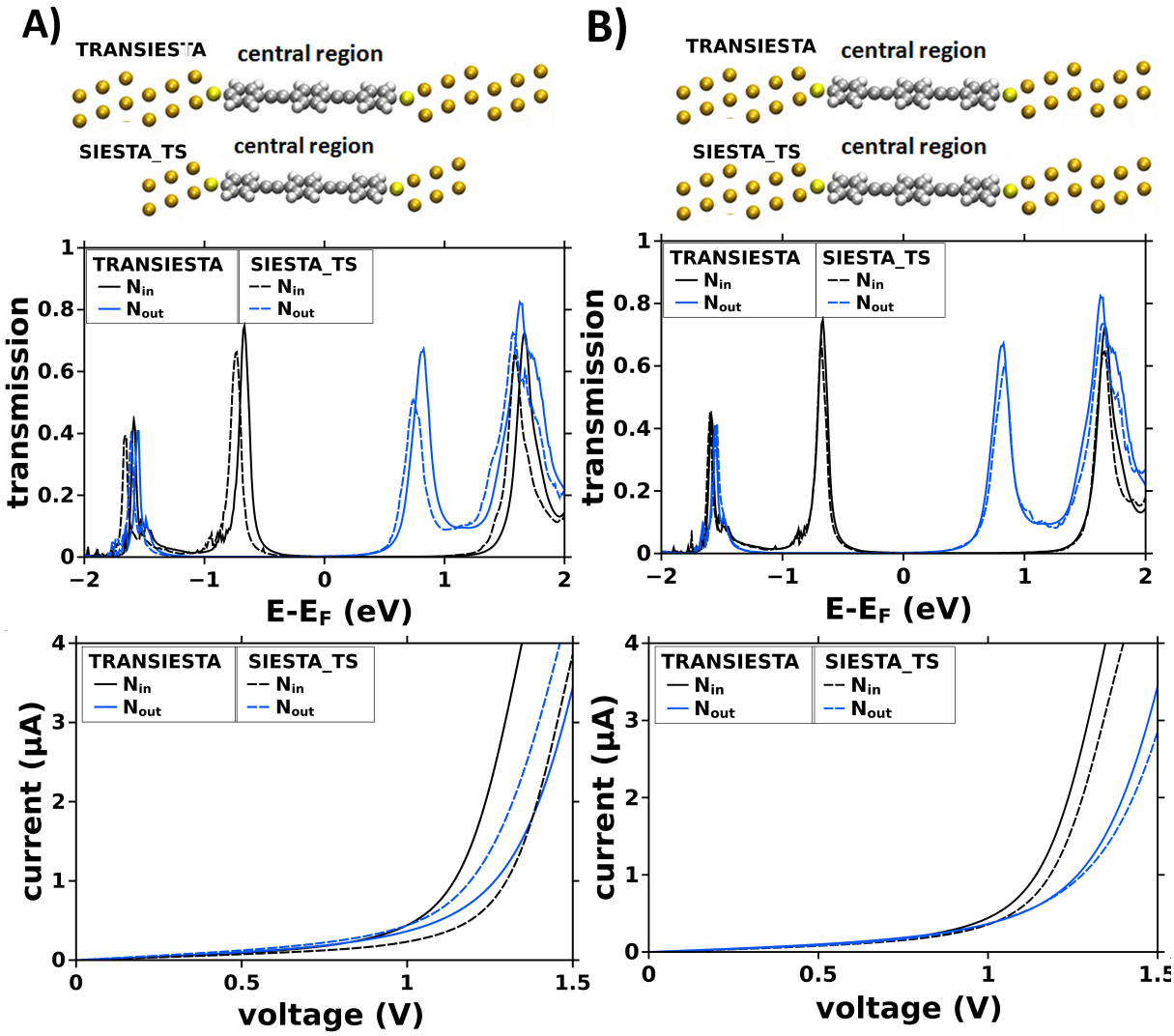

Figure 49: Comparison of transport properties obtained from TranSiesta and Siesta$_{TS}$ for N_{in} and N_{out} junctions of full coverage. (A) transmission function and current per molecule for 6 gold layers on each side of the central region for TranSiesta (to obtain convergence) and 3 layers of gold for Siesta$_{TS}$. A rigid shift of about 0.1 eV is observed. (B) transmission function and current per molecule for the same number of layers in the centralregion (6 for both cases). Almost identical transport characteristics can be found for the different codes.

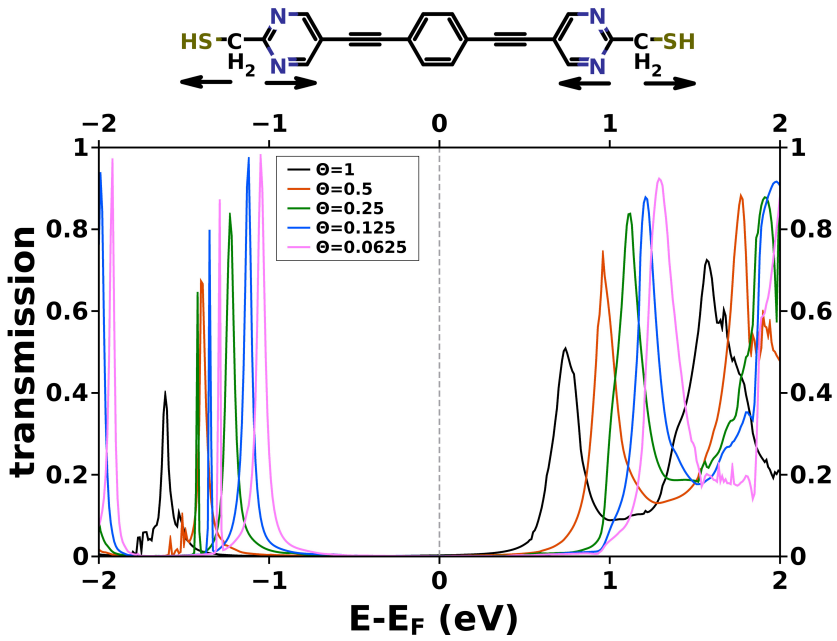

Figure 50: Coverage dependent transmission function for N_{out} junctions. A significant energy shift of about 0.6 eV are found when going from full monolayer to single molecule junctions due to collective electrostatic effects.

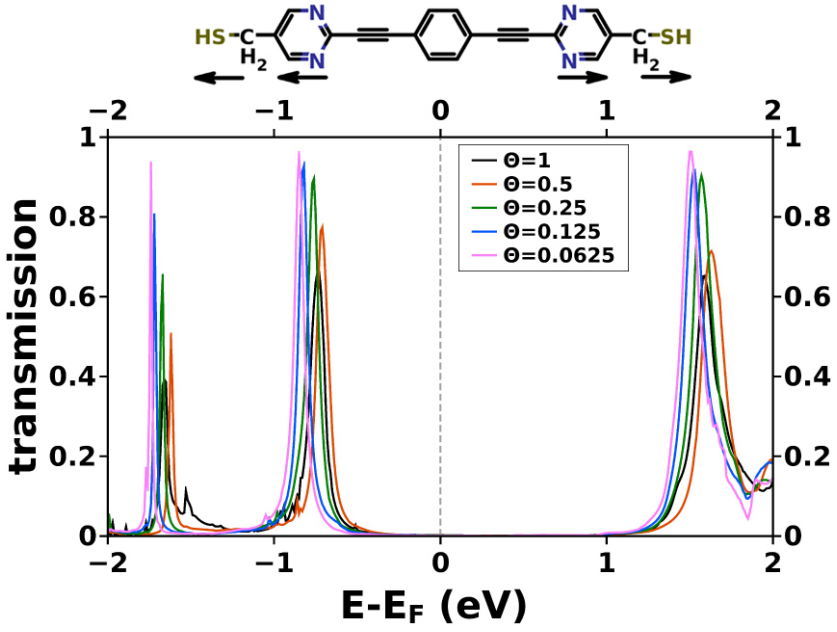

Figure 51: Coverage dependent transmission function for N_{in} junctions. A minor shift of -0.1 eV is found when going from full monolayer to single molecule junctions.

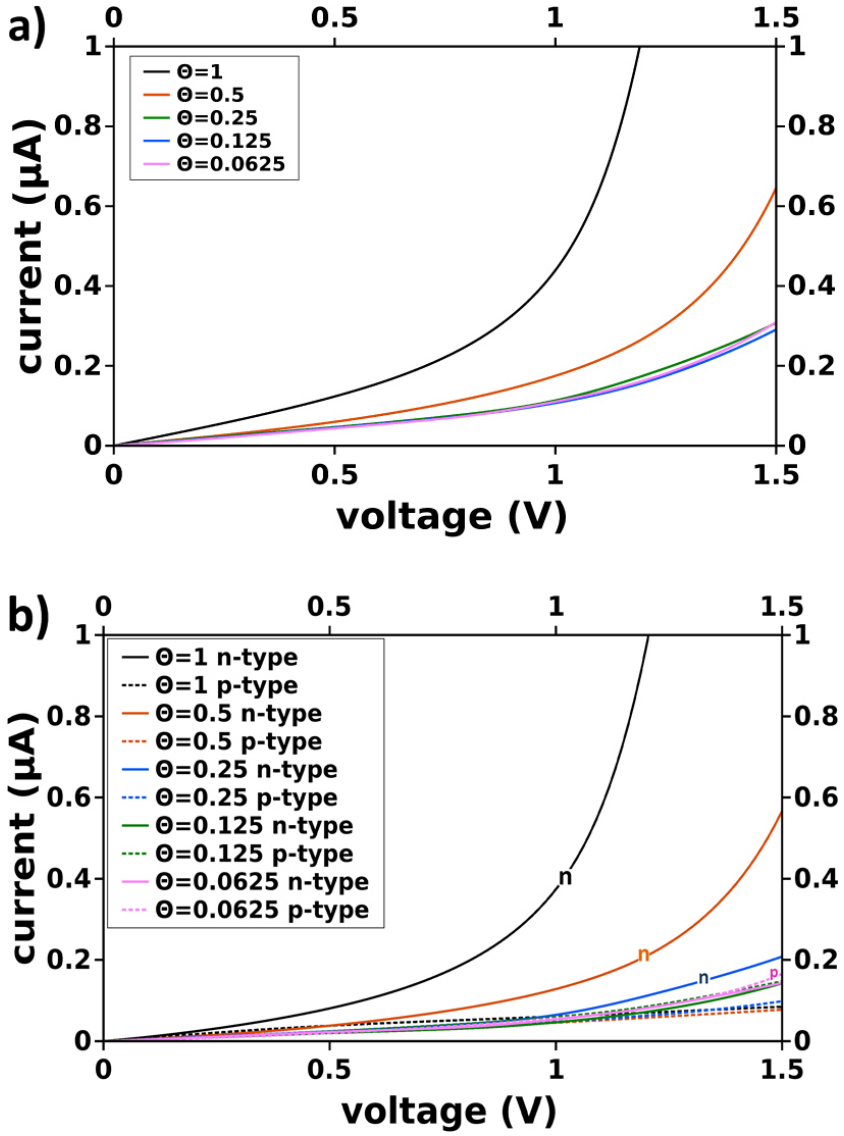

Figure 52: (a)Voltage dependent current per molecule for N_{out} junctions of different coverages Θ; (b) corresponding n-type and p-type currents per molecule

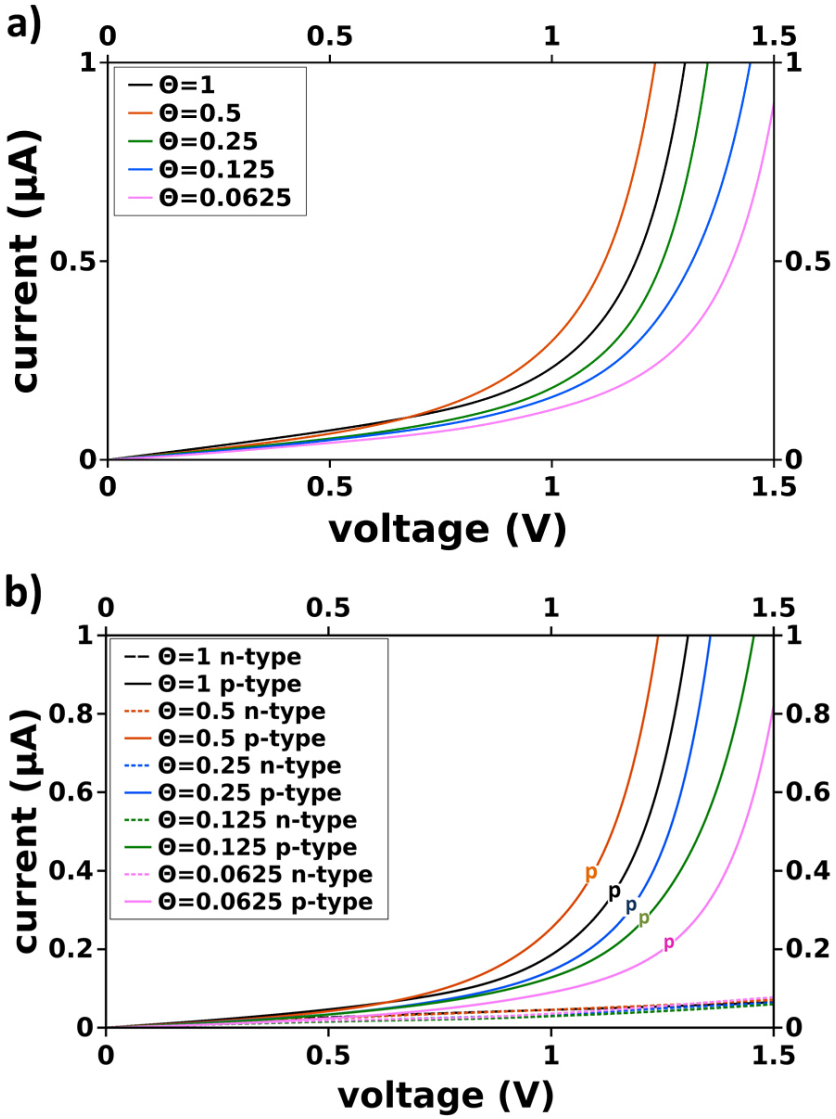

Figure 53: (a)Voltage dependent current per molecule for N_{in} junctions of different coverages Θ; (b) corresponding n-type and p-type currents per molecule

It has to be mentioned that the current in all DFT based methods is found to be significantly overestimated compared to experiments, due to the wrong level alignment found within the DFT framework, leading to a too smaller bandgap, and therefore too high current densities are achieved. For example, Quek et al. [109] tried to quantitatively understand the conductance of single-molecule benzenediamine-gold junctions in a combined theoretical and experimental investigation. They found the average calculated conductance to be seven times larger than in experiment, and explained the discrepancy quantitatively in terms of electron correlation effects impacting the molecular level alignments in the junction.

A very successful approach to correct for this self-interaction error, at least for weakly coupled systems, was persued by J. Neaton et al. [110] by cleverly renormalizing the molecular electronic levels at the metal-molecule interfaces. This electron self-energy correction to the molecular orbital energies consists of two parts: (i) a 'molecular' term correcting for the difference between DFT HOMO and LUMO energies and IP and EA of the gas phase, and second (ii) an 'image charge' term accounting for the effect of electrode polarization. In [111] Quek et al. investigated the length dependence of conductance in aromatic single-molecule junctions. They showed that DFT + Σ brings both conductance and the length dependency into nice agreement with measurements, while normal DFT only correctly describes the exponential decay of conductance with length. Using self-energy-corrected DFT together with a coherent scattering approach Darancet et al. recently found excellent agreement with experiments at finite bias for pyridine-Au and amine-Au linked molecular junctions [112].

Since in this thesis, absolute values for the current are not that important, as only relative energies are needed to describe collective electrostatic effects, standard DFT is a sufficient description.

7 Impact of coverage for molecules with different docking groups

Since docking groups were found to have a strong impact on charge transport characteristics, as reported in section 1.3, molecules with different anchor groups forming the contact between the organic part and the electrodes shall be investigated in this chapter. After analyzing the effect of different docking groups on the electronic properties of full monolayer junctions on the basis of VASP and SIESTA, coverage-dependent effects will be studied in a similar way as it was done in the previous section. Transmission functions and (I-V)-characteristics will be obtained from $\text{SIESTA}_{\text{TS}}$ as a function of coverage.

7.1 Full coverage junctions

Bevor investigating collective electrostatic effects established in molecular junctions with different docking groups, properties of the full monolayer junctions (2×2 unit cell with 11.81 Å^2) comprising the molecules $\text{Tour}_{\text{CH}_2\text{SH}}$, Tour_{SH}, Tour_{NC} and Tour_{Pyr} (Fig. 54) shall be analyzed on the basis of VASP and $\text{SIESTA}_{\text{TS}}$ results.

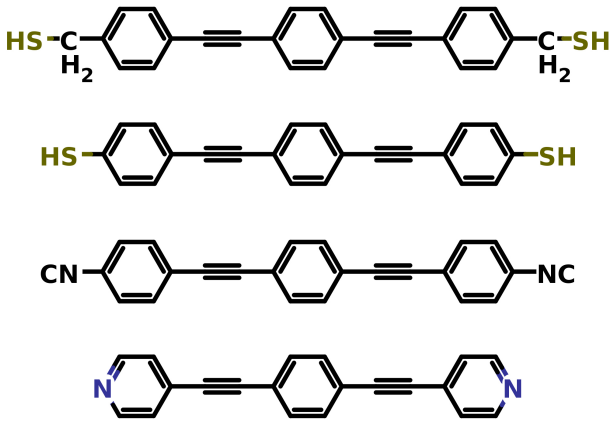

Figure 54: Chemical structures of $\text{Tour}_{\text{CH}_2\text{SH}}$, Tour_{SH}, Tour_{NC} and Tour_{Pyr}

7.1.1 Docking Groups and Level Alignment

Docking groups were shown to have tremendous effects on the level alignment in molecular junctions, as was elaborately discussed in the introduction (section 1.3). Fig. 55 shows the density of states projected onto the molecular part (PDOS) for the different systems for full coverage $\Theta = 1$ obtained from VASP. The line-up of the frontier molecular orbitals with the metal E_F is greatly influenced by changing the anchoring group. While there is only a small difference when removing the methylene (CH_2SH) spacer, reflected in the broadening of the two sharp peaks for $\text{Tour}_{\text{CH}_2\text{SH}}$ into a composition for Tour_{SH}, there are enormous shifts to lower energies of HOTC and LUTC for the isocyanide and pyridine

anchor group.

As can be seen in Fig. 55, the identification of the highest occupied transmission channel HOTC the lowest unoccupied transmission channel LUTC, is not always that clear, especially for the HOTC of $Tour_{SH}$ and the LUTC of $Tour_{NC}$. To find the right states I followed the procedure carried out in in section 6.1 for the example of N_{out}. At first the local density of states LDOS was obtained by integrating the PDOS in steps of 0.1 eV in the interesting energy regions. Additionally, a python script called `interpolation_and_integration` written by Bernhard Kretz, was used to find the energy intervals, in between two electronic states (one spin up and one spin down) are defined. The vertical, black lines in Fig. 55 indicate the corresponding energy intervals. Table 5 summarizes the positions of the HOTC and LUTC energies with respect to the metal E_F, ΔE_{HOTC} and ΔE_{LUTC} respectively for full coverage $\Theta = 1$.

Table 5: Level alignment ΔE_{HOTC} and ΔE_{LUTC} , defined as the energy difference between HOTC and LUTC with the metal E_F, for the systems with different docking groups for full coverage $\mathbf{\Theta = 1}$

Systems	$\Delta E_{HOTC}{}^{\Theta=1}$/eV	$\Delta E_{LUTC}{}^{\Theta=1}$/eV
$Tour_{CH_2SH}$	-0.80	1.55
$Tour_{SH}$	-0.68	1.53
$Tour_{NC}$	-1.40	0.68
$Tour_{Pyr}$	-2.15	0.17

The HOTC and LUTC come to lie highest with respect to E_F for the -SH (CH_2SH) docking groups, they are at intermediate positions for -NC and lowest for -Pyr; the choice of the anchor group, thus, permits the possibility to tune the level alignment over a range of > 1 eV. The special alignment of the LUTC of $Tour_{Pyr}$, due to an effect called *Fermi-level pinning* [51], [113], will be discussed in detail in section 7.3.

A comparison to the results obtained from SIESTA, as it was done for N_{in} and N_{out} in section 6.2.1, is shown in Fig. 56 for the the full monolayer junctions with different docking groups. A nice agreement can be, again, found for $\Theta = 1$ when adapting the same settings as in section 6.2.1 (with a crucial parameter being the `PAO.EnergyShift`).

7.1.2 Current-Voltage-Characteristics

The difference in the level alignment, originating from different anchor groups binding the molecules to the electrodes, is, of course, reflected in the corresponding transport characteristics. Fig. 57 shows the current of all molecular junctions for $\Theta = 1$, calculated with $SIESTA_{TS}$. Again, for the sake of comparison the results obtained from TRANSIESTA are indicated as dashed lines. The differences between the codes are basically stemming from the fact, that there are three layers of gold on each side of the central region used in $SIESTA_{TS}$, while there had to be six layers deployed to achieve convergence for TRANSIESTA. Adapting the number of layers used in the central region leads to a nice agreement

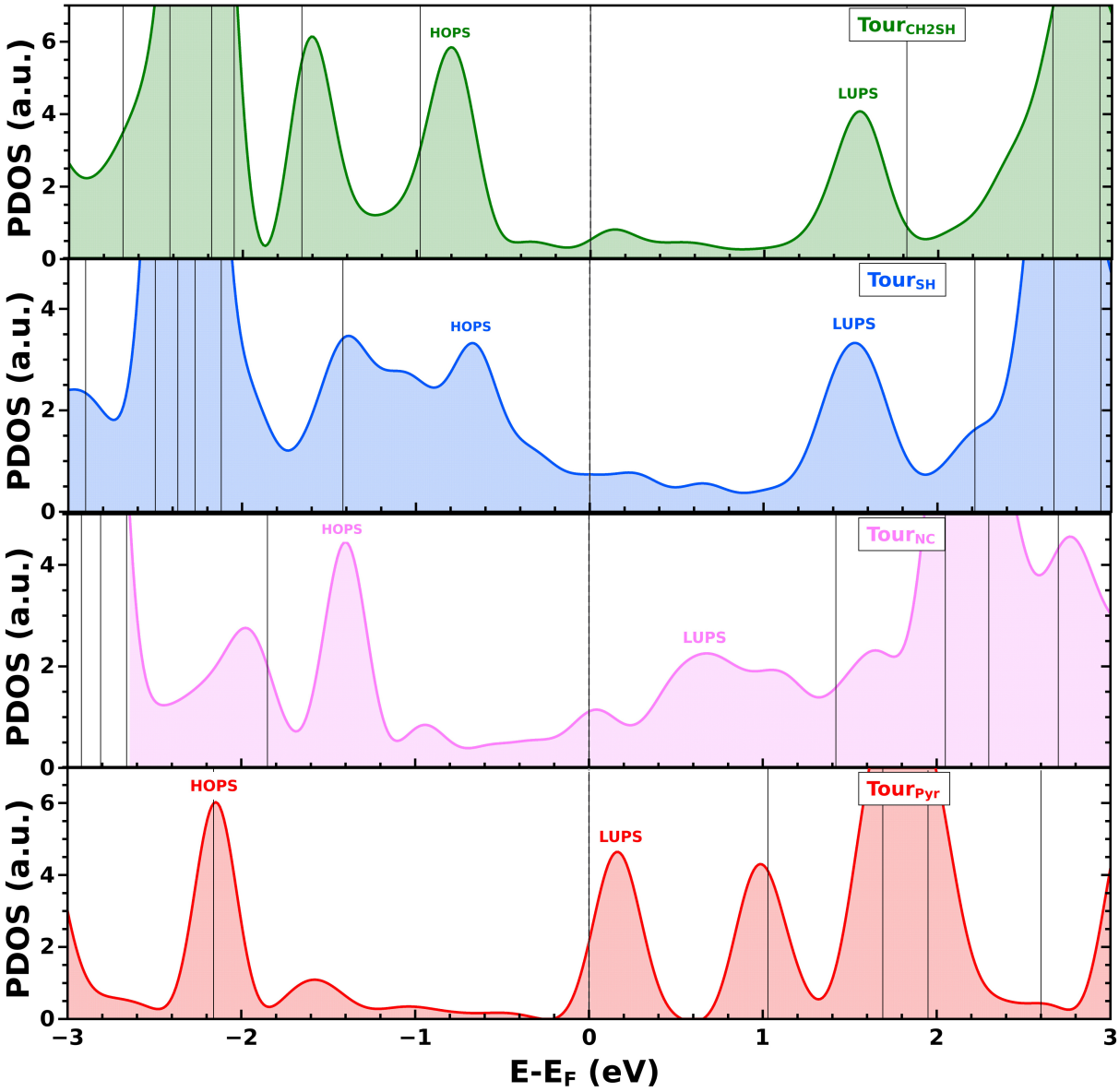

Figure 55: Density of states projected onto the molecular part (PDOS) for full coverage $\Theta = 1$ for different docking groups -CH_2SH, -SH, -CN, -Pyr (from top to bottom) calculated with VASP; HOTC and LUTC peaks are marked after deriving the corresponding isodensity plots of the LDOS; black, vertical lines indicate the intervals, in between which two states are found.

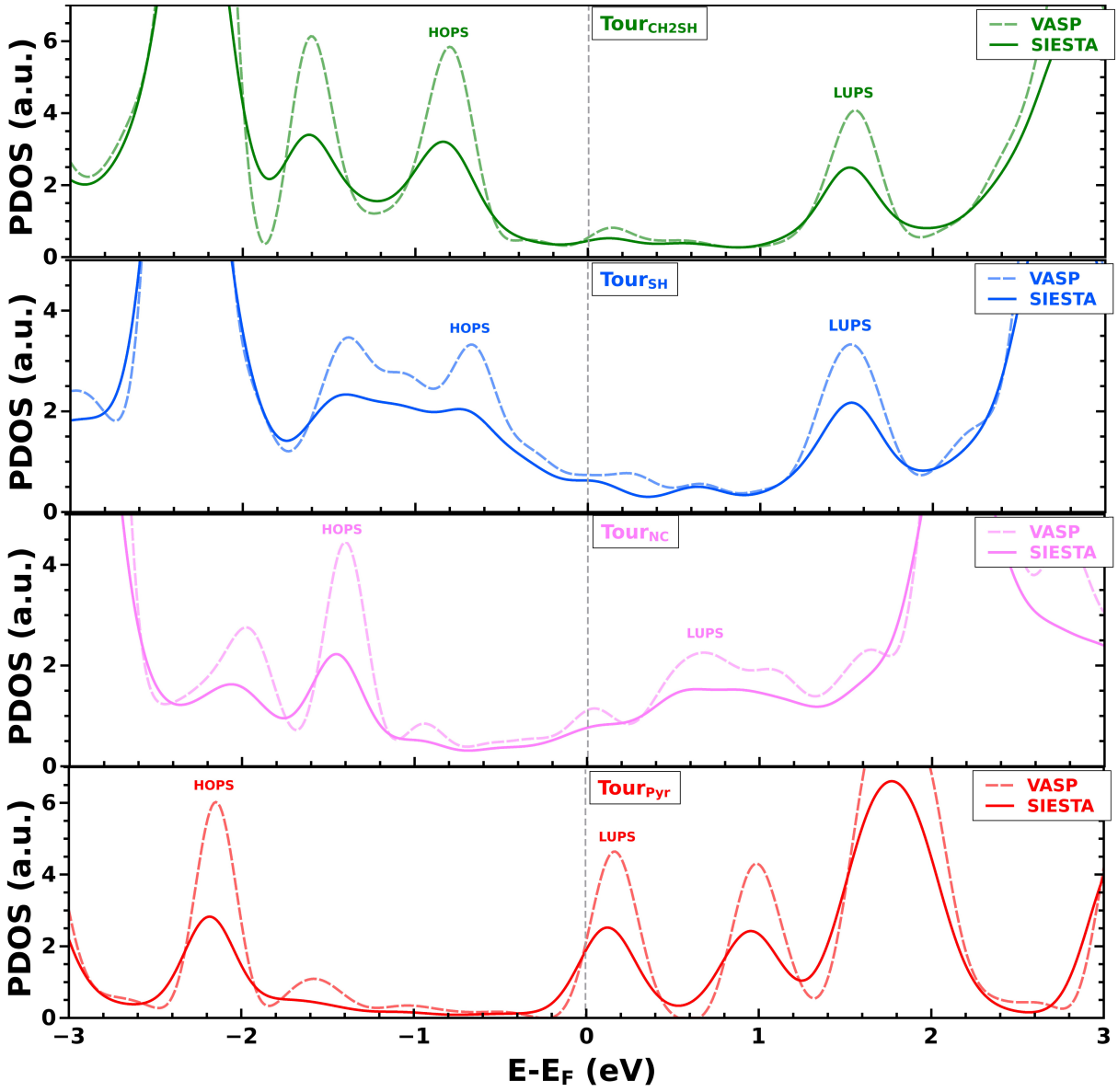

Figure 56: Density of states projected onto the molecular part (PDOS) for full coverage $\Theta = 1$ for different docking groups -CH_2SH, -SH, -CN, -Pyr (from top to bottom) calculated with VASP and SIESTA.

between the codes as was shown for N_{in} and N_{out} in section 6.2.2.

An enormous difference in the (I-V) curves for full monolayer devices can be found, when changing the docking groups. Compared to N_{in} and N_{out}, there is a lower current per molecule for $Tour_{CH_2SH}$. For the -SH and especially for the -NC docking group, a vast increase in current per molecule up to several μA can be found. Note, that these results only hold in the low-bias regime and again the special case of Fermi-level pinning for the -PYR anchor group leads to a saturation of the current within this description (see section 7.3).

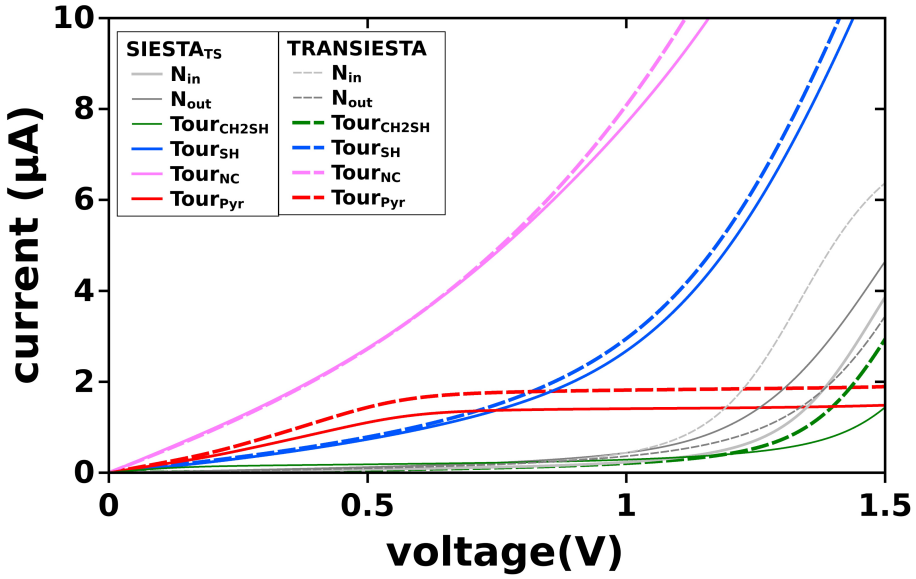

Figure 57: Current-voltage characteristics for full coverage $Tour_{CH_2SH}$, $Tour_{SH}$, $Tour_{NC}$ and $Tour_{Pyr}$ junctions, obtained from SIESTA$_{TS}$, as well as TRANSIESTA with small differences mainly stemming from the different number of gold layers used in the centralregion calculation for the different codes. N_{in} and N_{out} results are indicated as grey lines.

7.2 Coverage-dependent Effects

Collective electrostatic effects shall now be investigated also for $Tour_{CH_2SH}$, $Tour_{SH}$, $Tour_{NC}$ and $Tour_{Pyr}$ junctions of different coverages in a way similar to what was done in section 6.1. It was shown, that N_{in} and N_{out} molecular junctions have very different transport characteristics when assembled in a full monolayer device, but reducing the coverage led to a more and more similar situation. When lowering the molecular junctions with different docking groups, the tremendous differences originating from collective effects in the full monolayer devices mentioned in the last section are expected to reduce to the respective differences in the IP and EA and the bond dipole for the corresponding single molecule junctions.

Fig. 58a - d illustrate the PDOS of all systems with different docking groups as a function of coverage obtained from VASP. Bevore discussing the pronounced differences found in

these coverage-dependent PDOSs, a comparison to the results obained from SIESTA shall be done, since these are the quantities entering the transport calculations. Fig. 58a - d show the same coverage-dependent curves, on the one hand calculated with VASP and, on the other hand, obtained from SIESTA with the same settings as for N_{in} and N_{out} (section 6.2.1) that provided the best agrreement with VASP. The localized basis sets used in SIESTA, again, cannot describe the situation for lower coverages correctly, leading to pronounced energy differences in the HOTC and LUTC peaks > 0.1 eV for lowest coverage, $\Theta = 0.0625$. As a consequence, the investigated collective effects are sligthly reduced in all further transport calculations obtained from SIESTA.

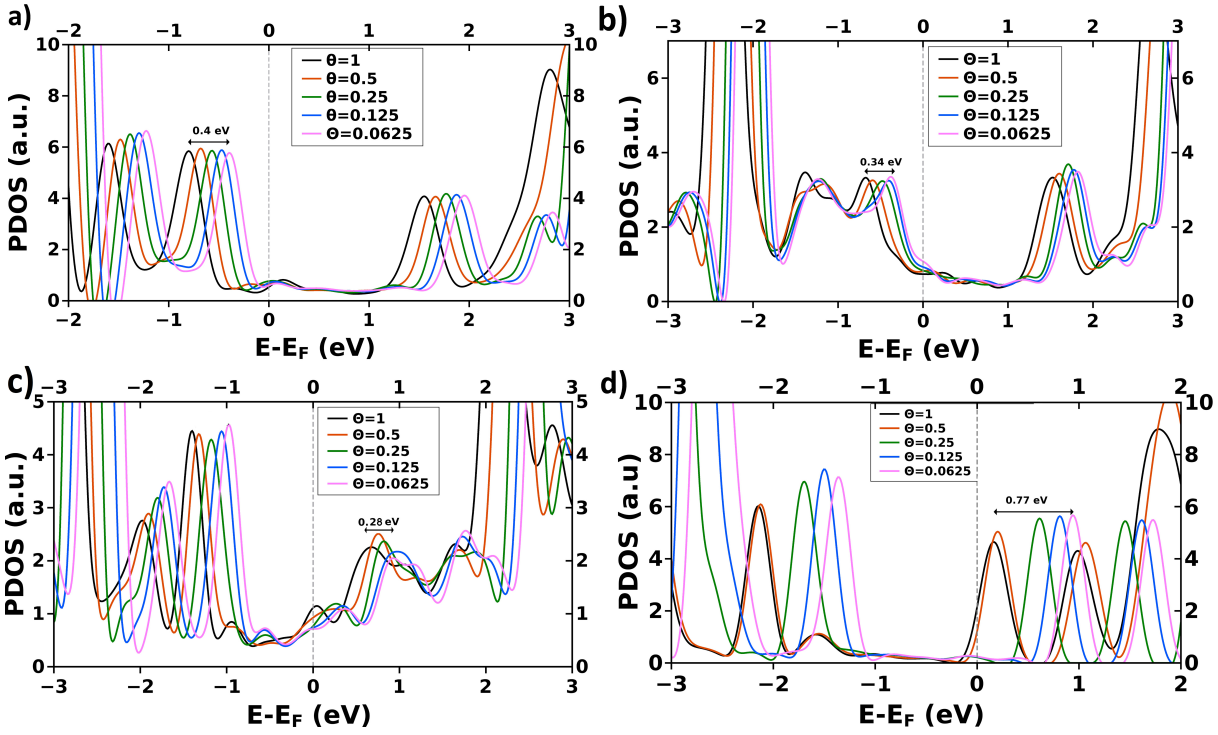

Figure 58: Coverage dependent PDOS of molecular junctions with different docking groups: (a) $Tour_{CH_2SH}$, (b) $Tour_{SH}$, (c) $Tour_{NC}$, (d) $Tour_{Pyr}$ for different coverages Θ, obtained from VASP.

The corresponding HOTC and LUTC energies derived from the peaks of Fig. 58a - d are summarized in Fig. 60a and b for all molecular junctions. Depending on coverage, Θ, the HOTC and LUTC peaks are aligned with respect to the HOTC and LUTC energies for full coverage $E_{HOTC}{}^{\Theta=1}$ and $E_{LUTC}{}^{\Theta=1}$. From these plots one can easily retrace the pronounced differences in the coverage-dependent trends for the investigated systems. Compared to all other systems, the N_{in} molecular junction (black circles) stands out with an almost vanishing coverage-dependent effect. Also unusual is the $Tour_{Pyr}$ system, showing a very strong shift when going to lower coverages with a pronounced kink at $\Theta = 0.5$. All other systems $Tour_{SH}$, $Tour_{CH_2SH}$, $Tour_{NC}$ and N_{out} exhibit collective effects that lie somewhere between the former systems.

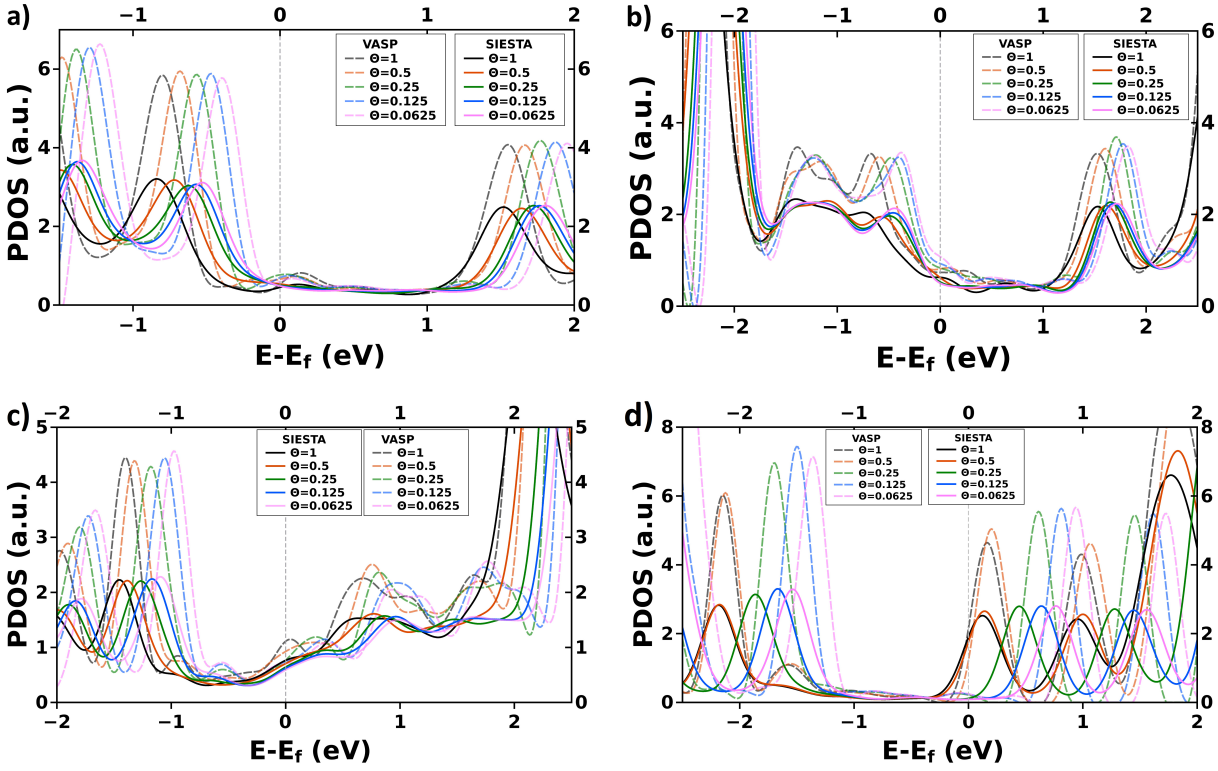

Figure 59: Coverage dependent PDOS of molecular junctions with different docking groups: (a) $\text{Tour}_{\text{CH}_2\text{SH}}$, (b) Tour_{SH}, (c) Tour_{NC}, (d) Tour_{Pyr} for different coverages Θ, obtained from VASP and SIESTA.

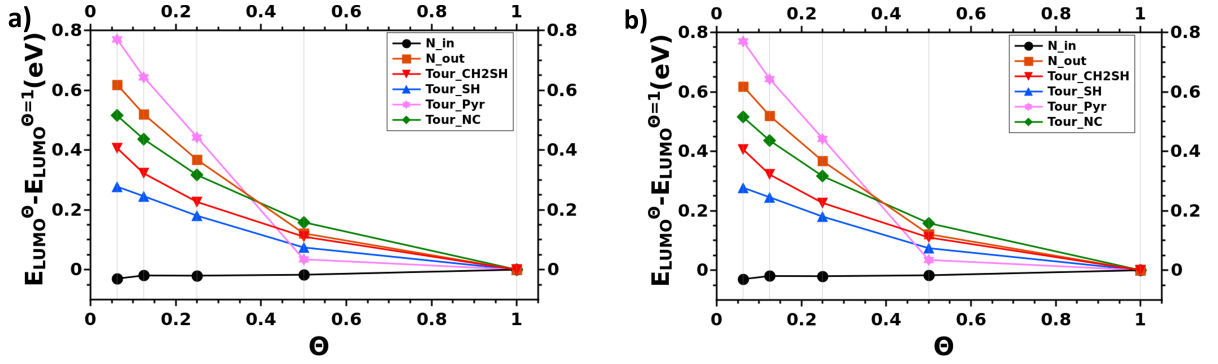

Figure 60: Coverage dependent energy shifts ΔE_{HOTC} and ΔE_{LUTC} for all investigated systems. HOTC and LUTC energies, obtained from the peaks of the corresponding PDOS are aligned with respect to the energies for full coverage $E_{HOTC}^{\Theta=1}$ and $E_{LUTC}^{\Theta=1}$ respectively.

Table 6: Level alignment ΔE_{HOTC} and ΔE_{LUTC} for coverage $\mathbf{\Theta = 0.5}$

Systems	$\Delta E_{HOTC}{}^{\Theta=0.5}$/eV	$\Delta E_{LUTC}{}^{\Theta=0.5}$/eV
$Tour_{CH_2SH}$	-0.68	1.66
$Tour_{SH}$	-0.59	1.60
$Tour_{NC}$	-1.32	0.75
$Tour_{Pyr}$	-2.12	0.20

Table 7: Level alignment ΔE_{HOTC} and ΔE_{LUTC} for coverage $\mathbf{\Theta = 0.25}$

Systems	$\Delta E_{HOTC}{}^{\Theta=0.25}$/eV	$\Delta E_{LUTC}{}^{\Theta=0.25}$/eV
$Tour_{CH_2SH}$	-0.65	1.78
$Tour_{SH}$	-0.47	1.71
$Tour_{NC}$	-1.18	0.82
$Tour_{Pyr}$	-1.69	0.61

7.2.1 Origin of Collective Effects

In anaolgy to section 6.1, a detailed description of the collective electrostatic effects shall be given. This will be based on a seperation of the effects into the ones arising from metal-molecule bonding and the ones coming from the properties of individual molecules, respectively, free standing monolayers.

The corresponding HOTC and LUTC energies derived from the peaks of the PDOS of the metal-molecule-metal systems, shown in Fig. 58, are summarized in tables 5 (page 85), 6, 7, 8 and 9 for $\Theta = 1$, $\Theta = 0.5$, $\Theta = 0.25$, $\Theta = 0.125$ and $\Theta = 0.0625$ respectively. Every system shows a pronounced shift to higher energies when going from full monolayer $\Theta = 1$ to a single molecule junction at $\Theta = 0.0625$, similar to the N_{out} junction. None of them reflects the situation observed for N_{in}, where the combined interaction of local dipoles and bond dipole led to a disappearing coverage effect.

Taking a closer look at the shifts in the PDOS, the first collective effect, namely the jump in the electrostatic potential energy due to metal-bond formation reflected in the bond dipole, shall be investigated as a function of coverage for all systems with different docking groups. The coverage-dependent bond dipole, Δ_{BD}, is shown in Fig. 61a-d for all systems. $Tour_{CH_2SH}$ adopts an intermediate situation between N_{in} and N_{out}, reflected in

Table 8: Level alignment ΔE_{HOTC} and ΔE_{LUTC} for coverage $\mathbf{\Theta = 0.125}$

Systems	$\Delta E_{HOTC}{}^{\Theta=0.125}$/eV	$\Delta E_{LUTC}{}^{\Theta=0.125}$/eV
$Tour_{CH_2SH}$	-0.47	1.87
$Tour_{SH}$	-0.41	1.77
$Tour_{NC}$	-1.06	0.97
$Tour_{Pyr}$	-1.50	0.81

Table 9: Level alignment ΔE_{HOTC} and ΔE_{LUTC} for coverage $\mathbf{\Theta = 0.0625}$

Systems	$\Delta E_{HOTC}^{\Theta=0.0625}$/eV	$\Delta E_{LUTC}^{\Theta=0.0625}$/eV
$Tour_{CH_2SH}$	-0.40	1.96
$Tour_{SH}$	-0.38	1.82
$Tour_{NC}$	-0.98	0.93
$Tour_{Pyr}$	-1.37	0.94

a bond dipole that is -1.04 eV at full coverage that reduces to -0.19 eV for low coverages (δE_{BD}= 0.85 eV). While the jump in electrostatic potential energy is very localized to the metal-molecule interface for the reference system, it is a slightly more extended into the backbone for the $Tour_{SH}$ molecular junction with a shift of δE_{BD}=0.79 eV when going from full to lowest coverage. This is a consequence of a slightly more extended charge transfer into the molecular backobone for $Tour_{SH}$. A different behaviour is found for $Tour_{NC}$. With a bond dipole of about +1 eV for full coverage, it is the only system with a positive bond dipole, and, therefore, a negative coverage effect concerning bond formation (δE_{BD}= -0.86 eV). This behaviour is in agreement with many works [35], [49] and can be reflected in the electron withdrawing property of the strong accepting -NC docking group, while thiol docking groups exhibit an electron donating character [49]. A special situation occurs again for the pyridine docking group, where there is a remarkable reduction of the bond dipole for full coverage in the middle of the backbone. Therefore, δE_{BD} is nominally reduced here to 0.10 eV.

The second collective effect coming from the assembly of local dipoles of the free-standing monolayers of different densities is illustrated in Fig. 62. The plots show the HOMO (a) and LUMO (b) energies aligned to the vacuum level E_{VAC} of the free standing monolayers for different molecular densities Θ. $Tour_{CH_2SH}$ and $Tour_{SH}$ are found to shift very little with coverage (about $0.1 - 0.3$ eV), whereas $Tour_{Pyr}$ and especially $Tour_{NC}$ show tremendous shifts for different molecular densities (about $1 - 2$ eV).

As discussed in section 6.1, the shifts in the molecular junction PDOS, δE_{HOTC} and δE_{LUTC}, when going from full coverage to lowest coverage can be partitioned into contributions coming from the free monolayer (δE_{HOMO} and δE_{LUMO}) and contributions coming from the metal-molecule bond formations, reflected in the jump of the corresponding electrostatic potential (δE_{BD}). The equations are reprinted, according to Eq. 6.1a and 6.1b from section 6.1

$$\delta E_{HOPS} = \delta E_{HOMO} + \delta E_{BD} + 2\delta E_{corr}^{HOMO} \tag{6.1a}$$

$$\delta E_{LUPS} = \delta E_{LUMO} + \delta E_{BD} + 2\delta E_{corr}^{LUMO} \tag{6.1b}$$

Again, small correction terms have to be introduced, accounting for (i) the shifts of the eigenenergies of the SAM resulting from changes in the molecular potential due to the bonding-induced charge rearrangements and (ii) potential inhomogenieties for different coverages. δE_{HOTC} and δE_{LUTC} are taken from the peaks of the PDOS plots in Fig. 58a-d, δE_{HOMO} and δE_{LUMO} from the peaks of the corresponding DOS of the free standing monolayer (Fig. 62a-d) and the bond dipoles difference δE_{BD} is taken from Fig. 61a-d.

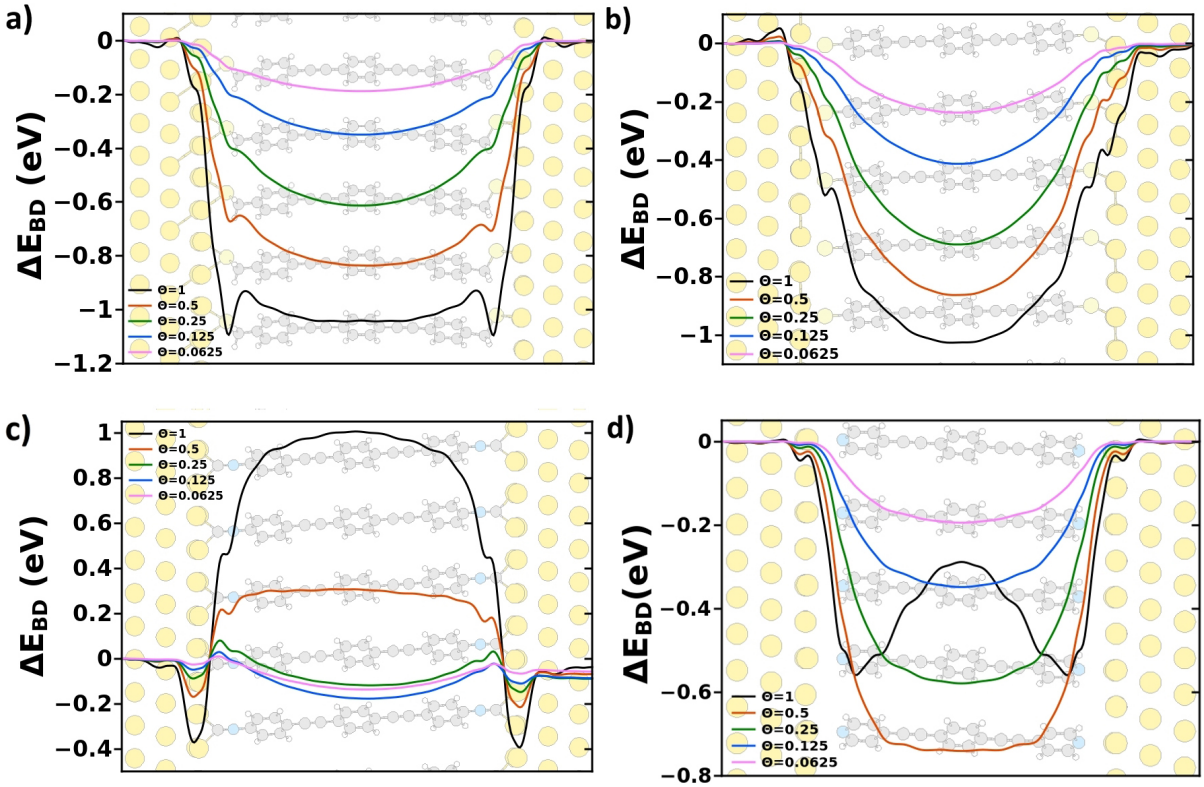

Figure 61: Coverage dependent bond dipole ΔE_{BD} of molecular junctions with different docking groups: (a) $\text{Tour}_{\text{CH}_2\text{SH}}$, (b) Tour_{SH}, (c) Tour_{NC}, (d) Tour_{Pyr} for different coverages Θ

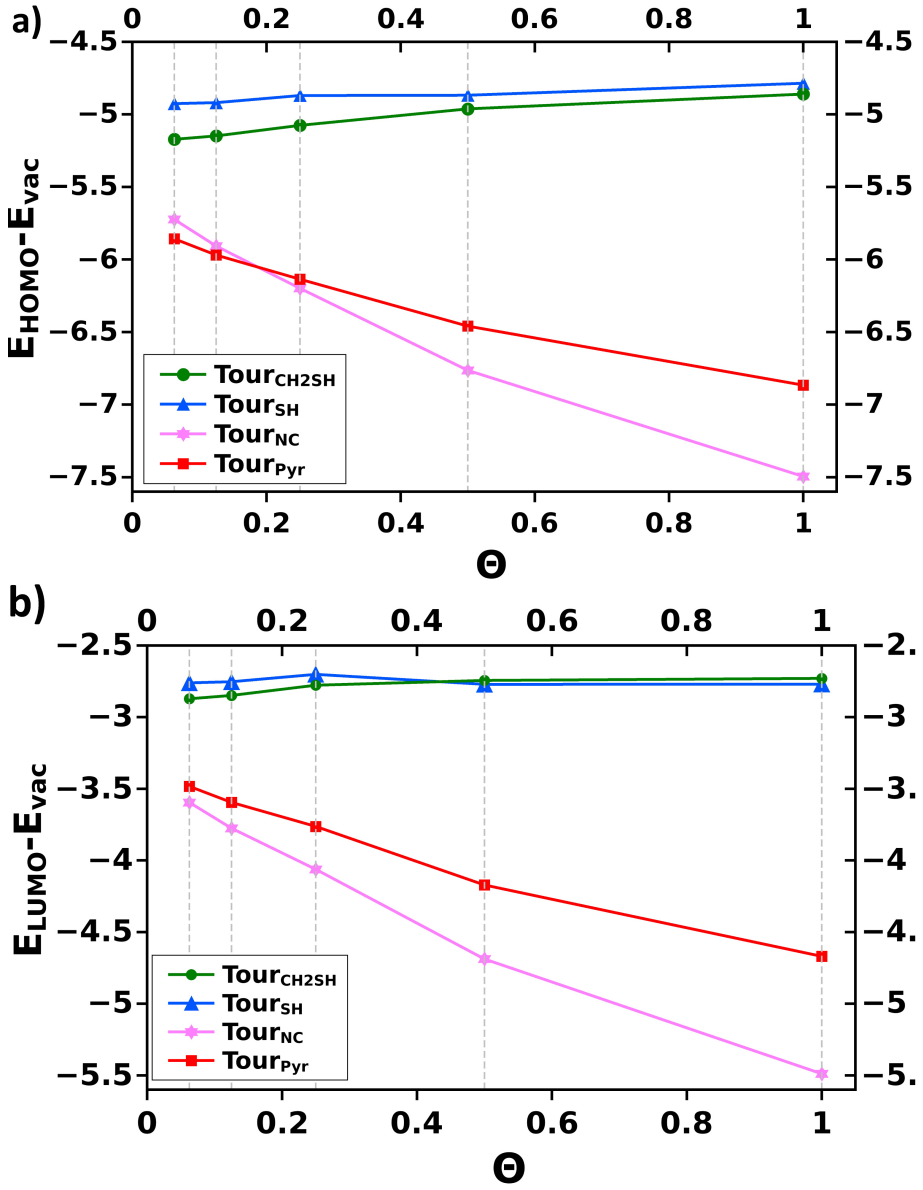

Figure 62: Coverage dependent energy shifts ΔE_{HOMO} (a) and ΔE_{LUMO} (b) for the systems with different docking groups. HOMO and LUMO energies are obtained from the peaks of the corresponding coverage dependent DOS and the vacuum level E_{VAC} can be obtained from the corresponding plane averaged potential.

Table 10: Parameters characterising collective effects in $Tour_{CH_2SH}$, $Tour_{SH}$, $Tour_{NC}$ and $Tour_{Pyr}$ molecular junctions of different densities according to Eq. 6.1a and 6.1b: $\delta E_{HOTC}/\delta E_{LUTC}$ are the differences in the HOTC/LUTC energies between full monolayer and single molecule junctions. $\delta E_{HOMO}/\delta E_{LUMO}$ are the differences in the HOMO/LUMO energies between the corresponding free full monolayer and single molecule. δE_{BD} reflects the energy difference of the bond dipole upon charge rearrangements between full coverage and lowest coverage. δE_{corr}^{HOMO}, δE_{corr}^{LUMO} are correction energies.

Systems	δE_{HOTC}/eV	δE_{HOMO}/eV	δE_{BD}/eV	δE_{corr}^{HOMO}/eV
$Tour_{CH_2SH}$	0.40	-0.27	0.85	-0.09
$Tour_{SH}$	0.30	-0.10	0.79	-0.19
$Tour_{NC}$	0.42	1.81	-0.86	-0.26
$Tour_{Pyr}$	0.78	1.01	0.10	-0.16
Systems	δE_{LUTC} /eV	δE_{LUMO}/eV	δE_{BD}/eV	δE_{corr}^{LUMO}/eV
$Tour_{CH_2SH}$	0.41	-0.28	0.85	-0.08
$Tour_{SH}$	0.29	-0.10	0.79	-0.20
$Tour_{NC}$	0.28	1.78	-0.86	-0.32
$Tour_{Pyr}$	0.77	1.06	0.10	-0.19

Table 10 summarizes the results.

The correction energies are found to be very small for extended docking group like the -CH_2SH and rise significantly, when switching to docking groups that are stronger coupled. This was also found in [35]. While they are in the range of 0.1 eV for the -CH_2SH anchor group, they get very high for the -NC docking group. The larger value for $Tour_{NC}$ is, in part, also due to the difficult determination of the LUTC position, as can be seen in Fig. 58.

In section 6 it was described in detail that the ismoeric N_{in} and N_{out} systems were seen to become almost equal when lowering the coverage in the respective molecular junctions, since they have a very similar IP. Now, the systems with different docking groups are investigated. They are expected not to become equal as single molecule junctions, but to result in differences only according to their various molecular IP and EA and the remaining bond dipole.

As expressed in Eq. 7.2a and 7.2b, the energy difference of the level alignment of the HOTC and LUTC with the Fermi level at lowest coverage, $\Delta E_{HOTC}{}^{\Theta=0.0625}$ and $\Delta E_{LUTC}{}^{\Theta=0.0625}$, should be reflected in contributions coming from the corresponding alignment as a free standing single molecule (approximated by IP and EA), and from the remaining bond dipole at lowest coverage, $E_{BD}{}^{\Theta=0.0625}$.

$$\Delta E_{HOTC}{}^{\Theta=0.0625} = IP + E_{BD}{}^{\Theta=0.0625} + 2E_{corr}{}_{HOMO}^{\Theta=0.0625} \tag{7.2a}$$

$$\Delta E_{LUTC}{}^{\Theta=0.0625} = EA + E_{BD}{}^{\Theta=0.0625} + 2E_{corr}{}_{LUMO}^{\Theta=0.0625} \tag{7.2b}$$

Table 11: Quantities described in Eq. 7.2a and 7.2b. $\Delta E_{HOTC}{}^{\Theta=0.0625}$ and $\Delta E_{LUTC}{}^{\Theta=0.0625}$ are the energy shifts of the HOTC and LUTC with respect to Fermi energy for the molecular junction systems at lowest coverage. $IP^{\Theta=0.0625}$ and $EA^{\Theta=0.0625}$ are . Differences are investigated with respect to the reference system. IPs and EAs are taken from table 3, whereas $\Delta E_{HOPS}{}^{\Theta=0.0625}$ and $\Delta E_{LUPS}{}^{\Theta=0.0625}$ are calculated from the respective values summarized in table 9.

Systems	IP/eV	$\Delta E_{HOTC}{}^{\Theta=0.0625}$/eV	$E_{BD}{}^{\Theta=0.0625}$/eV	$E_{corr\,HOMO}^{\Theta=0.0625}$/eV
$Tour_{CH_2SH}$	-0.15	-0.40	-0.19	-0.03
$Tour_{SH}$	-0.15	-0.38	-0.24	0.05
$Tour_{NC}$	-0.28	-0.98	-0.13	-0.35
$Tour_{Pyr}$	-0.15	-1.37	-0.19	-0.52
Systems	EA/eV	$\Delta E_{LUTC}{}^{\Theta=0.0625}$/eV	$E_{BD}{}^{\Theta=0.0625}$/eV	$E_{corr\,LUMO}^{\Theta=0.0625}$/eV
$Tour_{CH_2SH}$	2.11	1.96	-0.19	0.02
$Tour_{SH}$	1.98	1.82	-0.24	0.04
$Tour_{NC}$	1.95	0.93	-0.13	-0.45
$Tour_{Pyr}$	2.22	0.94	-0.19	-0.55

IPs and EAs are approximated by the HOMO and LUMO energies aligned to the Fermi level at lowest coverage. $\Delta E_{HOTC}{}^{\Theta=0.0625}$ and $\Delta E_{LUTC}{}^{\Theta=0.0625}$ are taken from the peaks of the corresponding PDOS and $E_{BD}{}^{\Theta=0.0625}$ is taken from Fig. 61. The respective values are summarized in table 11. Again, correction terms have to be added.

For $Tour_{CH_2SH}$ and $Tour_{SH}$ the situation is very well described and the correction terms are really small (< 0.1 eV). So reducing the coverage in these systems results only in differences coming from their different IP/EA and the remaining bond dipole is very small ($0.1 - 0.2$ eV). For $Tour_{NC}$ and $Tour_{Pyr}$ there are tremendous correction effects, but the remaining bond dipole is similar to the values of the other systems. For these systems further investigations need to be done.

7.2.2 Transport Calculations

Applying $SIESTA_{TS}$ coverage-dependent charge transport properties of all molecular junctions with different docking groups were obtained. The corresponding transmission functions are shown in Fig. 63a-d and Fig. 64a-d contains the respective current-voltage curves, obtained according to the Landauer formula.

In comparison to N_{in} and N_{out}, the reference system $Tour_{CH_2SH}$ has exactly the same docking group, but of course a different IP and EA. Its coverage dependent transmission functions can be found in Fig. 63a. In accordance with the corresponding PDOS there is a shift of 0.3 eV to positive energies when going from full monolyayer to single molecule junctions. Since the HOTC is in this case closer to the metal E_F, charge transport through unoccupied states is expected. Altogether $Tour_{CH_2SH}$ represents a new situation.

In comparison to N_{out}, the peaks in the shift PDOS into the same direction, but transport is HOMO instead of LUMO dominated. N_{in} and $Tour_{CH_2SH}$ exhibit opposite energetic trends, but are both HOMO dominated. Reducing the coverage for the reference system, shifts the crucial transport channel closer and closer to the Fermi energy, resulting in a curent per molecule, that is expected to increase with decreasing coverage. Indeed, this is the case for $Tour_{CH_2SH}$, as can be seen in Fig. 64 a in the low-bias current-per molecule. This is a new kind of (I-V) behaviour compared to N_{out}, where the current was found to decrease with decreasing coverage, and N_{in}, where a relatively small coverage effect was obtained.

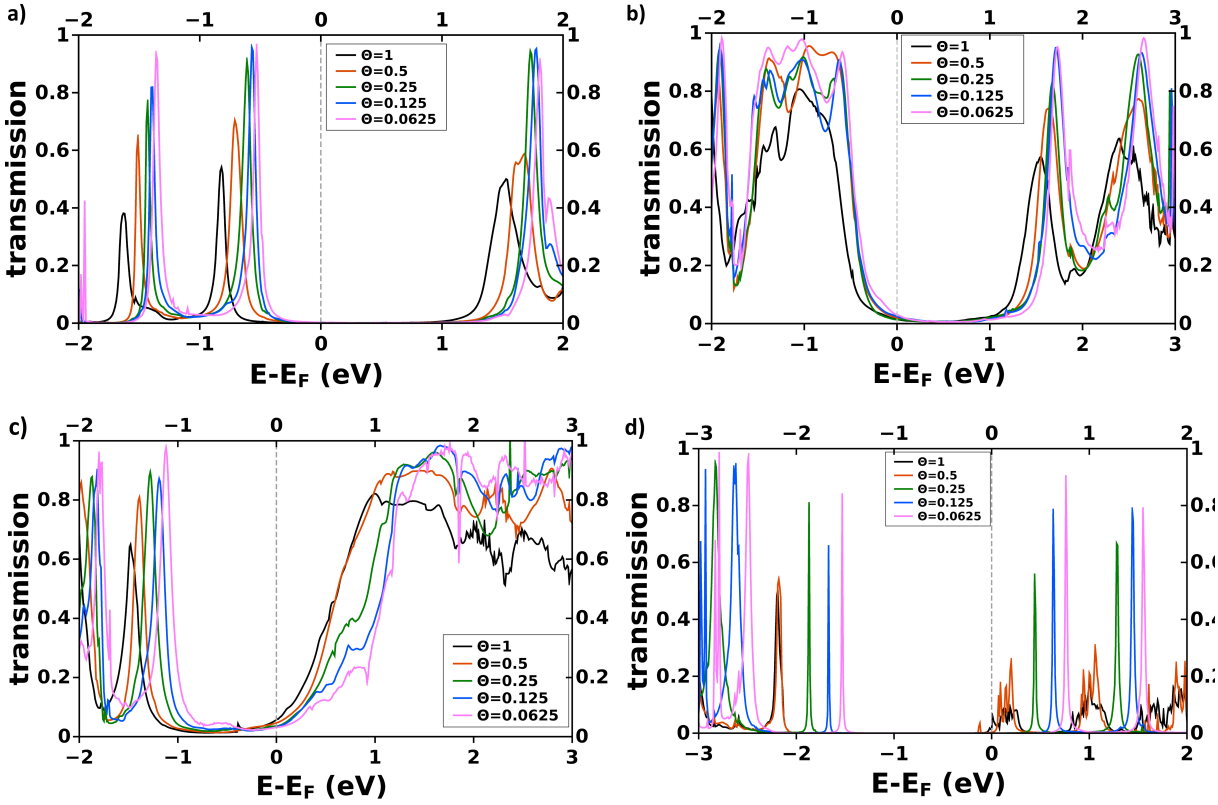

Figure 63: Coverage dependent transmission functions obtained with SIESTA$_{TS}$ for (a) $Tour_{CH_2SH}$, (b) $Tour_{SH}$, (c) $Tour_{NC}$ and (d) $Tour_{Pyr}$.

Different charge transport characteristics are discovered when investigating $Tour_{SH}$ molecular junctions at different densities. As shown in Fig. 63b, there is only a slight shift to higher energies when going from $\Theta = 1$ to $\Theta = 0.0625$, resulting basically in a rising current per molecule for lower coverages (see Fig. 64b). This increase is not constant. After a pronounced step, when going from $\Theta = 1$ to $\Theta = 0.5$, the current stays nearly the same for further reduced coverages. The fact that the current corresponding to half coverage (orange line) is even slightly above the curve corresponding to $\Theta = 0.25$ (green line) is connected to the difficult determination of the HOTC states for $Tour_{SH}$. In comparison to $Tour_{CH_2SH}$, the HOTC are very much broadened, stemming from the also broadened PDOS, incorporating many states in this area. This pronounced HOTC leads to a higher current per molecule than in the case of $Tour_{CH_2SH}$.

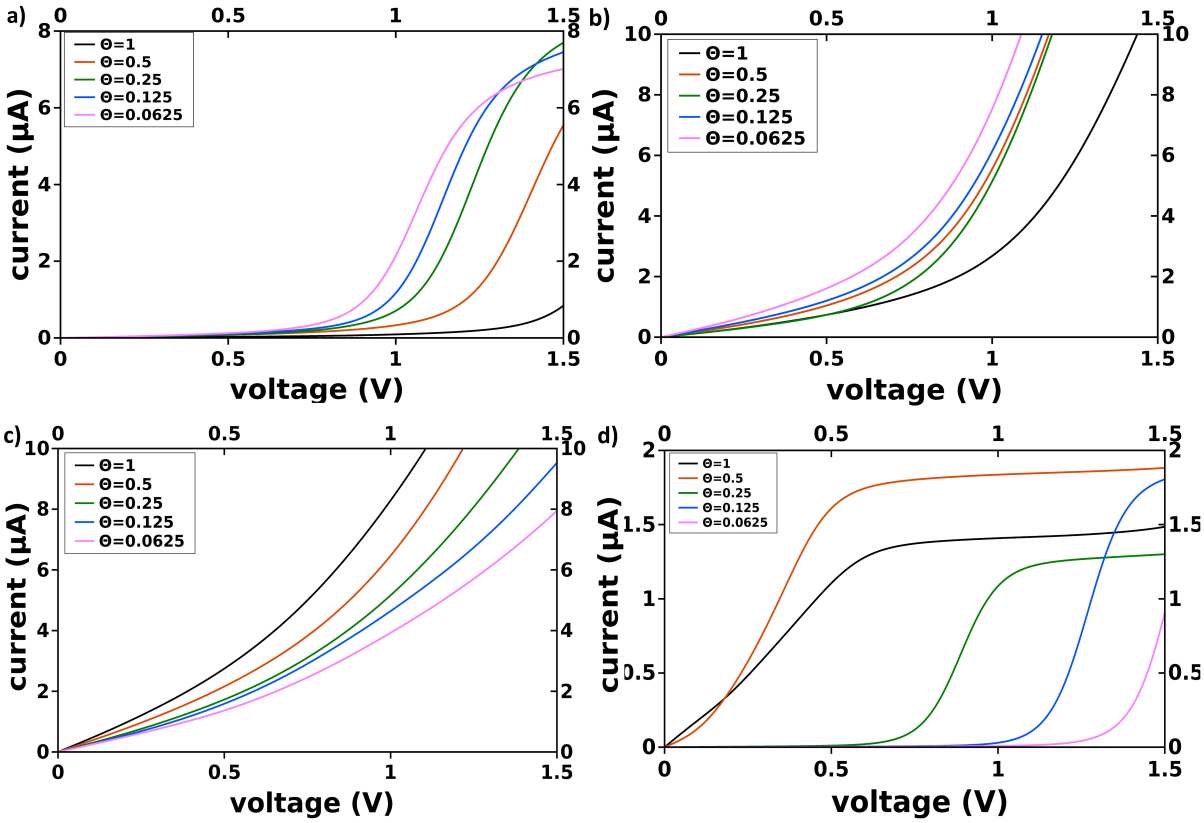

Figure 64: Voltage dependent current per molecule for $Tour_{CH_2SH}$ (a), $Tour_{SH}$ (b), $Tour_{NC}$ (c) and $Tour_{Pyr}$ (d) molecular junctions of different coverages, derived from the transmission functions via the Landauer formula

An interesting candidate, that exhibits great potential as a docking group, is $Tour_{NC}$. Compared to N_{in} and N_{out}, $Tour_{NC}$ has in fact a different docking group, but at the same time, very similar IP and EA. Fig. 63c shows a broad transmission spectrum around E_F, stemming from the fact that the metal E_F is near-resonance with the LUTC state in the PDOS, which is delocalized over the entire molecule. As can be seen from Fig. 64c this broad LUTC results in a large current per molecule for low voltages, tremendously reducing the onset voltage. Since the LUTC shifts away from E_F with decreasing coverage, there is the same trend of lower current per molecule when reducing the coverage, as was found for the N_{out} molecule. Transport is LUMO dominated for all coverages.

The special transmission function and transport characteristics of $Tour_{Pyr}$ will be discussed in the next chapter.

7.3 Fermi Level Pinning

In the case of pyridine docking to the gold electrodes, a special situation appears, as can be seen in the respective PDOS in Fig. 58d. When going from single molecule to full monolayer, collective electrostatic effects shift the states by 0.77 eV to lower energies, until the onset of the LUTC related peak is right at the Fermi energy for $\Theta = 1$ and to some extent also for $\Theta = 0.5$. This is a manifestation of the of the fact, that the system is in the regime of Fermi-level pinning [51], [35].

Fermi level pinning is found to be a consequence of interfacial charge rearrangements that, in contrast to other systems, extend along the whole molecular backbone. This can be seen in Fig. 65 that shows a comparison of the charge rearrangements $\Delta\rho$ for $Tour_{Pyr}$ (a) and the reference system $Tour_{CH_2SH}$ (b). While for the latter, $\Delta\rho$ is well localized to the interface, the charge rearrangements for the former are clearly extended. The series of dipoles introduced by these charge rearrangements readjusts the bond dipole in a way that the effective ΔE_{BD} is diminished for $\Theta = 1$, as illustrated in Fig. 61d.

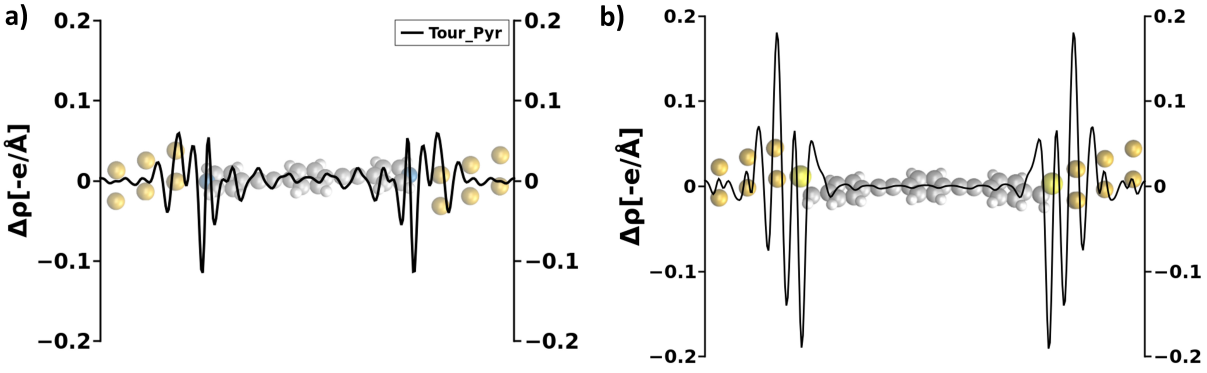

Figure 65: Charge rearrangements $\Delta\rho$ upon bond formation for (a) $Tour_{Pyr}$ and (b) compared to the reference system $Tour_{CH_2SH}$

These charge-rearrangements are not associated with long-range charge transfer, as it is

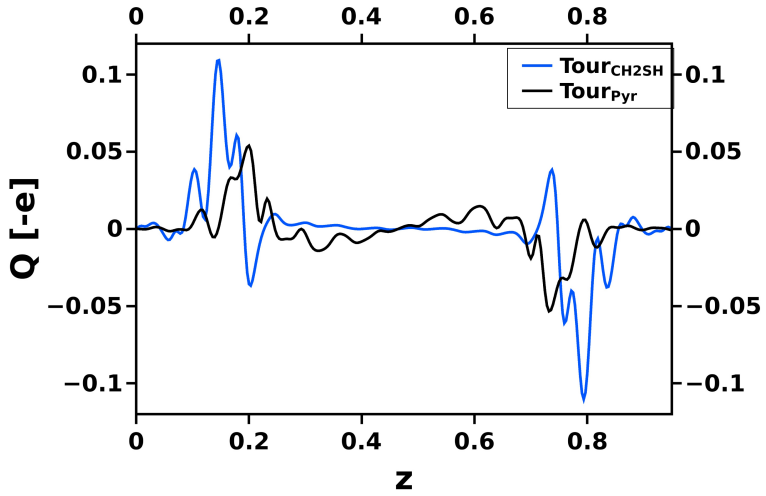

Figure 66: Charge transfer Q per molecule for Tour_{Pyr} (black line) compared to the reference system $\text{Tour}_{\text{CH}_2\text{SH}}$ (blue line).

usually found for flat-lying adsorbates [114], [115], but rather with a local polarization of the SAM as can be seen in Fig. 65 and 66 showing $\Delta\rho$ and the charge transfer per molecule, Q, respectively.

As can be also seen in the PDOS of Tour_{Pyr}, for the pinning situation at $\Theta = 1$ and $\Theta = 0.5$, a new state appears in the intragap region between the HOTC and the LUTC mainly localized on the gold substrates and the N atoms. This was also found by Heimel et al. in [35], where they saw the pinning situation in gold-pyridine systems when increasing the length of the molecule. Collective effects can be again quantitatively investigated corresponding to the concept introduced in section 6.1 for the example of $\text{Tour}_{\text{CH}_2\text{SH}}$. While the PDOS of the whole system shifts about $\delta E_{LUTC} = 0.77$ eV, the contributions of the monolayer $\delta E_{LUMO} = 1.06$ eV and the ones stemming from the bonding $\delta_{BD} = 0.1$ eV add up to 1.16 eV leading to a negative correction energy of $\delta E_{corr}^{LUTC} = -0.19$ eV, to satisfy Eq. 7.2b. Similar results are obtained for the HOTC shift, as can be seen in table 10.

Since the alignment of the closest molecular orbital with E_F determines the charge transport characteristics, pyridine linkers are supposed to be promising docking groups in molecular electronics, giving rise to particularly small charge injection barriers ΔE_{HOTC} and therefore dramatically reduced onset voltages. This is confirmed by the corresponding current-voltage characteristics in Fig. 64d. While there is a typical exponential behaviour for the current per molecule at lower coverages, the current starts out linearly in the Fermi-level pinning regime. Since the onset in the corresponding transmission function (Fig. 63d) is right at E_F, a transport channel is provided instantly when opening the symmetric voltage window. Again the current per molecule has a decreasing trend when going to lower coverages, with the exception of $\theta = 0.5$. This can be explained when looking at the transmission function that establishes a quite distinct LUTC channel and noticeable broadening of the unoccupied states.

Linear (I-V)-characteristics were also found in [113] by Heimel et al., where doping of molecular wires in single-molecule junctions was investigated. In their work, they obtained the Fermi-level pinning regime by using radicalic doped molecules, leading to a current two orders of magnitudes larger than in the undoped molecule. In this thesis Fermi-level pinning can be obtained without using radicals and additionally only for full coverage. Therefore, this is an effect, regulated by pure collective electrostatic effects.
In general Fermi-level pinning was found for pyridine anchor groups in different works in literature [51], [113]. Ma et al. investigated pyridine-based SAMs on gold and found extended charge rearrangements and Fermi level pinning strongly dependent on the length of the molecular backbone. Recently Hong et al. [50] compared different anchor goups in a combined experimental and theoretical study on single molecule conductance of tolanes and found pyridine to exhibit the best performance with high conductance and 100% junction formation probability. Pyridine docking groups were generally found to offer high stability and low conductance fluctuations.

8 Clusters of Molecules

While the full monolayer junction ($\Theta = 1$) and the single molecule junction ($\Theta = 0.0625$) discussed so far represent realistic situations that can also be obtained in experiments, the coverage variation in between ($\Theta = 0.5$, 0.25 and 0.125) constitutes a kind of unnatural situation compared to reality and makes its comparison to experiments difficult. I.e., these situations were studied here primarily to be able to more clearly explain the differences between SAM and single-molecule junctions. When measuring single molecule junctions, it is, however, sometimes the case, that one deals with a group of molecules rather than a single molecule contained between the leads. Therefore, especially for experimentalists, it would be nice to know at which number of molecules collective electrostatic effects like the ones discussed in the previous chapters start playing a rule. Therefore, in the following molecular clusters of different size shall be investigated.

8.1 Structure of the Unit Cells

Since collective effects in clusters shall be investigated on the basis of VASP calculations, proper unit cells need to be defined. As periodic boundary conditions are applied, the molecules have to be assembled in a unit cell that is large enough to avoid interactions with consecutive images. This unit cell is here referred to as supercell, since it is an assembly of the unit cell obtained for full coverage $\Theta = 1$ (2×2 unit cell with 11.81 Å^2), that was introduced in section 3.3.

Two methods seemed are conceivable to finding appropriate input geometries. The first idea was to take a supercell, that is really large, so that adding additional molecules would not change the interaction length between consecutive images. Since this method requires too large computational cost, a second idea was introduced, as illustrated in Fig. 67. Starting with a sufficiently large supercell for one molecule with a constant 'interaction length' **a** between the molecule and its consecutive image, one adds molecule per molecule, while increasing the size of the supercell in every step.

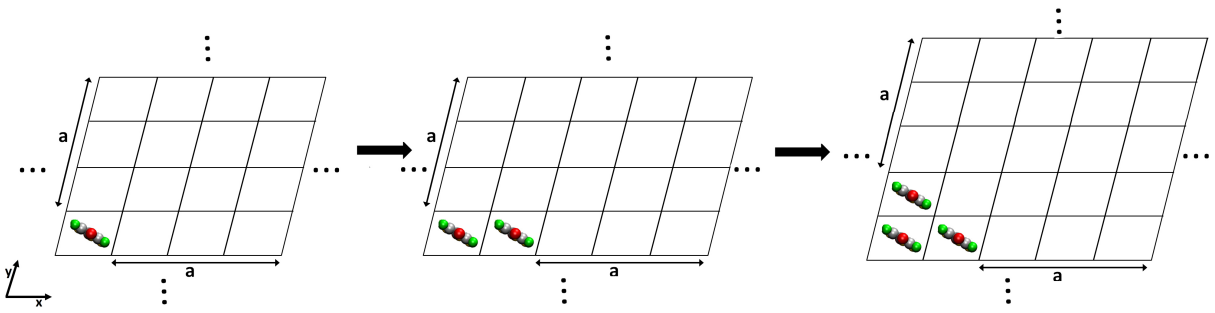

Figure 67: Graphic illustration of the cluster method: when adding molecule per molecule, the unit cell is correspondingly enlarged, so that the 'interaction length' a stays the same

The sufficiently large unit cell for a cluster containing one molecule was decided to be a

super cell, consisting of 4×4 full coverage unit cells, resulting in an interaction length **a** that is three times the full monolayer unit cell, as can be seen from Fig. 68a. (Starting with a larger super cell, consisting of 5×5 full coverage unit cells, resulted in an energy difference of the HOTC of only 0.04 eV in comparison to the 4×4 super cell.) For all cluster calculations only 1 k-point in the 1.Broullin zone was used, to keep computational cost as low as possible. (Tests were also made for 2 k-points resulting in an energy difference in the corresponding density of states of 0.01 eV.)

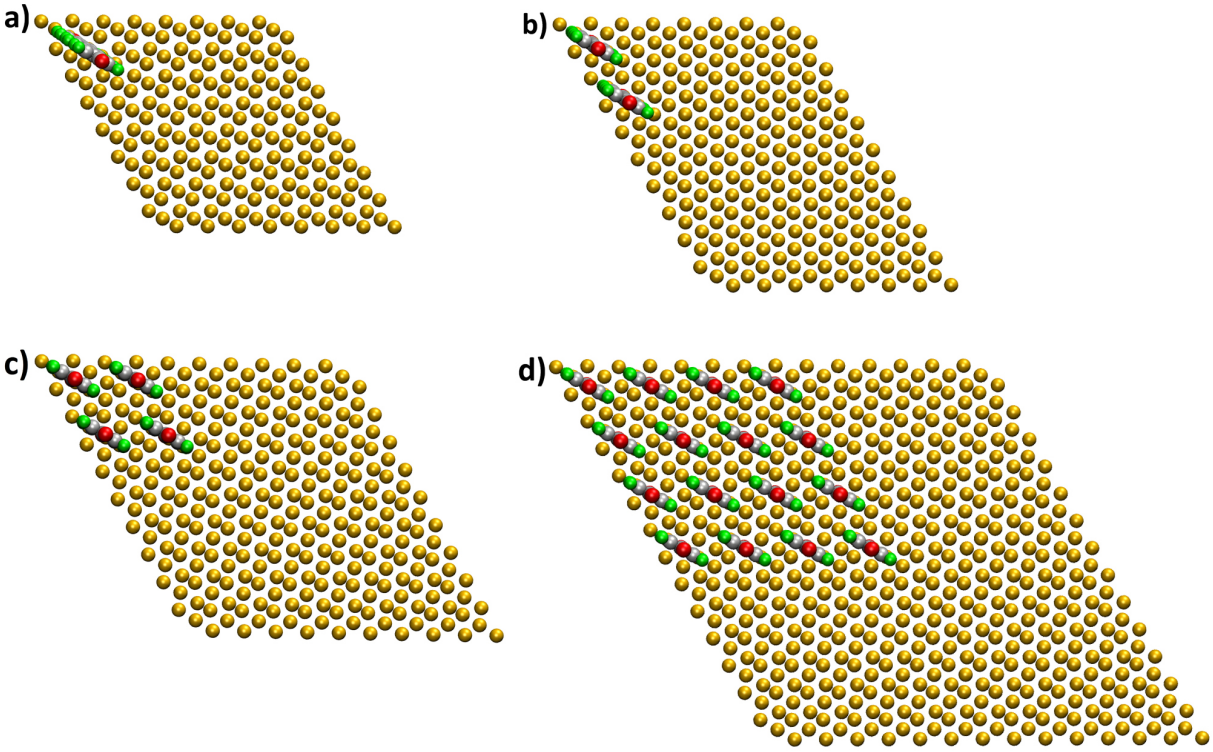

Figure 68: Geometries of the super cells used for the cluster method for 1 molecule (1), 2 molecules (b), 4 molecules (c) and 16 molecules (d)

Cluster geometries were built and calculated using VASP for all systems including 1, 2, 3, 4, 9, 16 and partly 25 molecules. Fig. 68a-d illustrates a top view of some of the structures.

8.2 Results

Fig. 69 shows the density of states projected onto the molecular part per molecule for molecular junctions comprising 1, 2, 3, 4, 9 and 16 N_{out} molecules. The cluster including only one molecule corresponds exactly to the lowest coverage $\Theta = 0.0625$ discussed in section 6. As a quite surprising result, the peaks in the PDOS do not broaden when introducing more and more molecules. This would be expected for an increasing number of molecules due to the stronger coupling to the metal electrodes. The PDOS exhibits again a shift in the HOTC and LUTC energies when increasing the number of molecules. These shifts are now compared to the coverage dependent calculations that were done in

section 6.1.

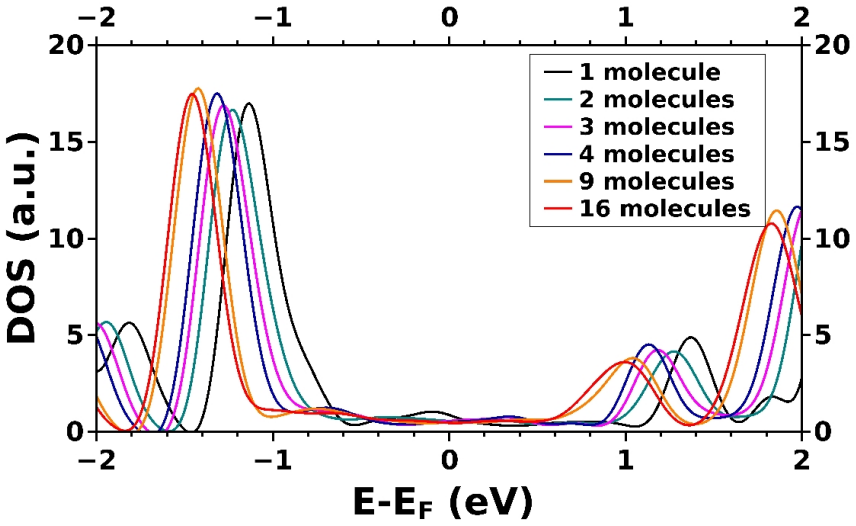

Figure 69: Density of states projected onto the molecular part PDOS for different numbers of molecules in N_{out} clusters

Fig. 70a shows the HOTC energies (obtained from the HOTC peaks of Fig. 69) relative to the Fermi level for different cluster sizes (black circles) compared to the results obtained for different coverages Θ. The latter are included as the vertical, coloured lines. Increasing the number of the molecules in the respective clusters corresponds to increasing the coverage in the junctions. The HOTC peaks are found to rapidly shift with increasing number of molecules. Already two molecules reflect a coverage of $\Theta = 0.125$, whereas 16 molecules almost reach the behaviour of a half coverage monolayer $\Theta = 0.5$. The same calculations were done for all other systems investigated in this thesis (except the N_{in} molecule, since it was found not to exhibit any coverage effect). Fig. 70b-e show the energetic situation for $Tour_{CH_2SH}$, $Tour_{SH}$, $Tour_{NC}$ and $Tour_{Pyr}$. All molecules are found to rapidly approach to the half coverage limit and seem to converge very slowly afterwards to the full monolayer situation. Clusters comprising 25 molecules were calculated for $Tour_{SH}$ and $Tour_{Pyr}$ leading to almost the same result as for 16 molecules. For a further increasing number of molecules, the unit cell become very large, resulting in a very high computational cost, prohibiting calculations for larger clusters.

To completely understand the behaviour illustrated in Fig. 70 further investigations need to be done, including a better understanding of the electrostatic situation, as well as a deeper look at convergence aspects (in particluar k-point convergence).

For future calculations it would be quite interesting to do transport calculations on these molecular clusters and to investigate thermoelectric properties of the junctions. The Seebeck coefficient S is generally known to be independent of the number of molecules [97]. In this work the N_{out} molecule was found to change from mainly HOMO dominated current to LUMO dominated current when varying the coverage and, therefore, to change the sign of S with coverage (see section 6.2.2). Therefore, it would be interesting to do transport

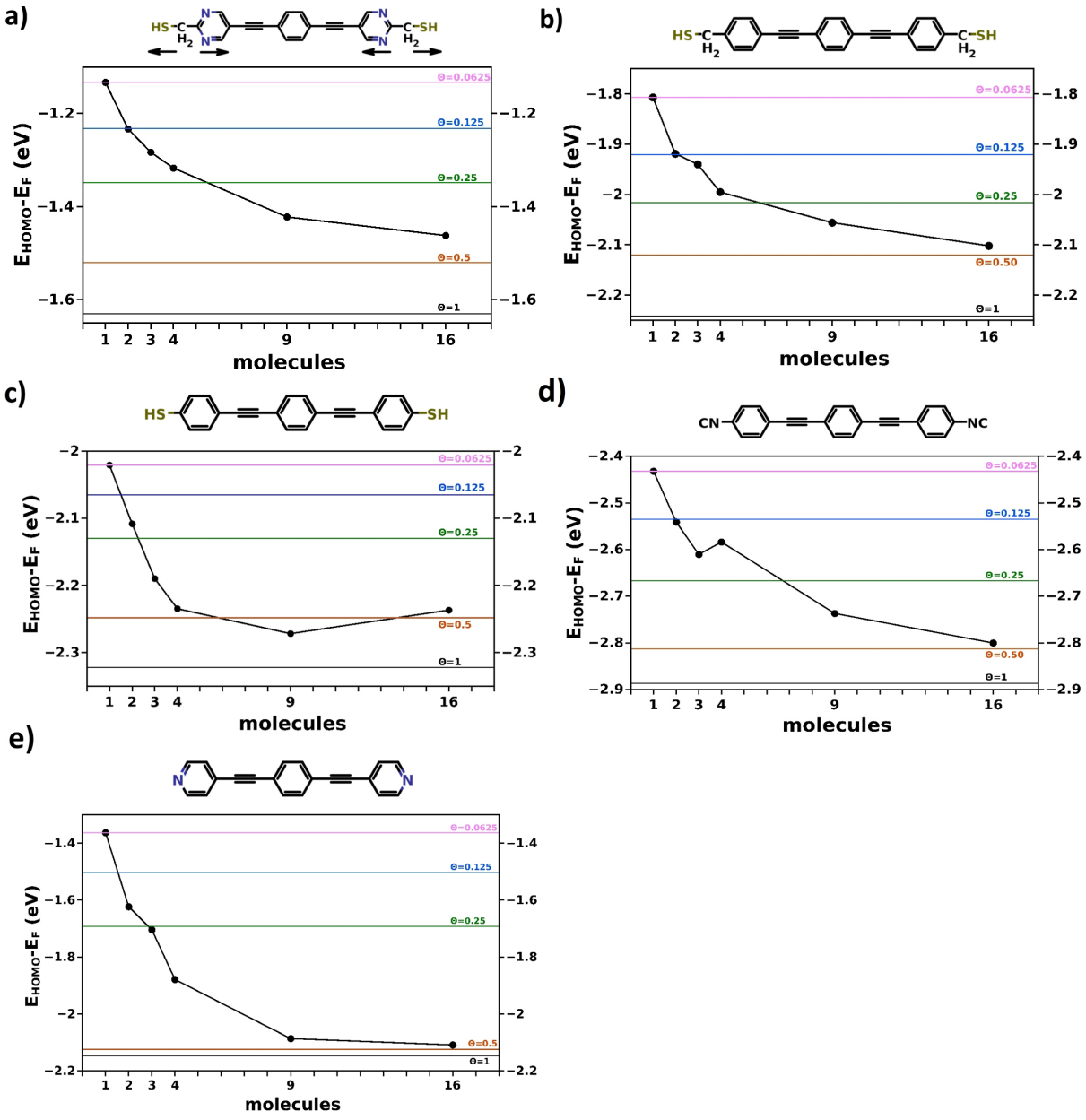

Figure 70: HOMO energies (black circles) for different numbers of molecules in (a) N_{out} (b) $Tour_{CH_2SH}$ (c) $Tour_{SH}$ (d) $Tour_{NC}$ and (e) $Tour_{Pyr}$ clusters compared to the HOMO energies obtained from different coverages Θ (coloured, horizontal lines).

calculations especially on N_{out} clusters, where collective effects are then expected to lead to a Seebeck coefficient that depends on the number of molecules.

References

[1] Hyunwook Song, Mark A. Reed, and Takhee Lee. Single molecule electronic devices. *Advanced Materials*, 23(14):1583–1608, 2011.

[2] Richard L. McCreery and Adam Johan Bergren. Progress with molecular electronic junctions: Meeting experimental challenges in design and fabrication. *Advanced Materials*, 21(43):4303–4322, November 2009.

[3] Richard L. McCreery, Haijun Yan, and Adam Johan Bergren. A critical perspective on molecular electronic junctions: there is plenty of room in the middle. *Physical Chemistry Chemical Physics*, 15(4):1065–1081, December 2012.

[4] Sriharsha V. Aradhya and Latha Venkataraman. Single-molecule junctions beyond electronic transport. *Nature Nanotechnology*, 8(6):399–410, June 2013.

[5] Juan Carlos Cuevas and Elke Scheer. *Molecular electronics an introduction to theory and experiment*. World Scientific, Singapore; Hackensack, NJ, 2010.

[6] Arieh Aviram and Mark A. Ratner. Molecular rectifiers. *Chemical Physics Letters*, 29(2):277–283, 1974.

[7] G. Binning, H. Rohrer, Ch. Gerber, and E. Weibel. Surface studies by scanning tunneling microscopy. In *Scanning Tunneling Microscopy*, volume 6, pages 31–35. Springer Netherlands, Dordrecht, 1982.

[8] G. Binnig and H. Rohrer. In touch with atoms. *Reviews of Modern Physics*, 71(2):S324–S330, March 1999.

[9] John Moreland and J. W. Ekin. Electron tunneling experiments using nb-sn break junctions. *Journal of Applied Physics*, 58(10):3888, 1985.

[10] C. Muller, J. van Ruitenbeek, and L. de Jongh. Conductance and supercurrent discontinuities in atomic-scale metallic constrictions of variable width. *Physical Review Letters*, 69(1):140–143, July 1992.

[11] M. A. Reed. Conductance of a molecular junction. *Science*, 278(5336):252–254, October 1997.

[12] Ismael Dìez-Pèrez, Joshua Hihath, Youngu Lee, Luping Yu, Lyudmyla Adamska, Mortko A. Kozhushner, Ivan I. Oleynik, and Nongjian Tao. Rectification and stability of a single molecular diode with controlled orientation. *Nature Chemistry*, 1(8):635–641, October 2009.

[13] Sense Jan van derMolen and Peter Liljeroth. Charge transport through molecular switches. *Journal of Physics: Condensed Matter*, 22(13):133001, April 2010.

[14] Hyunwook Song, Youngsang Kim, Yun Hee Jang, Heejun Jeong, Mark A. Reed, and Takhee Lee. Observation of molecular orbital gating. *Nature*, 462(7276):1039–1043, December 2009.

[15] Emanuel Lörtscher, Jacob W. Ciszek, James Tour, and Heike Riel. Reversible and controllable switching of a single-molecule junction. *Small*, 2(8-9):973–977, August 2006.

[16] Linda A. Zotti, Thomas Kirchner, Juan-Carlos Cuevas, Fabian Pauly, Thomas Huhn, Elke Scheer, and Artur Erbe. Revealing the role of anchoring groups in the electrical conduction through single-molecule junctions. *Small*, 6(14):1529–1535, June 2010.

[17] Latha Venkataraman, Jennifer E. Klare, Colin Nuckolls, Mark S. Hybertsen, and Michael L. Steigerwald. Dependence of single-molecule junction conductance on molecular conformation. *Nature*, 442(7105):904–907, August 2006.

[18] Ismael Diez-Perez, Joshua Hihath, Thomas Hines, Zhong-Sheng Wang, Gang Zhou, Klaus Müllen, and Nongjian Tao. Controlling single-molecule conductance through lateral coupling of π orbitals. *Nature Nanotechnology*, 6(4):226–231, February 2011.

[19] Ya-Lin Lo, Shih-Jye Sun, and Ying-Jer Kao. Length- and temperature-dependent crossover of charge transport across molecular junctions. *Physical Review B*, 84(7), August 2011.

[20] Michael Galperin and Abraham Nitzan. Cooperative effects in inelastic tunneling. *The Journal of Physical Chemistry B*, 117(16):4449–4453, April 2013.

[21] Yoram Selzer, Lintao Cai, Marco A. Cabassi, Yuxing Yao, James M. Tour, Theresa S. Mayer, and David L. Allara. Effect of local environment on molecular conduction: Isolated molecule versus self-assembled monolayer. *Nano Letters*, 5(1):61–65, January 2005.

[22] D. Cahen, R. Naaman, and Z. Vager. The cooperative molecular field effect. *Advanced Functional Materials*, 15(10):1571–1578, October 2005.

[23] Matthew G. Reuter, Gemma C. Solomon, Thorsten Hansen, Tamar Seideman, and Mark A. Ratner. Understanding and controlling crosstalk between parallel molecular wires. *The Journal of Physical Chemistry Letters*, 2(14):1667–1671, July 2011.

[24] Matthew G. Reuter, Mark C. Hersam, Tamar Seideman, and Mark A. Ratner. Signatures of cooperative effects and transport mechanisms in conductance histograms. *Nano Letters*, 12(5):2243–2248, May 2012.

[25] Arie Landau, Leeor Kronik, and Abraham Nitzan. Cooperative effects in molecular conduction. *The Journal of Computational and Theoretical Nanoscience*, 2008.

[26] Matthew G. Reuter, Tamar Seideman, and Mark A. Ratner. Molecular conduction through adlayers: Cooperative effects can help or hamper electron transport. *Nano Letters*, 11(11):4693–4696, November 2011.

[27] Latha Venkataraman, Jennifer E. Klare, Iris W. Tam, Colin Nuckolls, Mark S. Hybertsen, and Michael L. Steigerwald. Single-molecule circuits with well-defined molecular conductance. *Nano Letters*, 6(3):458–462, 2006.

[28] X. D. Cui. Reproducible measurement of single-molecule conductivity. *Science*, 294(5542):571–574, October 2001.

[29] B. Xu and Nongjian Tao. Measurement of single-molecule resistance by repeated formation of molecular junctions. *Science*, 301(5637):1221–1223, August 2003.

[30] J. G. Kushmerick, J. Naciri, J. C. Yang, and R. Shashidhar. Conductance scaling of molecular wires in parallel. *Nano Letters*, 3(7):897–900, July 2003.

[31] A. Salomon, D. Cahen, S. Lindsay, J. Tomfohr, V.B. Engelkes, and C.D. Frisbie. Comparison of electronic transport measurements on organic molecules. *Advanced Materials*, 15(22):1881–1890, November 2003.

[32] M. Magoga and C. Joachim. Conductance of molecular wires connected or bonded in parallel. *Physical Review B*, 59(24):16011–16021, June 1999.

[33] N. Lang and Ph. Avouris. Electrical conductance of parallel atomic wires. *Physical Review B*, 62(11):7325–7329, September 2000.

[34] A. Natan, L. Kronik, H. Haick, and R. Tung. Electrostatic properties of ideal and non-ideal polar organic monolayers: Implications for electronic devices. *Advanced Materials*, 19(23):4103–4117, December 2007.

[35] Georg Heimel, Lorenz Romaner, Egbert Zojer, and Jean-Luc Brèdas. Toward control of the Metal-Organic interfacial electronic structure in molecular electronics: A first-principles study on self-assembled monolayers of π conjugated molecules on noble metals. *Nano Letters*, 7(4):932–940, April 2007.

[36] Dudi Deutsch, Amir Natan, Yoram Shapira, and Leeor Kronik. Electrostatic properties of adsorbed polar molecules: Opposite behavior of a single molecule and a molecular monolayer. *Journal of the American Chemical Society*, 129(10):2989–2997, March 2007.

[37] L Kronik. Surface photovoltage phenomena: theory, experiment, and applications. *Surface Science Reports*, 37(1-5):1–206, December 1999.

[38] David A. Egger, Ferdinand Rissner, Egbert Zojer, and Georg Heimel. Polarity switching of charge transport and thermoelectricity in self-assembled monolayer devices. *Advanced Materials*, 24(32):4403–4407, August 2012.

[39] L.A. Bumm, J.J. Arnold, M.T. Cygan, T.D. Dunbar, T.P. Burgin, L. Jones, D.L. Allara, J.M. Tour, and P.S. Weiss. Are single molecular wires conducting? *Science*, page 1550, 1996.

[40] Yongqiang Xue, Supriyo Datta, and Mark A. Ratner. Charge transfer and 'band lineup' in molecular electronic devices: A chemical and numerical interpretation. *The Journal of Chemical Physics*, 115(9):4292, 2001.

[41] Fang Chen, Xiulan Li, Joshua Hihath, Zhifeng Huang, and Nongjian Tao. Effect of anchoring groups on single-molecule conductance: Comparative study of thiol-, amine-, and carboxylic-acid-terminated molecules. *Journal of the American Chemical Society*, 128(49):15874–15881, December 2006.

[42] Christian A. Martin, Dapeng Ding, Jakob Kryger Sorensen, Thomas Bjornholm, Jan M. van Ruitenbeek, and Herre S. J. van der Zant. Fullerene-based anchoring groups for molecular electronics. *Journal of the American Chemical Society*, 130(40):13198–13199, October 2008.

[43] Wenbo Chen, Jonathan R. Widawsky, Hèctor Vàzquez, Severin T. Schneebeli, Mark S. Hybertsen, Ronald Breslow, and Latha Venkataraman. Highly conducting π-conjugated molecular junctions covalently bonded to gold electrodes. *Journal of the American Chemical Society*, 133(43):17160–17163, November 2011.

[44] Emanuel Lörtscher, Clara J. Cho, Marcel Mayor, Meinrad Tschudy, Charles Rettner, and Heike Riel. Influence of the anchor group on charge transport through single-molecule junctions. *ChemPhysChem*, 12(9):1677–1682, June 2011.

[45] Carlos R. Arroyo, Edmund Leary, Andrès Castellanos-Gòmez, Gabino Rubio-Bollinger, M. Teresa Gonzàlez, and Nicolàs Agrait. Influence of binding groups on molecular junction formation. *Journal of the American Chemical Society*, 133(36):14313–14319, September 2011.

[46] Yongqiang Xue and Mark Ratner. End group effect on electrical transport through individual molecules: A microscopic study. *Physical Review B*, 69(8), February 2004.

[47] Jian-guo Wang, Emil Prodan, Roberto Car, and Annabella Selloni. Band alignment in molecular devices: Influence of anchoring group and metal work function. *Physical Review B*, 77(24), June 2008.

[48] Guowen Peng, Mikkel Strange, Kristian S. Thygesen, and Manos Mavrikakis. Conductance of conjugated molecular wires: Length dependence, anchoring groups, and band alignment. *The Journal of Physical Chemistry C*, 113(49):20967–20973, December 2009.

[49] Junya Koga, Yuta Tsuji, and Kazunari Yoshizawa. Orbital control of single-molecule conductance perturbed by π-accepting anchor groups: Cyanide and isocyanide. *The Journal of Physical Chemistry C*, 116(38):20607–20616, September 2012.

[50] Wenjing Hong, David Zsolt Manrique, Pavel Moreno-Garcìa, Murat Gulcur, Artem Mishchenko, Colin J. Lambert, Martin R. Bryce, and Thomas Wandlowski. Single molecular conductance of tolanes: Experimental and theoretical study on the junction evolution dependent on the anchoring group. *Journal of the American Chemical Society*, 134(4):2292–2304, February 2012.

[51] ZhongYun Ma, Ferdinand Rissner, LinJun Wang, Georg Heimel, QiKai Li, Zhigang Shuai, and Egbert Zojer. Electronic structure of pyridine-based SAMs on flat

au(111) surfaces: extended charge rearrangements and fermi level pinning. *Physical Chemistry Chemical Physics*, 13(20):9747, 2011.

[52] Marcel Mayor, Heiko B. Weber, Joachim Reichert, Mark Elbing, Carsten von Hänisch, Detlef Beckmann, and Matthias Fischer. Electric current through a molecular Rod-Relevance of the position of the anchor groups. *Angewandte Chemie International Edition*, 42(47):5834–5838, December 2003.

[53] Hongkun Park, Andrew K. L. Lim, A. Paul Alivisatos, Jiwoong Park, and Paul L. McEuen. Fabrication of metallic electrodes with nanometer separation by electromigration. *Applied Physics Letters*, 75(2):301, 1999.

[54] Kazunari Yoshizawa, Tomofumi Tada, and Aleksandar Staykov. Orbital views of the electron transport in molecular devices. *Journal of the American Chemical Society*, 130(29):9406–9413, July 2008.

[55] Franklin Anariba, Hugo Tiznado, James R. Diers, Izabela Schmidt, Ana Z. Muresan, Jonathan S. Lindsey, Francisco Zaera, and David F. Bocian. Comprehensive characterization of hybrid junctions comprised of a porphyrin monolayer sandwiched between a coinage metal overlayer and a si(100) substrate. *The Journal of Physical Chemistry C*, 112(25):9474–9485, June 2008.

[56] Hylke B. Akkerman, Paul W. M. Blom, Dago M. de Leeuw, and Bert de Boer. Towards molecular electronics with large-area molecular junctions. *Nature*, 441(7089):69–72, May 2006.

[57] G. Kresse and J. Hafner. Ab initio molecular dynamics for liquid metals. *Physical Review B*, 47(1):558–561, 1993.

[58] Josè M. Soler, Emilio Artacho, Julian D. Gale, Alberto Garcì, Javier Junquera, Pablo Ordejòn, and Daniel Sànchez-Portal. The SIESTA method for ab initio order-n materials simulation. *Journal of Physics: Condensed Matter*, 14(11):2745, 2002.

[59] P. Hohenberg and W. Kohn. Inhomogeneous electron gas. *Physical Review*, 136(3B):B864–B871, 1964.

[60] W. Kohn and L. J. Sham. Self-consistent equations including exchange and correlation effects. *Physical Review*, 140(4A):A1133–A1138, 1965.

[61] Walter Kohn. Nobel lecture: Electronic structure of matter-wave functions and density functionals. *Reviews of Modern Physics*, 71(5):1253–1266, 1999.

[62] Eberhard Engel and Reiner M Dreizler. *Density functional theory an advanced course*. Springer, Berlin; Heidelberg; New York, 2011.

[63] Robert G. Parr and Weitao Yang. *Density-Functional Theory of Atoms and Molecules*. Oxford University Press, April 1989.

[64] H. Sormann and E. Schachinger. Theoretische festkörperphysik. Wintersemester 2012/13.

[65] L. H. Thomas. The calculation of atomic fields. *Mathematical Proceedings of the Cambridge Philosophical Society*, 23(05):542, October 2008.

[66] John P. Perdew and Yue Wang. Accurate and simple analytic representation of the electron-gas correlation energy. *Physical Review B*, 45(23):13244–13249, June 1992.

[67] John P. Perdew, Kieron Burke, and Matthias Ernzerhof. Generalized gradient approximation made simple. *Physical Review Letters*, 77(18):3865–3868, October 1996.

[68] Hendrik J. Monkhorst and James D. Pack. Special points for brillouin-zone integrations. *Physical Review B*, 13(12):5188–5192, June 1976.

[69] Emilio Artacho, Daniel Sànchez-Portal, Pablo Ordejòn, Alberto Garcia, and Josè M. Soler. Linear-scaling ab-initio calculations for large and complex systems. *Condensed Matter*, 1999.

[70] J. C. Slater and G. F. Koster. Simplified LCAO method for the periodic potential problem. *Physical Review*, 94(6):1498–1524, June 1954.

[71] Emilio Artacho, Josè Marìa Cela, Julian D. Gale, Alberto Garcìa, Javier Junquera, Pablo Ordejòn, Daniel Sànchez-Portal, and Josè M. Soler. Siesta user's guide. 2010.

[72] Georg Kresse, Martijn Marsman, and Furthmüller Jürgen. Vasp user's guide. 2012.

[73] D. J. Chadi and Marvin L. Cohen. Special points in the brillouin zone. *Physical Review B*, 8(12):5747–5753, December 1973.

[74] Juana Moreno and Josè Soler. Optimal meshes for integrals in real- and reciprocal-space unit cells. *Physical Review B*, 45(24):13891–13898, June 1992.

[75] R. Landauer. Spatial variation of currents and fields due to localized scatterers in metallic conduction. *IBM Journal of Research and Development*, 1(3):223–231, July 1957.

[76] Mads Brandbyge, Josè-Luis Mozos, Pablo Ordejòn, Jeremy Taylor, and Kurt Stokbro. Density-functional method for nonequilibrium electron transport. *Physical Review B*, 65(16), March 2002.

[77] Supriyo Datta. Electrical resistance: an atomistic view. *Nanotechnology*, 15(7):S433–S451, July 2004.

[78] Supriyo Datta. *Quantum Transport: Atom to Transistor*. Cambridge University Press, June 2005.

[79] M. Paulsson. Non equilibrium green's functions for dummies: Introduction to the one particle NEGF equations. *arXiv:cond-mat/0210519*, October 2002.

[80] M. P. Lopez Sancho, J. M. Lopez Sancho, J. M. L. Sancho, and J. Rubio. Highly convergent schemes for the calculation of bulk and surface green functions. *Journal of Physics F: Metal Physics*, 15(4):851, April 1985.

[81] Georg Heimel, Ferdinand Rissner, and Egbert Zojer. Modeling the electronic properties of π-conjugated self-assembled monolayers. *Advanced Materials*, 22(23):2494–2513, April 2010.

[82] R. Feynman. Forces in molecules. *Physical Review*, 56(4):340–343, August 1939.

[83] Ödö Farkas and H. Bernhard Schlegel. Methods for optimizing large molecules. an improved algorithm for geometry optimization using direct inversion in the iterative subspace (gdiis). *Physical Chemistry Chemical Physics*, 4(1):11–15, January 2002.

[84] Tomàš Bučko, Jürgen Hafner, and Jànos G. Àngyàn. Geometry optimization of periodic systems using internal coordinates. *The Journal of Chemical Physics*, 122(12):124508, 2005.

[85] Michael Teter, Michael Payne, and Douglas Allan. Solution of schrödingers equation for large systems. *Physical Review B*, 40(18):12255–12263, December 1989.

[86] Jon Baker, Alain Kessi, and Bernard Delley. The generation and use of delocalized internal coordinates in geometry optimization. *The Journal of Chemical Physics*, 105(1):192, 1996.

[87] Elena F. Koslover and David J. Wales. Geometry optimization for peptides and proteins: Comparison of cartesian and internal coordinates. *The Journal of Chemical Physics*, 127(23):234105, 2007.

[88] Taekyeong Kim, Hèctor Vàzquez, Mark S. Hybertsen, and Latha Venkataraman. Conductance of molecular junctions formed with silver electrodes. *Nano Letters*, 13(7):3358–3364, July 2013.

[89] M. J. Frisch, G. W. Trucks, H. B. Schlegel, G. E. Scuseria, M. A. Robb, J. R. Cheeseman, G. Scalmani, V. Barone, B. Mennucci, G. A. Petersson, H. Nakatsuji, M. Caricato, X. Li, H. P. Hratchian, A. F. Izmaylov, J. Bloino, G. Zheng, J. L. Sonnenberg, M. Hada, M. Ehara, K. Toyota, R. Fukuda, J. Hasegawa, M. Ishida, T. Nakajima, Y. Honda, O. Kitao, H. Nakai, T. Vreven, J. A.Jr. Montgomery, J. E. Peralta, F. Ogliaro, M. Bearpark, J. J. Heyd, E. Brothers, K. N. Kudin, V. N. Staroverov, R. Kobayashi, J. Normand, K. Raghavachari, A. Rendell, J. C. Burant, S. S. Iyengar, J. Tomasi, M. Cossi, N. Rega, J. M. Millam, M. Klene, J. E. Knox, J. B. Cross, V. Bakken, C. Adamo, J. Jaramillo, R. Gomperts, R. E. Stratmann, O. Yazyev, A. J. Austin, R. Cammi, C. Pomelli, J. W. Ochterski, R. L. Martin, K. Morokuma, V. G. Zakrzewski, G. A. Voth, P. Salvador, J. J. Dannenberg, S. Dapprich, A. D. Daniels, Ö. Farkas, J. B. Foresman, J. V. Ortiz, J. Cioslowski, and D. J. Fox. Gaussian 09 revision d.01. 2009.

[90] G. A. Petersson, Andrew Bennett, Thomas G. Tensfeldt, Mohammad A. Al-Laham, William A. Shirley, and John Mantzaris. A complete basis set model chemistry. i. the total energies of closed-shell atoms and hydrides of the first-row elements. *The Journal of Chemical Physics*, 89(4):2193, 1988.

[91] Lorenz Romaner, Georg Heimel, and Egbert Zojer. Electronic structure of thiol-bonded self-assembled monolayers: Impact of coverage. *Physical Review B*, 77(4), January 2008.

[92] Lorenz Romaner, Georg Heimel, Mathis Gruber, Jean-Luc Brèdas, and Egbert Zojer. Stretching and breaking of a molecular junction. *Small*, 2(12):1468–1475, December 2006.

[93] Magnus Paulsson and Supriyo Datta. Thermoelectric effect in molecular electronics. *Physical Review B*, 67(24), June 2003.

[94] Christophe Krzeminski, Christophe Delerue, Guy Allan, Dominique Vuillaume, and R. M. Metzger. Theory of electrical rectification in a molecular monolayer. *Physical Review B*, 64(8):085405, 2001.

[95] P. Reddy, S.-Y. Jang, R. A. Segalman, and A. Majumdar. Thermoelectricity in molecular junctions. *Science*, 315(5818):1568–1571, March 2007.

[96] Janakiraman Balachandran, Pramod Reddy, Barry D. Dunietz, and Vikram Gavini. End-group-induced charge transfer in molecular junctions: Effect on electronic-structure and thermopower. *The Journal of Physical Chemistry Letters*, 3(15):1962–1967, August 2012.

[97] Kanhayalal Baheti, Jonathan A. Malen, Peter Doak, Pramod Reddy, Sung-Yeon Jang, T. Don Tilley, Arun Majumdar, and Rachel A. Segalman. Probing the chemistry of molecular heterojunctions using thermoelectricity. *Nano Letters*, 8(2):715–719, February 2008.

[98] Aaron Tan, Janakiraman Balachandran, Seid Sadat, Vikram Gavini, Barry D. Dunietz, Sung-Yeon Jang, and Pramod Reddy. Effect of length and contact chemistry on the electronic structure and thermoelectric properties of molecular junctions. *Journal of the American Chemical Society*, 133(23):8838–8841, June 2011.

[99] Jonathan R. Widawsky, Pierre Darancet, Jeffrey B. Neaton, and Latha Venkataraman. Simultaneous determination of conductance and thermopower of single molecule junctions. *Nano Letters*, 12(1):354–358, January 2012.

[100] J. Janak. Proof that $\partial E/\partial n_i = \epsilon$ in density-functional theory. *Physical Review B*, 18(12):7165–7168, December 1978.

[101] Georg Heimel, Lorenz Romaner, Jean-Luc Brèdas, and Egbert Zojer. Interface energetics and level alignment at covalent metal-molecule junctions: π-conjugated thiols on gold. *Physical Review Letters*, 96(19):196806, May 2006.

[102] Gregor Witte, Simon Lukas, Paul S. Bagus, and Christof Wöll. Vacuum level alignment at organic/metal junctions: Cushion effect and the interface dipole. *Applied Physics Letters*, 87(26):263502, 2005.

[103] Emilio Artacho, Josè Marìa Cela, Julian D. Gale, Alberto Garcìa, Javier Junquera, Pablo Ordejòn, Daniel Sànchez-Portal, and Josè M. Soler. Siesta user's guide. 2010.

[104] Jeremy Taylor, Mads Brandbyge, and Kurt Stokbro. Theory of rectification in tour wires: The role of electrode coupling. *Physical Review Letters*, 89(13), September 2002.

[105] Yongqiang Xue and Mark Ratner. Microscopic study of electrical transport through individual molecules with metallic contacts. i. band lineup, voltage drop, and high-field transport. *Physical Review B*, 68(11), September 2003.

[106] Jeremy Taylor, Mads Brandbyge, and Kurt Stokbro. Conductance switching in a molecular device: The role of side groups and intermolecular interactions. *Physical Review B*, 68(12), September 2003.

[107] Gerold M. Rangger, Lorenz Romaner, Georg Heimel, and Egbert Zojer. Understanding the properties of interfaces between organic self-assembled monolayers and noble metals-a theoretical perspective. *Surface and Interface Analysis*, 40(3-4):371–378, March 2008.

[108] M. Strange, I. S. Kristensen, K. S. Thygesen, and K. W. Jacobsen. Benchmark density functional theory calculations for nanoscale conductance. *The Journal of Chemical Physics*, 128(11):114714, 2008.

[109] Su Ying Quek, Latha Venkataraman, Hyoung Joon Choi, Steven G. Louie, Mark S. Hybertsen, and J. B. Neaton. Amine-Gold linked single-molecule circuits: Experiment and theory. *Nano Letters*, 7(11):3477–3482, November 2007.

[110] J. Neaton, Mark Hybertsen, and Steven Louie. Renormalization of molecular electronic levels at metal-molecule interfaces. *Physical Review Letters*, 97(21), November 2006.

[111] Su Ying Quek, Hyoung Joon Choi, Steven G. Louie, and J. B. Neaton. Length dependence of conductance in aromatic single-molecule junctions. *Nano Letters*, 9(11):3949–3953, November 2009.

[112] Pierre Darancet, Jonathan R. Widawsky, Hyoung Joon Choi, Latha Venkataraman, and Jeffrey B. Neaton. Quantitative Current-Voltage characteristics in molecular junctions from first principles. *Nano Letters*, 12(12):6250–6254, December 2012.

[113] Georg Heimel, Egbert Zojer, Lorenz Romaner, Jean-Luc Brèdas, and Francesco Stellacci. Doping molecular wires. *Nano Letters*, 9(7):2559–2564, July 2009.

[114] Norbert Koch. Organic electronic devices and their functional interfaces. *ChemPhysChem*, 8(10):1438–1455, July 2007.

[115] Slawomir Braun, William R. Salaneck, and Mats Fahlman. Energy-level alignment at Organic/Metal and Organic/Organic interfaces. *Advanced Materials*, 21(14-15):1450–1472, April 2009.